Synthesis of Semiconductor Quantum Dots, Study of Their Optical Properties and Their Application in Sensitized Solar Cells

A Thesis

Submitted in partial fulfillment of the requirements

of the degree of

Doctor of Philosophy

by

Padmashri Patil

20083020

INDIAN INSTITUTE OF SCIENCE EDUCATION AND RESEARCH, PUNE

JULY, 2014

To my parents

CERTIFICATE

Certified that the work incorporated in this thesis entitled "**Synthesis of Semiconductor Quantum Dots, Study of Their Optical Properties and Their Applications in Sensitized Solar Cells"** submitted by **Padmashri Patil** was carried out by the candidate, under my supervision. The work presented here or any part of it has not been included in any other thesis submitted previously for the award of any degree or diploma from any other University or institution.

Dr. Shouvik Datta,

Supervisor

DECLARATION

I declare that, this written submission represents my ideas in my own words and where other's ideas have been included, I have adequately cited and referenced the original sources. I also declare that I have adhered to all principles of academic honesty and integrity and have not misrepresented or fabricated or falsified any idea / data / fact / source in my submission. I understand that violation of the above will be cause for disciplinary action by the Institute and can also evoke penal action from the sources which have thus not been properly cited or from whom proper permission has not been taken when needed.

Padmashri Patil,
20083020

ACKNOWLEDGMENTS

I take this opportunity to express my gratitude to all the individuals without whom the dream of completing my Ph. D. thesis would be incomplete.

Firstly, I would like to express my gratitude to my Ph. D. supervisor Dr. Shouvik Datta. It was a great opportunity for me to work in his lab. I was always on a steep learning curve, as I was trying to keep up with Dr. Shouvik's pace. His knowledge (a product of reading a great many choice books for specific topics in each, I'm sure) and his "out- of- the- box" thinking kept us all on our feet for as long as my six year tenure. I consider myself privileged that I was able train with him to think in a non-conventional way, and to adapt this way of working on many a research ideas. He is very hard to surprise with new ideas as more often than not, my new and exciting ideas were already a by-product of his thought processes! This in particular drove us to strive and come up with newer and better approaches.

Besides my supervisor, it is my pleasure to thank our collaborators Dr. Shivprasad Patil and Dr. Angshuman Nag who helped me in understanding many new scientific concepts and instrumentation and data analysis. Working with them was really a great experience for me. I really appreciate their patience and helping attitude. Two of my publications would have been impossible without their collaboration. I am also thankful to their students Murhty, Kiran and Jagdishwara Rao for their help during these collaborations.

I really appreciate the help we got from Dr. S. B. Ogale from NCL Pune. My sincere thanks to Dr. Ogale and Ms.Prachi, who is a member of Dr. Ogale's group, for teaching me the techniques of the TiO_2 paste preparation for Dye Sensitized Solar Cell fabrication.

I thank the Indian Nanoelectronics User Program (INUP) program at IIT Bombay for helping us in the deposition of Platinum electrodes which we used as electrodes in sensitized solar cell fabrication.

I thank my RAC members Dr. Prasenjit Ghosh, Dr. Pankaj Mandol, Dr. Shivprasad Patil and Dr. Angshuman Nag for their timely assistance, which aided me in shaping my thesis and completing the work on time. I also extend my thanks to all the physics faculty of IISER, Pune for teaching me concepts related to and beyond Physics. I will be always thankful to Dr. Ambika,

Dr. Pavan Kumar, Dr. Harsh Chaturvedi, Dr. Surjeet Singh, Dr. Sulbha Kulkarni, Mr. Prashant Kale and Mr. Neelesh Dhumbare for their help. I am highly grateful to IISER for graduate fellowship without which this work would have been hardly possible.

Some of the most enjoyable moments of my time in IISER have been when I was working in the lab. I must say the time I spent in lab was made a lot more enjoyable and cheerful by my colleague friends Arthur, Kanika and the frequent, welcome visitor Murhty. They have taught me so many things which helped me not just in lab but otherwise, too. I specially thank them for helping me in characterizations as well as giving me company in all the joyous and stressful situations alike. I would also like to thank a few project students who worked with me a while ago Dhavala, Zuala and Krithika who also became my good friend. I would also like to thank all the present and past project students who joined our lab and helped me in conducting experiments.

This journey would have been very boring without the company of many cheerful friends like Ramya, Smitha, Murhty, Mayur, Arun, Abhishek, Arthur, Kanika, Snehal, Vimal, Resmi, Mandar, Sunil, Neeraj, Keerthi, Usha, Madhan, and all the juniors who joined after us. I would like to thank Ramya and Smita for accepting me as their virtual roommate and teaching me how to get ready to catch an 8am bus even if I woke up just at 7.45am! Thanks for bearing my quirks; I will miss you always. I am glad to have had the tasteful company of Ramya, Resmi and Murhty for cooking at HR2. I will never forget the conversations we had after dinner which used to go on for hours and hours on the same topics for months!

I must like to mention special thanks to my friend Chaitra. I must say the refreshment that I got because of music sessions we had helped me to relax my mind timely. I really enjoyed learning of Carnatic Vocal and few things about the Veena. I also thank Krithika for joining our practice sections and cheering us with sweet melodious songs.

I can’t thank my mother and father enough for their innumerable and immense sacrifices and hard work. Their support has been invaluable to me throughout. I consider myself very lucky to have such parents. I also thank my Aaka, Daji, brother Ram, niece and nephew Kishor and Kishori without whose support I would not have stepped out of my village for education. I also appreciate the love shown by my parents- in-law Aatya, Tatya during these years. I thank my brothers- in-law Nana and Bhai for their support and understanding in all situations. Last but not

least, I thank my dearest husband Sachin without whose support, understanding and encouragement, this work would have stopped without reaching completion.

Padmashri Patil.

Abstract

Requirement of clean and cheap renewable energy production by understanding and then manipulating the physics of semiconductor nanostructures to realize cost effective and efficient Nanophotovoltaic devices is the primary drive for the current research. Many advantages of semiconductor quantum dots (QDs) like higher optical absorption cross-section, wavelength tunability, reduced phonon mediated relaxation and capability for solution processing at a low cost made these very popular. Here we have reported easy, economic synthesis and fabrication procedures for QD based nano-photovoltaic devices.

The main focus of this thesis work is to develop synthesis procedures with reduced synthesis steps while maintaining optimum optical and electronic transport qualities of these nanostructured devices. We have developed a simple low temperature and aqueous synthesis method for CdTe QDs. The measured photoluminescence quantum yield of the as prepared QDs is highest among the aqueous based synthesis procedures reported till now for CdTe QDs. We have used these QDs as photo-absorber in Quantum Dot Sensitized Solar Cells. However it was evident that the polysulfide electrolyte reacts with these CdTe QDs, which reduces the performance of QD sensitized cells. Further we have tried to avoid such reactive degradation using type-II heterostructure i.e. core/shell structure with CdTe as core and CdSe as shell.

We then presented a quicker, economic and less toxic, single step aqueous synthesis procedure for core/shell QDs at relatively low temperature. We have shown that the structural as well as optical properties of these core/shell QDs are almost similar to that of core/shell QDs synthesized with purification of core QDs. We have demonstrated that the power conversion efficiency of QD sensitized cells depend on their shell thickness. Reasonable good efficiency (~2%) is measured for the devices fabricated using core/shell QDs having thicker shells. There might be two reasons for observing efficiency increment by using such CS QDs # 1. energy level alignment in type-II heterostructure helps in separation of photogenerated carriers and #2. shell layer helps in separating the electrolyte and core which avoids reaction between them.

Interestingly, the efficiency of the cells also increases by ~83% with sintering of photo-anode, as this sintering helps in removing the insulating capping layer and thereby improves electronic charge transport.

Many a time agglomeration of QDs due to sintering of photo-anode also reduces its photo absorption efficiency. To avoid such issues while making the QD sensitized cells, we have used uncapped i.e. ligand free $AgInS_2$ QDs as photo-absorber provided by the research group of Dr. Angshuman Nag, IISER Pune. The obtained efficiency using ligand free QDs is superior than any of the previous reports on capped $AgInS_2$ QDs based QDSSCs as it facilitates better charge transport.

Apart from these studies we have also studied the dependence of hydrodynamic size on the excitation intensity using Florescence Correlation Spectroscopy in collaboration with Dr. Shivprasad Patil, IISER Pune. In this study we have observed that the estimated hydrodynamic size is significantly affected by photo-excitation intensity above a certain threshold due to blinking. Here we have calculated photo-darkened fraction and probability of QD entering into dark state upon photon absorption.

We have also studied collisional broadening of E_3 excitonic resonance in absorption spectra over wide range sizes and its overall aging and temperature variation for lead sulfide QDs at room temperature. As the carrier multiplication (CM) is a direct consequence of hot-exciton physics therefore, our results on the effects of excitonic collisions on absorbance spectra may help in understanding the physics of CM for photovoltaic applications.

CONTENTS

LIST OF FIGURES

LIST OF TABLES

Chapter 1

Introduction

I. Preface

Nanotechnology has many a promises; a promise for possible technological breakthroughs, a promise to make life better. In a way, it is a promise to make devices efficient, faster, smaller and cheaper. Most importantly, nanoscience and nanotechnology have the potential to play a huge role in coming up with solutions for today's demand for energy. Many researchers have worked on different aspects of nanoscience and nanotechnology to fulfill these promises, by coming up with innovative ideas like that of robots swimming in blood veins, palm sized satellites, writing with atoms to power generating windows, smaller and smaller computers, cars generating power using roof painted photovoltaic cells among many others. Yes it is possible! This was a dream of the famous scientist Prof. Feynman who knew that "There is plenty of room at the bottom". This famous talk delivered in 1959 is considered as a seminal event in the history of science which is happened to be a conceptual beginning of the field 'nanotechnology'.

II. Quantum Confinement

As discussed above, one of the ways to come up with new materials and new technologies is to look at the properties of materials at very small length scales of nanometers.

There the spatial confinement is the key for attaining desirable nano-technological effect and it is the only way. In case of materials, the question about the exact amount of confinement where quantum effects begin to influence the physical properties is generally answered by a characteristic length, which is called as the exciton Bohr radius (a_b). Exciton is an electron-hole bound pair and it is generated once a material is either optically or electrically excited. Many a times mutual coulombic attraction between an electron and a hole forms such a hydrogen atom like bound excitonic state inside a solid[1,2]. The representation of an exciton is as shown in figure 1.1.

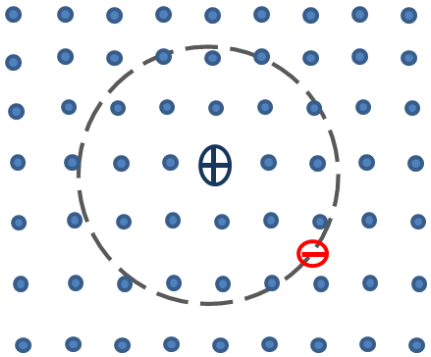

Figure 1.1. Exciton: Bound pair of electron and hole forming hydrogen atom like situation due to mutual Coulombic interaction between them. An electron is shown by red color circle with negative sign and the hole is shown by blue color circle with positive sign.

At the lowest energy state the minimum distance between an electron and a hole is called the exciton Bohr radius (a_b). In general it is given by,

$$a_b = \frac{\varepsilon_o h^2}{\pi m_\mu e^2} \qquad (1.1)$$

where ε_o is the static dielectric constant of the material, e is electronic charge, h is the Plank's constant and $m_\mu = \left(\frac{m_e^* m_h^*}{m_e^* + m_h^*} \right)$ is reduced mass of electron-hole bound state, m_e^* and m_h^* are effective mass of electron and holes respectively in M.K.S units. For semiconductors this value falls in the range of a few nanometers (nm). Materials with this size are introduced as nanomaterials/ nanoparticles. In this way nanoparticles or nanocrystals of a material can be

formed by spatial confinement below its exciton Bohr radius. At such small sizes, the material loses its bulk properties and exhibit exciting optical, electrical, chemical properties mainly governed by quantum phenomenon. Most importantly, as a result of spatial confinement, the allowed energy levels in materials become discrete and separation between them increases. One can get an idea of the discrete energy level structure present within a quantum structure from the textbook description of an infinite barrier quantum well potential for which the energy eigenvalues are given by[3,4]_

$$E_n = n^2 \times \frac{h^2}{8m^* L^2} \ , \qquad (1.2)$$

Here, n = 1, 2, 3,....etc, m* is the effective mass of the electron/hole in a particular band, L is the confinement width and h is the Plank's constant, The minimum available energy difference between the filled valance band and the empty conduction band also increases, which can be understood by the uncertainty principle. As a result, the lowest transition energy blue shifts with respect to the bulk band gap. The total increase in energy is the result of confinement energy due to columbic interaction and exciton binding energy and it is given by equation 1.3.

$$E = E_g + \frac{1}{L^2}\left(\frac{h^2}{8m_\mu}\right) - \frac{1}{L}\left(\frac{1.786e^2}{\varepsilon_0}\right) - 0.248E^*_{RY} \qquad (1.3)$$

Here E is the lowest transition energy of confined material, E_g is the bulk band gap of the material, $m_\mu = \left(\frac{m_e^* m_h^*}{m_e^* + m_h^*}\right)$ is reduced mass of electron-hole bound state, m_e* and m_h* are effective mass of electron and holes respectively in M.K.S. units, L is the size of the material, ε_o is the static dielectric constant, E_{RY}* is the effective Rydberg energy $E^*_{RY} = \frac{2\mu\pi^2 e^4}{h^2 \varepsilon_0^{\ 2}}$ and e is electric charge. The value of last term is very small and generally neglected.

Based on the dimension of confinement there are three types of quantum structures[4].

a) The quantum well (QW) in which electrons and holes are free to move in a plane and localized in the perpendicular direction.

b) The quantum wire (QWR) in which electrons and holes are free to move along one direction but confined along other two, and

c) The zero dimensional quantum dot (QD) in which electrons and holes are localized in all three directions. Most of the nanoparticles actually belong to this category.

These structures have different electronic density of states depending on the dimensionality as shown in figure 1.2.

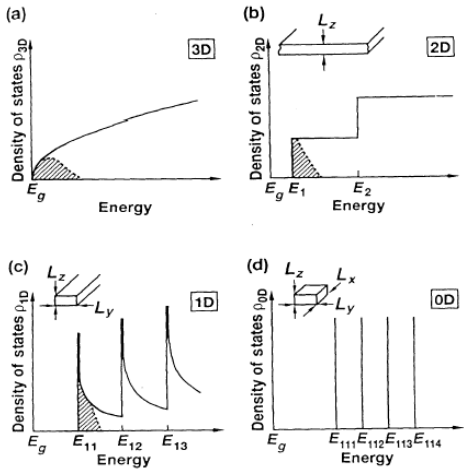

Figure 1.2. Joint density of states for a) bulk, b) Quantum Well c) Quantum Wire d) Quantum Dot. Filled states are represented by shaded region. From Eli Kapon, in Semiconductor Lasers Academic Press, San Diego, 1999.

III. Quantum Dots as a Better Alternative

Semiconductor quantum dots were first prepared in colloidal solution by L.E. Brus[5] and by Alexei Ekimov[6] in glass matrix. The term QD was first coined by Mark Reed[7] in 1988. QDs are considered as better alternatives for use in applications compared to its bulk constitutes as well as other available organic molecules. These are the few reasons which make QDs a better choice over the others.

1) Band gap engineering is possible through size variation. This feature helps us to tune the band gap and get desirable absorption/emission[8].

2) Spatial quantization allows energy levels to split and distance between energy levels increases as $\Delta E \propto 1/r^2$. This slows down phonon mediated relaxation channel for the charge

carriers[9]. Because of this QDs are thought of as strong candidates for multiple exciton generation (MEG)[10,11].

3) Increased absorption cross-section compared to the bulk material[12].

With all these advantages of size tunability, novel physical properties as compared to a single bulk material, many researchers used QDs in applications like transistors[13,14], light emitting diodes[15,16,17], solar cells[18,19] etc.. Among all the known methods to grow a QD, chemical synthesis of QDs is known to be easier, quicker, more economic and highly reproducible. Studies have shown that colloidal QDs synthesized using chemical synthesis are good for solution processing and help in better material utilization. As cost is one of the primary concerns in any application (e.g. solar cell), it has been shown that use of colloidal solution of QDs is very economic due to material utilization rate. Therefore, any research in this area of growth and synthesis of good quality QDs is important in order to provide a better and economic way of producing good quality materials.

IV. Chemical Synthesis of Quantum Dots

Colloidal quantum dots can be fabricated by wet chemical synthesis process using chemical precursors dissolved in solutions. Size tuning is easy in this method and can be easily accomplished by either varying the temperature or the duration of the reaction or by varying concentration of the capping molecules. In chemical reaction when the concentration of a solute in the solution exceeds its solubility, a new phase appears. This supersaturated solution with excess solute possesses high Gibb's free energy and the overall energy would be decreased by segregating solutes. Thus the reduction in Gibb's free energy is the driving force for nucleation and growth. The change in Gibb's free energy per unit volume in solid phase is dependent on the concentration of the solute_

$$\Delta G_v = -kT/\Omega \ln (1+ (C-C_o)/C_o), \quad (1.4)$$

Here, C is the concentration of the solute, C_O is the equilibrium concentration or solubility, Ω is the atomic volume. Without super-saturation when $C-C_o/C_o = 0$, ΔG_V is zero, and no nucleation would occur. When $C > C_O$, ΔG_v is negative and nucleation occurs spontaneously.

If a spherical nucleus of radius 'r' is formed then the change in Gibb's free energy or volume energy is given by $\Delta\mu_v$,

$$\Delta\mu_v = 4/3\pi\, r^3 \Delta G_v \qquad (1.5)$$

However, formation of a new phase is due to the reduction of free energy so the change in surface energy $\Delta\mu_s$,

$$\Delta\mu_s = 4\pi r^2 \gamma \qquad (1.6)$$

Here, γ is surface free energy. Total change in chemical potential for formation of the nucleus is thus the resultant reduction in energy due to volume energy and surface energy.

$$\Delta G = \Delta\mu_v + \Delta\mu_s = (4/3)\pi\, r^3 \Delta G_v + 4\pi r^2 \gamma \qquad (1.7)$$

At $d\Delta G/dr = 0$ we will get a critical size r* of nucleus required for continuous growth into a QD.

$$r^* = -2\gamma/\Delta G_V \qquad (1.8)$$

A nucleus smaller than r* will dissolve back into the solution to reduce free energy. Many times further growth of QDs proceeds through Oswald's ripening. In this growth process smaller QDs dissolve due to higher surface energy and solute will be used for further growth of comparatively bigger QDs. In this way it is possible to achieve large mean diameter in particle size distribution.

Another way to control size of QD is concentration variation of capping layer molecule in chemical reaction[20]. Capping layer molecules are organic short/long chain molecules also called as ligands/ surfactants. These are bi-functional molecules with polar groups at both ends. The molecular structures for few thiol based capping molecules are shown in figure 1.3.

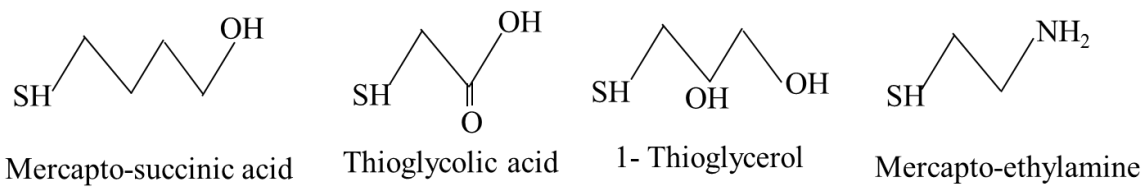

Figure 1.3. Molecular structure for different thiol based capping molecules.

In general these molecules possess a hydrophobic tail and a hydrophilic head. Choice of molecule is always such that one end binds the ion from QD and the other end is free to move in the solvent as shown in figure 1.4. The main idea of having a capping layer is to make QDs stable i.e. non-oxidizing, non-agglomerating, passivized surface without dangling bonds and presence of these also makes QDs soluble in the solvent[21]. For an aqueous QD synthesis thiol based ligand is a good choice as a lot of options such as thioglycolic acid, 1-thioglycerol, mercaptoethylamine, mercapto-succinic acid etc. are available.

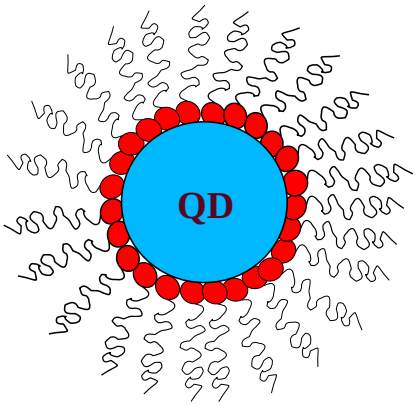

Figure 1.4. Schematic showing QD capped with organic molecules.

V. Energy Crisis in India and Potential for Nanotechnology

India has an installed power capacity of ~234 GW[22]. This makes India the fourth largest electricity producing country in the world[23]. Along with huge production, energy demand is also large. In 2009 the per capita average annual domestic electricity consumption in rural area was 96 kWh and 288 kWh in urban areas in contrast to worldwide per capita annual average of 2600 kWh and 6200 kWh in European Union[24]. Approximately more than few hundred million Indians live without electricity, and 800 million Indian still use traditional bio-mass as the fuel for their cooking. These traditional fuels are inefficient as well as environmentally polluting sources of energy, releasing high levels of smoke[25] on their combustion, which causes chronic health problems. This also leads to deforestation, imbalances in the ecosystem and affects global climate. Burning of biomass and firewood will not stop until unless electricity or clean burning

fuel and consumption technologies becomes reliably available and adopted in rural and urban India[26]. Secondly India still depends heavily on import of oil and natural gas. Use of these sources creates an economic burden on the government and at the same time causes pollution. Apart from all these problems a major challenge for India is its dependence on a non-renewable energy source like coal as shown in figure 1.5. Nearly 57% of the energy still comes from an exhaustible source like coal which also causes irreparable damage to the environment. Dependence on such a source for a long run is not feasible and hence the need to develop efficient means of using renewable sources like photovoltaic cell, wind power etc. arises.

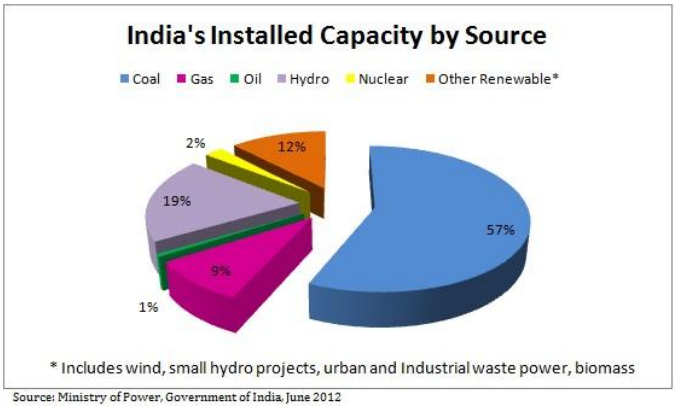

Figure 1.5. Pie chart showing contribution from different sources in India's total power production (Ministry of power, Government of India, June 2012).

a. Solar Energy as an Alternative

Choosing solar energy over other non-renewable sources will help to protect the environment and more importantly it is available free of cost. Conversion of solar energy into electricity is done using photovoltaic cells (PV) or solar cells, which work on the principle of photovoltaic effect. India gets abundant solar energy as it is located in the equatorial sun-belt of the Earth. Due to its favorable geographical position the daily average solar energy incident on India varies from 4 to7 kWh/m^2 with about 2300 to 3200 sunshine hours per year[27]. Theoretically this add up to have solar energy reception about 500 trillion kWh/year or 600 TW with about 300 clear sunny days a year[27].This is far more than the current total consumption. If we assume the

efficiency of solar cells is as low as 10%, this would still be a thousand times greater than the domestic electricity demand projected for the year 2015[27]. Taking into consideration all these positive points and advantages, the government has started investing money in projects to get maximum benefit from solar power. In 2007 the amount of energy produced using the solar energy was less than 1% of the total energy demand[28]. On the other hand India ranked number one in terms of solar energy production per watt installed, with as isolation of 1700 to 1900 kWh/kWp[29] in 2010. By the end of 2013 the installed grid connected photovoltaic had increased to 2.18 GW and in coming years it is projected to increase even further.

Although the production of solar cells has increased and there is an increasing awareness among people, it is difficult to make solar energy available at a low cost. If we compare the cost for production of 1 kWh energy from different sources then coal is the cheapest, at only Rs 2 to Rs 3 followed by photovoltaic cells fabricated using Silicon (Si) costing Rs 10 to Rs 15[30]. Si based solar cells are first generation solar cells. Though Si is abundant, currently producing low cost solar cells is a great challenge. The higher cost of Si based solar cells is mainly due to the processing of material to make it pure, crystalline and defect free. More than 95% of photovoltaic market is still dominated with Si based cells, whose efficiency is limited by Shockley Queisser's limit[31]. The figure 1.6 below shows the different losses that occur in bulk semiconductor p-n junction devices[32]. The only way to make solar cells affordable is to increase their efficiency at reduced fabrication/production cost per kWh.

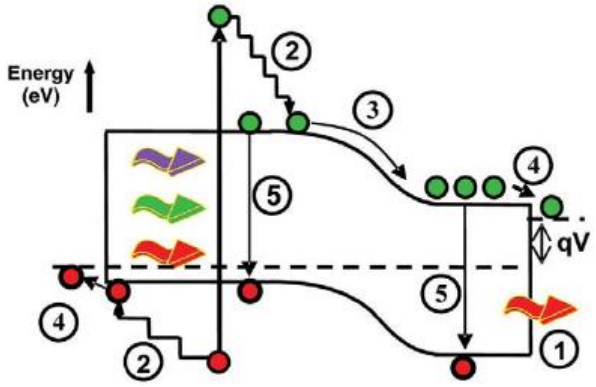

Figure 1.6. Loss processes in a standard solar cell. (1) Transmission of below band gap photons, (2) Photons with energy more than band gap lose their extra energy in thermalization, (3) Junction loss, (4) Contact loss, (5) Recombination loss either radiative or non-radiative[32].

Different techniques have been used in order to make solar cells affordable. One among them is the use of thin film technology. This is considered as a second generation solar cell. It is made up of deposition of one or more than one layers of photovoltaic material on the substrate. Material includes Copper Indium Gallium Selenide (CIS/ CIGS), Cadmium Telluride (CdTe), amorphous Silicon (a-Si) etc. Thickness of layer is varied from few nanometers to tens of micrometer. Actually, these cells can be fabricated at low cost compare to first generation cells but the efficiency is largely hampered by presence of defects due to dangling bonds at the surface[33]. The only promising approach to overcome all the above mentioned problems is the use of quantum dots as a photovoltaic material /photon absorber[34,35]. These types of solar cells come under third generation solar cells[33]. Theoretically it is possible to attain more than 80% efficiency[32,33] using multi junction cells under light concentration. Three different approaches have been proposed in order to increase efficiency:

1) Use of multiple band gaps materials (tuning of band gap is possible by varying size of QDs so one can use different sized QDs of same material)[8].

2) Multiple carrier generation per incident photon[10,11,36,37] or multiple low energy photons used to create one electron-hole pair.

3) Capturing carriers before thermalization[38].

Figure 1.7 below shows theoretically possible efficiency and projected cost for different generation solar cells[32].

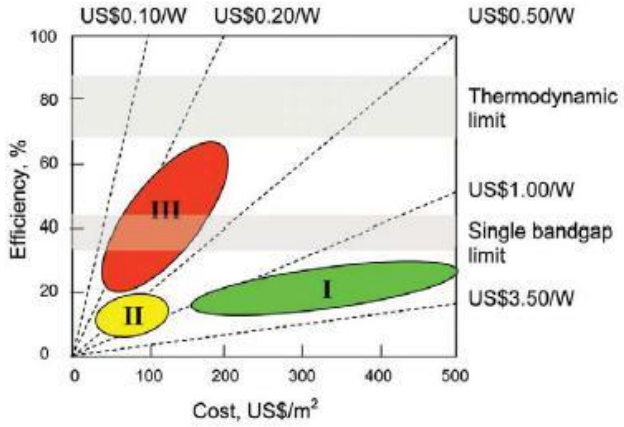

Figure 1.7. Theoretical efficiency and projected cost for 1st, 2nd and 3rd generation solar cell[32].

b. Working Principle of p-n Junction Solar Cells

The discovery of "photovoltaic effect" is dated back to 1839 by the French physicist Becquerel[39]. He observed that incidence of light develops/changes electrical potential between two silver coated platinum electrodes separated by some electrolyte. Since then, a variety of devices have been developed to convert light energy into electric energy. Generally when a photon is absorbed by a material an electron-hole pair is excited. The extra energy carried by these photo-generated carriers results in potential difference or electromotive force (e.m.f.) if these excited charge carriers can be collected and used to generate electrical energy. This force drives them through the electrical load to do work. Photovoltaic cells require built-in asymmetry in order to separate these generated charge carriers before they relax their energy through recombination and finally feed them to external circuit[33]as shown in figure 1.8.

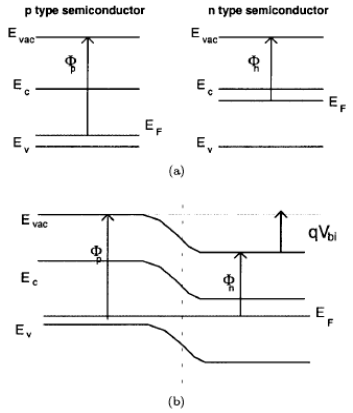

Figure 1.8. Band profile for p, n layers when separated. The difference in work-function due to different carrier concentration as a result of doping is visible. b) Band profile for p-n junction under equilibrium. The difference in work function creates an electrostatic field equal to $1/q^* \Delta E_{vac}$. Here V_{bi} is developed built-in potential in equilibrium. (Jenny Nelson, Physics of solar cell, Imperial college press)

This asymmetry can be created by materials with different electron affinity or with different work functions[40] as shown in figure 1.8. Without this asymmetry, energy cannot be extracted as the charge carriers will recombine very fast (~nanoSec). In case of semiconductors it is easily obtained by doping different regions of same material differently[40]. Here the work function of the p-type is large compared to n-type and subsequently an electric field is

established at the junction. A depletion layer is formed at the junction which acts as barrier to the majority charge carriers. Photo-generation drives minority charge carriers throughout the p and n layers and they reach the junction by diffusion.

VI. Sensitized Solar Cells

The sensitization was first reported in 1873 by Vogel[41]. He reported that the photosensitization extends to infrared by sensitization of silver halide with dyes. The photoelectric effect was then studied by using erythrosine on silver halide electrodes by Moser in 1887[42]. Till 1960 the mechanism for these processes was under dispute. In 1968 Tributsh et al. reported electron injection process[43] and then-after chemisorption of dyes on surfaces of semiconductor was studied in order to enhance the function of dye. Use of dye sensitized electrode in solar cell as photo-anode was invented by Michel Grätzel and Brian O'Regan at UC Berkeley in 1988. The first report was then published on dye sensitized solar cell in 1991[44] with efficiency ~7.1%. They used porous TiO_2 as the supporting layer on which the dye is chemisorbed. The evolution has been continued till now, with the highest efficiency achieved being 15% in DSSC with solid electrolyte[45].

Schematic for cell structure and working principle of DSSC is shown in figure 1.9. The cell structure consists of two metal electrodes, one of them required to be transparent as well as conducting. Generally a fluorinated tin oxide (FTO) coated glass is used as transparent conducting electrode and platinum (Pt) or gold coated glass is used as the other electrode. TiO_2 nanoparticles have been widely used as supporting material sensitized with the dyes as they are inexpensive, abundant, non-toxic as well as conducting etc. Dye is generally used as the photo-absorber or sensitizer by chemisorption on TiO_2, the TiO_2 thin film on FTO coated glass along with dye molecules adsorbed on it is called as photo-anode. A regenerative electrolyte is used in between photoanode and Pt electrode. This electrolyte is a combination of reducing and oxidizing species of the same element. The electrolyte is such that it can readily transfer an electron to an oxidized dye molecule[40].

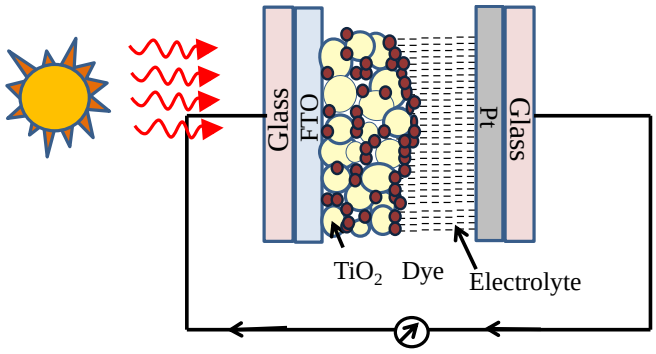

Figure 1.9. Schematic for sensitized device. Here FTO is transparent conducting glass. TiO_2 is supporting network for dye molecule. Dye molecules act as photo-absorber/ sensitizer. Electrolyte is used to neutralize oxidized dye molecule after charge transfer to FTO.

a. Working Principle for Sensitized Solar Cells

The figure 1.10 below shows charge transfer mechanism in sensitized solar cells[46]. The dye absorbs photons and a pair of charge carriers is generated. The electron gets transferred to TiO_2 which is sintered on FTO glass for electrical contact and further collected at FTO. The oxidized dye can be regenerated due to electron donation from the electrolyte to the dye. Electrolyte here is self-regenerated at the counter electrode by reduction of triodide/ oxidized species. Thus circuit is completed through external load. Efficiency of the device depends on the ability of the dye to absorb maximum solar spectrum, transfer of charge carriers without any hurdle in-between the dye and TiO_2, collection of charge carriers at the FTO without recombination with holes left in the dye as well as with electrolyte, transfer of electron from electrolyte to recycle the oxidized dye molecule and finally choosing the best metal as cathode which will not corrode in contact with the electrolyte[47]. In the coming sections of this thesis we will see how to resolve a few of these issues.

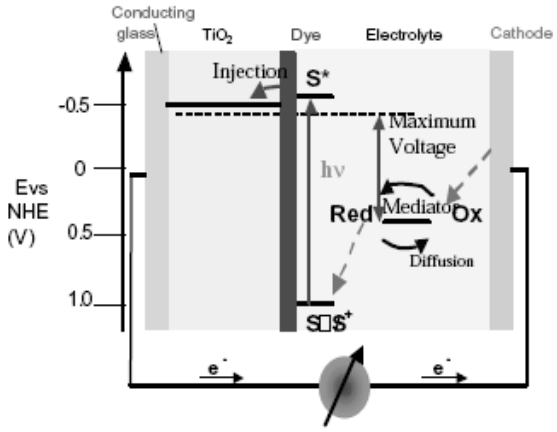

Figure 1.10. Schematic showing working principle and energy level scheme for sensitized solar cell[46].

b. The Quantum Dot Sensitized Solar Cells

Replacement of dye by semiconductor nanoparticles (i.e. QDs) as photo-absorber results in Quantum Dot Sensitized Solar Cell (QDSSC). The use of dye is said to have many disadvantages including toxicity, non-stability on exposure to UV wavelengths, higher cost due to the use of rare earth metals, synthesis and purification processes are difficult etc. To achieve the goal of affordability, higher efficiency and environmental friendly systems QDSSC is said to be better compared to DSSC[47,48]. Advantages of QDs as mentioned in section II will be useful for fabricating better solar cells. The very first report for replacing light absorbing dye with semiconductor includes use of CdS QDs adsorbed on TiO_2 colloids injects electrons into TiO_2 upon photo-excitation[49]. Since then there has been an increasing interest to use semiconductors as sensitizers[50,51,52,53].

VII. Aims of the Present Work

The main objective of this work is to describe a process to synthesize good quality semiconductor nanoparticles at low cost. We attempt to understand the growth processes, and also to reduce the steps for growth of QDs. Synthesis of good quality material and its use in application is the main aim of this thesis. The quality of the material and the performance of devices can be checked and analyzed using different techniques. In ***Chapter 2*** we will discuss

about the different techniques used for characterization of QDs and SSCs, and the precautions one has to take while conducting measurements. In ***Chapter 3*** we will understand how to synthesize good quality aqueous CdTe QDs and how the capping layer will help in adsorption of these QDs on TiO_2 layer. Here, we have found that the performance of the device is not good as CdTe undergoes self-destruction when it comes in contact with electrolyte. The need of having a shell layer for CdTe QDs in order to avoid direct contact with electrolyte will be discussed further. In connection to this problem we have discussed a synthesis procedure for type–II heterostructure in ***Chapter 4***, and given a protocol for CdTe/CdSe core/shell QDs synthesis using modified synthesis procedure. This procedure aims for reduced steps for synthesis and it is different compared to the usual synthesis procedure. It has been shown that the synthesized core/shell QDs are equally good in terms of optical and structural properties as that of those synthesized using the usual method. We have used these QDs as sensitizers in SSC and results have shown a many fold increase in efficiency compared to those experiments performed using just CdTe. In this chapter we have also emphasized the role of sintering photoanode as it helps in removing insulating capping layer and bridges the gap for better charge transportation. As sintering of photoanode results into agglomeration of QDs and it further decreases quantum effect we have discussed importance of having uncapped QDs. In ***Chapter 5*** we have briefly discussed use of uncapped $AgInS_2$ QDs and its application in SSCs. Work was done in collaboration with Dr. Angsjuman Nag's group in IISER-Pune. Here we have shown that the short circuit current density is affected due to the presence of defects. The increase in efficiency compared to other reported capped $AgInS_2$ QDs is emphasized in order to prove the importance of uncapped QDs. An effective size window for impact ionization in lead sulfide (PbS) QDs and experimental evidence for dispersive screening of coulomb interaction in hot excitons is explained in ***Chapter 6***. In ***Chapter 7*** we have discussed the dependence of measured hydrodynamic radius on excitation intensity. We have done this project in collaboration with Dr. Shivprasad Patil, IISER Pune. In this chapter we have addressed that one should not use hydrodynamic radius values without checking its dependence on excitation intensity. We have tried to explain the effect of blinking and based on the obtained results we have provided a novel approach to measure photo-induced dark fraction due to blinking. The probability of QD entering into dark state is calculated and the mechanism through which it occurs is also explained using

fluorescence correlation spectroscopy. At last in ***Chapter 8,*** we provide a summary of the research work done by us along with few thoughts on future directions.

VIII. References

[1] J. I. Pankove, Optical Processes in semiconductors, (Prentice-Hall Inc., Englewood Cliffs, New Jersey, 1971).

[2] R. S. Knox, Solid State Physics, edited by H. Ehrenreich and D. Turnbull (Academic Press, New York, 1963), vol . Suppl. 5.

[3] P. Y. Yu, and M. Cardona, Fundamentals of Semiconductors : Physics and Material Properties, 2nd eds, (Springer-Verlag, Berlin, 1999).

[4] J. Singh, Physics of Semiconductors and their heterostructures, (McGraw-Hill, Inc., Singapore, 1993).

[5] R. Rossetti, S. Nakahara, L. E. Brus, Quantum size effects in the redox potentials, resonance Raman spectra, and electronic spectra of CdS crystallites in aqueous solution. J. Chem. Phys., 79, 1086–1088, 1983.

[6] A. I. Ekimov, A. L. Efros, A. A. Onushchenko, Quantum size effect in semiconductor microcrystals. Solid State Commun. 56, 921-924, 1985.

[7] M. A. Reed, J. N. Randall, R. J. Aggarwal, R. J. Matyi, T. M. Moore, A . E. Westel, Observation of discrete electronic states in a zero-dimensional semiconductor nanostructure. Phy. Rev. Lett. 60 (6), 535-537, 1988.

[8] A. Kongkanand, K. Tvrdy, K. Takechi, M. K. Kuno, P. V. Kamat, Quantum dot Solar Cells. Tuning photo-response through size and shape control of CdSe-TiO_2 architecture. J. Am. Chem. Soc. 130, 4007–4015, 2008.

[9] A. J. Nozik, Quantum dot solar cells. Physica E, 14, 115-120 2002.

[10] E. Octavi, Semonin, J. M. Luther, C. Sukgeun, H.-Y. Chen, J. Gao, A. J. Nozik, M. C. Beard, Peak external photocurrent quantum efficiency exceeding 100% via meg in a quantum dot solar cell, Science , 334 (6062), 1530-1533, 2011.

[11] A. J. Nozik, Multiple exciton generation in semiconductor quantum dots, Chem. Phys. Lett. 457, 3-11, 2008.

[12] C. A. Leatherdale, W. –K. Woo, F. V. Mikulec, M. G. Bawendi, On the absorption cross section of CdSe nanocrystal quantum dots. J. Phys. Chem. B 106(31): 7619, 2002.

[13] L. Zhuang, L. Guo and S. Y. Chou, Silicon single-electron quantum-dot transistor switch operating at room temperature, Appl. Phys. Lett. 72, 1205, 1998.

[14] J. Kong, J. Cao, H. Dai and E. Anderson, Chemical profiling of single nanotubes: Intramolecular p–n–p junctions and on-tube single-electron transistors, Appl. Phys. Lett. 80, 73, 2002.

[15] Q. Sun, Y. A. Wang, L. S. Li, D. Wang, T. Zhu, J. Xu, C. Yang and Y. Li, Bright, multicoloured light-emitting diodes based on quantum dots, Nature Photonics 1, 717 – 722, 2007.

[16] A. Zrenner, E. Beham, S. Stufler, F. Findeis, M. Bichler and G. Abstreiter, Coherent properties of a two-level system based on a quantum-dot photodiode, Nature 418, 612-614, 2002.

[17] Y. Narukawa, Y. Kawakami, M. Funato, S. Fujita, S. Fujita and S. Nakamura, Role of self-formed InGaN quantum dots for exciton localization in the purple laser diode emitting at 420 nm, Appl. Phys. Lett. 70, 981, 1997.

[18] P. V. Kamat, Quantum dot solar cells. semiconductor nanocrystals as light harvesters, J. Phys. Chem. C, 112 (48), 18737–18753, 2008.

[19] I. Robel, V. Subramanian, M. Kuno and P. V. Kamat, Quantum dot solar cells. harvesting light energy with CdSe nanocrystals molecularly linked to mesoscopic TiO_2 films, J. Am. Chem. Soc., 2006, 128 (7), 2385–2393, 2006.

[20] T. S. Ahmadi, Z. L. Wang, T. C. Green, A. Henglein and M. A. El-Sayed, Shape-controlled synthesis of colloidal platinum nanoparticles, Science, 272, 1924-1925, 1996.

[21] A. L. Rogach, T. Franzl, T. A. Klar, J. Feldmann, N. Gaponik, V. Lesnyak, A. Shavel, A. Eychmuller, Y. P. Rakovich, and J. F. Donegan, J. Phys. Chem. C, 111, 14628-14637, 2007.

[22] http://cea.nic.in/reports/monthly/executive_rep/mar13/mar13.pdf (Central electricity authority, ministry of power, government of India, Nov. 2013, from Executive summery of the month of December 2013.)

[23] http://en.wikipedia.org/wiki/Electricity_sector_in_India#cite_note-cea13-1(International Energy Statistics, from Wikipedia.)

[24] World energy outlook 2011: Energy for all. International Energy Agency. Oct 2011.

[25] The Asian brown cloud: Climate and other environmental impacts, United Nations environmental programme 2002.

[26] http://en.wikipedia.org/wiki/Electricity_sector_in_India (Energy sector in India, Wikipedia,)

[27] T. Muneer, M. Asif and S. Munawwar, Sustainable production of solar electricity with particular reference to the Indian economy, Renewable and Sustainable Energy Reviews 9 (5), 444, 2005.

[28] http://www.ecoworld.com/products/electronics/indias-solar-power.html (R. Avilash, India's solar power: greening india's future energy demand, ecoworld.com. 15th may 2007.)

[29]http://articles.economictimes.indiatimes.com/2009-10-26/news/28443220_1_solar-power-renewable-energy-india-ranks (C. Tembhekar, India tops with US in solar power, Economic Times, 26th Oct 2009.)

[30] *http://www.solarpower.org.in/,(*An Overview of Solar Power – Today and Tomorrow)

[31] W. Shockley, H. J. Queisser, Detailed balance limit of efficiency of pn junction solar cells, J Appl. Phys. 32, 510, 1961.

[32] G. Conibeer, Third-generation photovoltaic, Materials Today, 10, 42-50, 2007.

[33] M. A. Green, Third Generation Photovoltaics, Ultra-high conversion efficiency at low cost, Prog. Photovolt: Res. Appl., 9, 123-135, 2001.

[34] P. V. Kamat, Quantum dot solar cells. Semiconductor nanocrystals as light harvesters, J. Phys. Chem. C, 112, 18737–18753, 2008.

[35] P. V. Kamat, Meeting the clean energy demand: Nanostructure architectures for solar energy conversion. J. Phys. Chem. C, 111, 2834–2860, 2007.

[36] R. D. Schaller, V. I. Klimov, High efficiency carrier multiplication in PbSe nanocrystals: implications for solar energy conversion. Phys. Rev. Lett., 92, 186601, 2004.

[37] R. D. Schaller, V. M. Agranovich and V. I. Klimov, High-efficiency carrier multiplication through direct photogeneration of multi-excitons via virtual single-exciton states. Nat. Phys., 1, 189–195, 2005.

[38] R. T. Ross and A. J. Nozik, Efficiency of hot-carrier solar energy converters, J. Appl. Phys., 53, 3813–8, 1982.

[39] A. E. Becquerel, Memoire sur les effets électriques produits sous l'influence des rayons solaires, C. R. Acad. Sci. Paris, 9, 561, 1839.

[40] J. Nelson, physics of solar cell, Imperial college press.

[41] W. West, First hundred years of spectral sensitization. Proc. Vogel Cent. Photogr. Sci. Eng. 18, 35, 1974.

[42]J. Moser, Notiz über Verstärkung photoelek-trischer Ströme durch optische Sensibilisirung. Monatsh. Chem., 8, 373, 1887.

[43] H. Gerischer, H. Tributsch, Ber. Bunsenges. Phys. Chem., 72, 437, 1968.

[44] B. O'Regan, M. Gratzel, A low cost high efficiency solar cell based on dye-sensitized colloidal TiO2 films, Nature,353 (6346), 737-740, 1991.

[45] J. Burschka, N. Pellet, S.-J. Moon, R. Humphry-Baker, P. Gao, M. K. Nazeeruddin and M. Gratzel, Sequential deposition as a route to high-performance perovskite-sensitized solar cells, Nature, 499, 316-319, 2013.

[46] Gratzel M, Sensitized solar cell, Journal of Photochemistry and Photobiology C: Photochemistry Reviews, 4, 145–153, 2003.

[47] G. Hodes, Comparison of dye- and semiconductor-sensitized porous nanocrystalline liquid junction solar cells, J. Phys. Chem. C, 112, 17778–17787, 2008.

[48] H. G. Agrell, J. Lindgren and A. Hagfeldt, Degradation mechanisms in a dye-sensitized solar cell studied by UV–VIS and IR spectroscopy, solar Energy, 75, 169-180, 2003.

[49] N. Serpone, E. Borgarello and M. Gratzel, Visible light induced generation of hydrogen from hzs in mixed semiconductor dispersions; improved efficiency through inter-particle electron transfer, J. Chem. Soc. Chem. Commun., 342, 1984.

[50] L. Spanhel, H. Weller and A. Henglein, Electron injection from illuminated CdS into attached TiO_2 and ZnO Particles J. Am. Chem. Soc., 109, 6632, 1987.

[51] S. Hotchandi and P. V. Kamat, J. Phys. Chem., 96, 6835, 1992.

[52] A. Ennaoui, S. Fiechter, H. Tributsch, M. Giersig, R. Vogel and H. J. Weller, Electrochem. Soc. 139, 2514, 1992.

[53] R. Vogel, P. Hoyer, H. Weller, Quantum-Sized PbS, CdS, Ag2S, Sb2S3 and Bi2S3 particles as sensitizers for various nanoporous wide- bandgap semiconductors, J. Phys. Chem., 98, 3183, 1994.

Chapter 2

Experimental Techniques for Optical, Structural and Electrical Characterization

Synthesis of good quality nanomaterials is important in order to manufacture high quality novel applications. However, the quality of nanomaterials and the performance of nano-devices can only be checked using different characterization techniques. In this chapter, we will try to understand the basics of these characterization techniques and how one can use them to study optical, structural and electronic properties of semiconductor quantum dots (QDs). We will also discuss the precautions one has to take while measurements are being conducted.

I. UV-VIS Optical Absorption Spectroscopy

UV-VIS optical absorption spectroscopy is one of the most important and well known techniques to characterize possible electronic transitions within a material which provide important clues for its optical and electronic quality. Allowed photo-excitations from lower energy valence states to available higher energy conduction states can be used to explore the electronic structure of semiconductor quantum dots and this can be studied using optical

absorption spectroscopy. In case of QDs, quantum confinement of charge carriers causes the discreteness in energy levels in both the bands and at the same time the effective energy gap also increases. UV-VIS spectrometer can easily track these photo-induced electronic transitions and so the increase/decrease in effective energy gap of nanoscale materials with change in size without any trouble. The ease of operation and affordability of the instrument have made this technique especially popular. A typical set up for the UV-VIS absorption spectrometer is as given in figure 2.1.

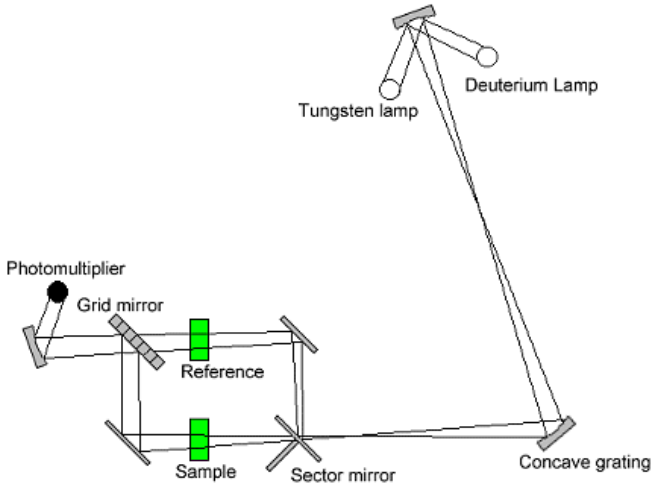

Figure 2.1. A typical set up for dual beam UV-VIS Absorption spectrometer[1].

Here, absorption of electromagnetic radiation causes transitions from filled initial valence states to empty final states if the energy of the photon matches with fundamental band gap of material and the probability of transition is called as absorption coefficient α(E). This is calculated as the relative rate of decrease in the incident intensity I_O along its propagation path in the material $(x)^2$.

$$\alpha(E) = \frac{-1}{I_O}\frac{d[I_O]}{dx} \qquad (2.1)$$

Absorption coefficient α(E) of a material also depends on the wavelength (λ) of incident photon and extinction coefficient (κ) of a material by equation,

$$\alpha(E) = \frac{4\pi\kappa}{\lambda} \qquad (2.2)$$

Extinction coefficient is a property of a material and it measures how strongly a substance absorbs a particular wavelength of light. It is represented by the unit $M^{-1}cm^{-1}$. The Absorbance A is thus related to the Incident intensity (I_O), transmitted light intensity (I_T), concentration of a solution (c), path length of the sample (L) and absorption coefficient α(E) by following equation,

$$A = \ln \frac{I_O}{I_T} = \alpha(E) \times L \qquad (2.3)$$

In case of QDs, the first excitonic peak absorption wavelength (λ) can be used to calculate the radius (R) of the QDs using Effective Mass Approximation (EMA) formula[3,4,5].

$$E = \frac{hc}{\lambda} = E_g + \frac{1}{R^2}\left(\frac{h^2}{8\pi^2 m_\mu}\right) - \frac{1}{R}\left(\frac{1.786e^2}{4\pi\varepsilon_0}\right) - 0.248\frac{4\mu\pi^2 e^4}{h^2 {\varepsilon_0}^2} \qquad (2.4)$$

Here, E is the first excitonic peak absorption energy of QDs, E_g is the bulk band gap of the material, R is the radius of QD, h is Plank's constant in eV, c is velocity of light, $m_\mu = \left(\frac{m_e^* m_h^*}{m_e^* + m_h^*}\right)$ is reduced mass of electron and hole, m_e* and m_h* are effective mass of electron and holes respectively in M.K.S units, ε_0 is static dielectric constant of the material, π is mathematical constant and e is absolute electric charge. In our experiments, we have used the optical absorption spectroscopy to find out first excitonic peak absorption wavelength and further used this EMA formula to calculate size of QDs. Figure 2.2 below shows the absorbance spectra for CdTe QDs of different sizes[6] (the size noted here is calculated using EMA formula excluding the self- energy term).

Perkin Elmer lambda 950, UV-VIS-NIR spectrometer with step size in-between 0.2-0.5nm/sec is used for studying the absorption spectra of different QDs. Proper precautions have been taken during measurements. For instance,

1. We have used a quartz cuvette throughout the experiments. Care has been taken to always use a cleaned and unscratched cuvette.

2. Over-concentrated or turbid solutions have not been used, in order to avoid losses in transmission due to scattering.

3. Data represented in this thesis is always corrected for background errors. Background correction has been done by recording absorption for a solvent which is also used as reference and subtracting sample's spectra from the reference spectra. In some cases we have also recorded the spectra of the solvent with air as background and represented it along with main data in order to avoid any misjudgment.

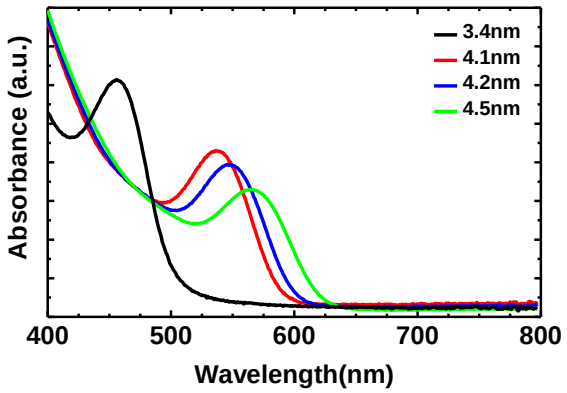

Figure 2.2. Absorption Spectra for different size CdTe QDs synthesized in our lab using aqueous medium at low temperature[6].

II. Photoluminescence Spectroscopy

Photoluminescence (PL) is emission of photons which occurs due to relaxation of excited electrons from higher energy levels to lower energy levels. The emitted light is collected and spectral distributions are measured in order to understand the processes. The emission of energy happens at low energies compared to the absorption and the shift from absorption wavelength is called as Stokes shift[7]. The Stoke shift is mainly due to thermalization of charge carriers, solvent effect and presence of defects etc[8]. PL is considered as an important technique in understanding the optical quality of a material, as the non-radiative processes due to the presence of any defects competes with the radiative processes. In order to record the PL spectra, the sample is excited by photons of wavelength equal to or less than the absorption peak wavelength and the emission from the sample is collected. A typical setup for the PL spectroscopy is given in the figure 2.3. It has been used frequently in order to understand the radiative/non-radiative processes as well as to calculate the PL quantum yield (QY) of fluorescent materials. PL QY measures emitted

number of photons as a fraction of the incident number of photons. Figure 2.4 shows emission spectrum for 4.5 nm CdTe sample excited at wavelength 560 nm[9].

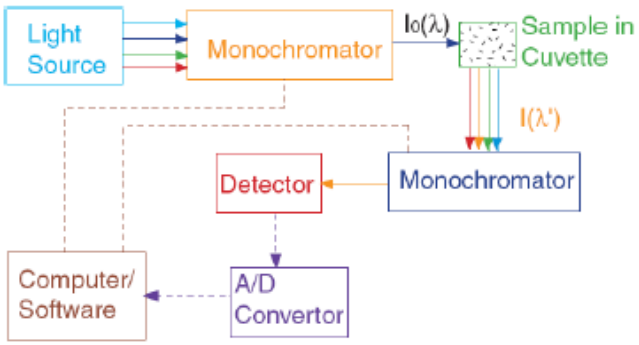

Figure 2.3. Cartoon showing the basic instrumentation setup of Photoluminescence spectroscopy[8].

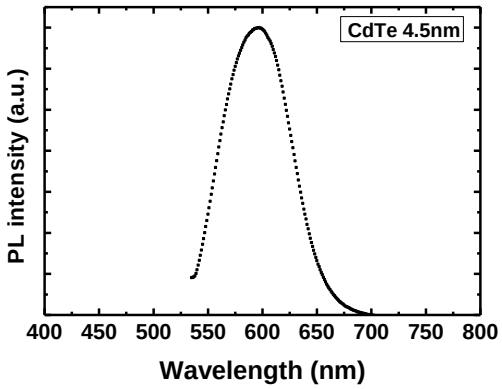

Figure 2.4. Photoluminescence spectrum for 4.5 nm CdTe QDs excited at 560 nm wavelength[9].

We have also measured the PL QY for QDs. PL QY is calculated for QDs by exciting the sample using a particular wavelength, generally at a higher wavelength than the band gap of material and collecting the PL spectrum. The resultant PL peak intensities are further used to calculate QY using the following formula[8]-

$$Q_s = Q_r \frac{A_s}{A_r} * \frac{OD_r}{OD_s} * \frac{n_s^2}{n_r^2} \qquad (2.5)$$

Here, Q_s is QY of sample, Q_r is PL QY of the standard reference material, A_s is the area under the curve of PL for the sample, A_r is the area under the curve of PL for the standard reference

material, OD_r is the optical density for the standard reference sample, OD_s is the optical density for the sample (it is taken from respective excitonic absorption spectra), n_r and n_s are the refractive indices of the solvent for both reference and sample.

We have used Fluorolog-3 from Horiba Jobin Yvon to record PL spectra of QDs. Precautions taken while conducting these QY measurements are: use of freshly prepared samples which are diluted using the same solvent such that all colloidal solutions should have a similar absorbance (~0.1 OD) at particular wavelength in order to correct its dependence on absorption.

III. Time Resoled Photoluminescence by Time Correlated Single Photon Counting

Time Correlated Single Photon Counting (TCSPC) technique is generally used to study lifetime of charge carriers in its excited state. The photo-excitation results in transition of charge carriers from lower filled state to empty higher states and while relaxing from higher energy state the analysis of time resolved decay of PL gives information related to lifetime of charge carriers[8,10]. Sample is generally excited by pulsed laser or LED. Time decay of PL after photo-excitation is recorded using a detector. The decay rate of the process is finally plotted as intensity vs. time graph. A typical setup for the TCSPC spectroscopy is as shown in figure 2.5.

We have used this technique to calculate the average lifetime of charge carriers in QDs. The photoluminescence decay for QDs is generally studied by exciting sample at higher energy than absorption energy of the material and collecting data using TCSPC. The data is tail-fitted using a single or multi-exponential decay equation (2.6). Best fit is selected such that fitting will give small residuals and a reduced chi-squared parameter (χ^2) approaching one[8].

$$I(t) = a_1 \exp\left(t/\tau_1\right) + a_2 \exp\left(t/\tau_2\right) + ... \quad (2.6)$$

Here, τ_1, τ_2, τ_3 ….. are the photoluminescence decay constants obtained from data analysis and a_1, a_2, a_3, …. are the corresponding pre-exponential factors. The average PL lifetime τ_{avg} can be calculated by taking intensity-weighted sum of the obtained lifetime components.

We have measured PL decays by using TCSPC setup from Horiba Jobin Yvon IBH, USA. As a pulse excitation source we have used 405 nm photo-excitation source from IBH, UK (NanoLED-405L). The photoluminescence signals are collected by Fluorolog-3 at a magic angle

polarization of 54.7˚ using a MCP-PMT detector from Hamamatsu, Japan. The analysis or fitting of the data is done using Horiba Jobin Yvon's IBH DAS6 decay analysis software. Care has been taken to keep photon count rate low (less than 1% of excitation rate) in order to make sure that the decay is not biased to early arriving photons.

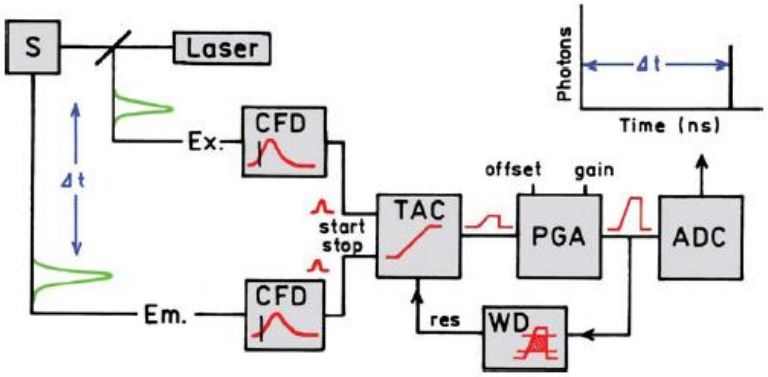

Figure 2.5. A typical TCSPC setup[8].

IV. Fluorescence Correlation Spectroscopy

Fluorescence Correlation Spectroscopy (FCS) is invented in 1972 by Magde, Elson, and Webb[11]. It is a very sensitive technique, used for detection of small molecules. In this technique fluorescence from a very tiny space (~1 μm^3) and from a very dilute sample (nanomolar to picomolar concentration) is detected[8]. We have collaborated with Dr Shivaprasad Patil's laboratory in IISER-Pune where a home-built FCS setup having diode laser photo-excitations of 532 nm and 450 nm respectively was used for the study. LABVIEW was used for recording correlated data on a computer. The typical set up for FCS used in our measurements is shown in figure 2.6[8,12,13,14].

The theory of FCS is based on Poisson's distribution in which the average number of particles residing in the detection volume can be determined from a random event. Particles in colloidal solution undergo diffusion due to Brownian motion, and this diffusion causes fluorescence fluctuation in the detection volume.

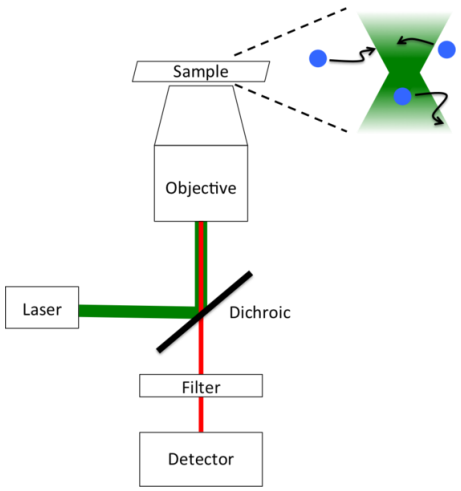

Figure 2.6. Schematic showing a typical FCS setup[8,12].

The temporal correlation of this fluorescence fluctuation is analyzed to get information like the diffusion time (τ_D), the hydrodynamic radius (R_H), the average number of particles in the detection volume (N) and the concentration of the solution used (C) etc. For normal 3D diffusion the autocorrelation function is given as[8]_

$$G(\tau) = G(0)\frac{1}{\left(1+\left(\tau/\tau_D\right)\right)\left(1+a^{-2}\left(\tau/\tau_D\right)\right)^{1/2}} + G(0) \tag{2.7}$$

Here, 'a' is the ratio of axial to the radial diameter, 'τ_D' is characteristic residence time and 1/G(0) is the mean number of diffusers in the detection volume. Radial dimension (r) of the detection volume is estimated using the following relation as the diffusion coefficient (D) for a standard chromosphere is known[8]_

$$r^2 = 4D\tau_D \tag{2.8}$$

Using this information, hydrodynamic radius of a diffusing particle can be calculated using Stokes-Einstein relationship as[8]_

$$R_H = \frac{kT}{6\Pi\eta D} \tag{2.9}$$

Here, k is the Boltzmann constant, T is the temperature, η is the viscosity of the solvent and D is the diffusion coefficient. In ***Chapter 7*** we will see how the hydrodynamic size of QDs depends on the intensity of excitation source and why one should be careful while using information regarding it[6].

V. X-Ray Diffraction

Study of crystal structure and calculation of crystallite size of QDs can be done using powder X-ray Diffraction (XRD). It has been used as one of the important tools as it helps in understanding crystal structures of variety of samples. X-rays are electromagnetic radiations. They undergo elastic scattering while interacting with electrons in an atom. As a crystal consists of a periodic arrangement of atoms, the interaction of X-rays with a crystal produces periodic scattered rays. The interferences of these scattered rays will be constructive in specific directions and destructive otherwise[15]. The angle for constructive interference can be determined by using Bragg's law[15]_

$$n\lambda = 2d\sin\theta \tag{2.10}$$

Here, λ is wavelength of X-ray beam, θ is the incident angle, d is interatomic distance of the crystal and n is any integer. The obtained scattering pattern is plotted as intensity vs 2θ angle as shown in figure 2.7(the plot shown here is X-ray diffraction for different sizes of lead sulfide QDs[16]).

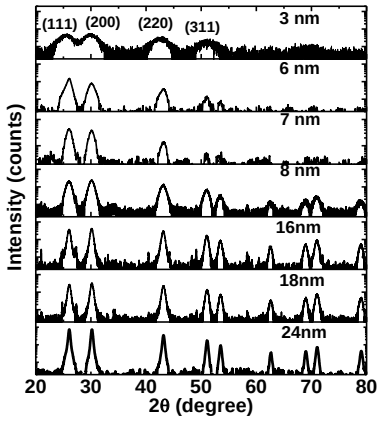

Figure 2.7. X-ray diffraction pattern for different size PbS QDs[16].

In case of powder XRDs many factors contribute to the observed peak profile i.e. broadening of the peak happens as a result of crystallite size, micro-strain present in the crystals as well as the temperature related broadening factor. In case of QDs, the long range order of periodicity is absent (as the size is not infinite as compared to that of bulk materials). Thus, destructive interferences of scattered intensities will not cancel out and as a result the peak

becomes broader upon reducing the size of QDs. We have used Debye Sheerer formula [15,17,18,19], to calculate crystallite size of QDs. This formula is only applicable to small particles with sizes ~100 nm or less than that.

$$\tau = K\lambda / \beta \cos\theta \tag{2.11}$$

Here, K is the shape factor (~0.9 for spherical QDs), λ is the wavelength of X-rays, β is the line broadening at half maximum intensity i.e. FWHM (Full Width at Half Maxima of a particular peak) and τ is the mean crystallite size of QDs. The increased full width at half maximum intensity (FWHM) value is used to calculate the crystallite size using formula 2.11. To get average crystallite size the values of FWHM and corresponding 2θ values from all prominent peaks for a given spectrum are used and average of all is considered. The size noted in the above figure 2.4 is calculated using Debye Shererer formula only assuming that there is no instrument related and strain related broadening.

Apart from crystallite size, the presence of micro-strain due to dislocations, domain boundaries and surfaces also produces a broadening in the peak profile. In case of QDs the ratio of the surface area to volume is more compared to its bulk structure, so it is prone to have more strain related broadening. Williamson-Hall first developed a method to determine the contribution from strain[20, 21]. The peak profile due to strain varies as _

$$\beta(2\theta) = 4\varepsilon \sin\theta / \cos\theta \tag{2.12}$$

Here, β is the integral breadth at the angle 2θ (θ being measured in radians). It is calculated by considering a rectangle with the same height and area as the diffraction peak, ε is the weighted average strain. Plotting βcosθ on the y-axis and 4sinθ on the x-axis will result in the Williamson-Hall plot. On a linear plot the intercept on the y-axis gives the average crystallite size and the slope of the graph is the weighted average strain present in QDs.

We have used Bruker D8 advanced X-ray diffractometer with Cu- k_α as a source (λ= 0.154 nm) and increment 0.01˚ per step. Crystallite size and information regarding strain in QDs is calculated using both Debye-Sheerer formula as well as Williamson-Hall method. In order to study powder XRD for QDs we have always used a thin film of purified QDs. Thin film is made on plane clean glass by drop casting colloidal solution of QDs. Precautions have been taken to

not heat the sample while evaporating the solvent and all contribution from k_β has been removed from the data presented in this thesis.

VI. Dynamic Light Scattering

Hydrodynamic size distribution profile of small scale particles suspended in colloidal solutions can be determined using Dynamic Light Scattering (DLS). This technique uses information of scattered light from small molecules/QDs whose size is less than or compared to the wavelength of light. The light used in this technique is from laser and hence is monochromatic and coherent in nature. As the particle undergoes Brownian motion the scattered light intensity shows time dependent fluctuations and this scattered intensity undergoes constructive or destructive interference with scattered light from the surrounding particles. A time dependent autocorrelation function is used to correlate data and the diffusion coefficient can be measured[22,23]. Stoke - Einstein equation is used which gives relation between size of particles and its speed due to Brownian motion.

We have used nanoseries Zetasizer ZS90 DLS instrument to get information about hydrodynamic size of nanoparticles/QDs. DLS experiments are carried out at 25 $^{\circ}$C using 633 nm, 3 mW He-Ne laser using 90 $^{\circ}$ optics having 10 μm apertures. A typical size distribution graph generated in this technique is always distribution of size (i.e. diameter) on the X axis and Y axis can be relative intensity of the scattered light or relative volume distribution of the particles or relative number distribution of the scattered particles. We have used information with relative number distribution and its corresponding diameter of QDs. We have repeated the measurement thrice and collected distribution data is averaged using Origin software to get final size distribution. Care has been taken during measurements to use very dilute samples without any dust present in it. Cuvette used in all measurements is clean and without any scratch on it. A fresh sample is always used for measurement. To study time dependent changes in the size distribution we have used same sample at different time interval.

VII. Scanning Electron Microscopy

Scanning electron microscopy (SEM) is one of the widely used and popular techniques for studying microstructural topography, morphology and for chemical composition analysis.

The light waves have limitations in obtaining resolution, due to diffraction and interference. So it cannot be used in general to resolve images with sizes less than the wavelength of light. However electrons with very small wavelengths undergo elastic or non-elastic scattering while interacting with the sample[24,25]. Figure 2.8 below shows different interactions of the incident electron beam with the sample[2424,25]. The elastic scattering of electrons from the outermost orbital electrons of the sample generates back scattered electrons (BSE). BSE provides compositional and topographical information of sample. The inelastic scattering of electrons from the sample produces secondary electrons (SE). These electrons are emitted from excited atoms. As the SEs have very low energies, they can escape from the region to just within a few nanometers of the material's thickness. Figure 2.9 shows SEM image for porous TiO_2 thin film.

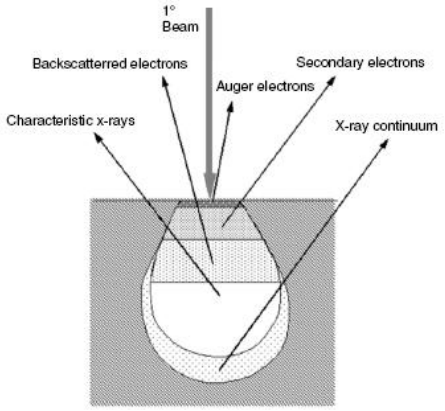

Figure 2.8. Illustration of interaction of electron beam with specimen in Scanning Electron Microscopy[24].

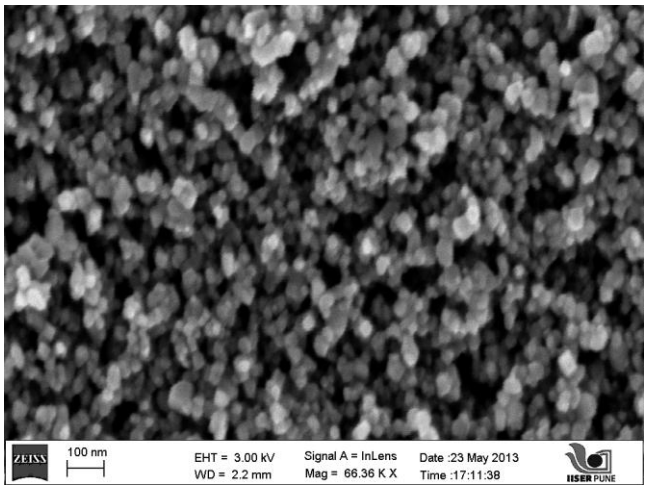

Figure 2.9. SEM image showing porous nature of TiO_2 thin film.

Apart from this, scattering electrons also interact with the sample and produce characteristic X-rays, Auger electron, cathodo-luminescence etc. The chemical composition determination or elemental analysis (atomic fraction) of any sample can be done using X-rays generated in SEM and the accessory is generally called as Energy Dispersive X-ray Spectroscopy (EDAX). When high energy electrons bombard onto the sample, an inner shell electron is displaced, an outer shell electron may fall into the inner shell to balance the created vacancy. Thus X-rays are emitted which are characteristics of a particular material and can be used reliably for elemental analysis. The topographic study and the elemental analysis for samples are done using a Carl Zeiss Ultra Plus system operated at 10 kV. We have used this technique to study the porous structure of TiO_2 thin films in sensitized solar cell. Chemical composition of the material after annealing and before annealing is also studied using EDAX and presented in ***Chapter 4***.

VIII. High Resolution Transmission Electron Microscopy

High Resolution Transmission Electron Microscopy (HRTEM) is an advanced imaging tool which allows direct imaging of the atomic structure of the sample. The highest resolution obtained using this technique is ~ sub-nanometer. In this microscopy an electron beam is transmitted through an ultra-thin specimen. While interacting with the specimen, as the electron beam passes through, the image is magnified and focused on fluorescent screen or captured using CCD camera[24,25]. We have done the structural investigation of the QDs using a JEOL JEM 1200 EX HRTEM instrument operated at an accelerating voltage of 200 kV. Samples are prepared by drop casting very dilute solutions onto copper grids (CF400-Cu, purchased from Electron Microscopy Science) with a carbon support in the air at room temperature and further preserved in vacuum desiccator at room temperature. Diameter of the QD is analyzed using 'ImageJ' software, this software provide a cursor using which one can measure length or breadth of a structure's image[26]. For most of the cases in our synthesis we get spherical QDs so we have used this software to measure diameter of QDs. The procedure is repeated and the values are averaged to minimize the error. The average QDs diameter is assessed via statistical analysis of measured HRTEM images of these QDs. The representative HRTEM image for CdTe/CdSe core/shell QDs synthesized in our lab is shown in figure 2.10[9].

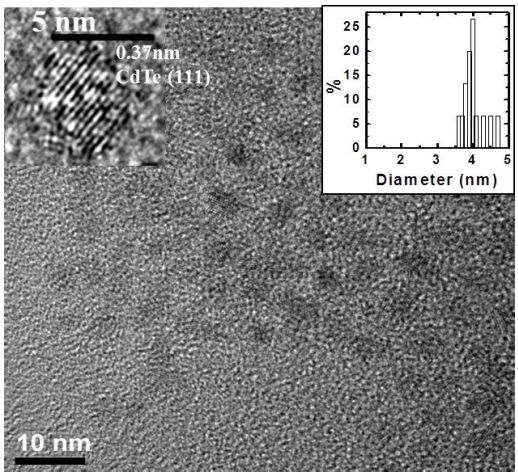

Figure 2.10. HRTEM image for CdTe/CdSe core/shell QDs[9].

IX. Photovoltaic Cells Characterization using Current– Voltage Measurements

Solar cell can be characterized by applying a varying bias and measuring the change in the current under light (under 1sun with AM 1.5 filter) and in dark. This study is generally called as the current-voltage (I-V) characteristic. Below we have discussed how solar cells respond under specific conditions[27,28]. Before explaining I-V characteristic we will see how to get uniform light and why AM1.5G filter and one sun condition is necessary[29]. The effect of parasitic resistances on the performance of solar cells is also discussed at the end of this section.

IX. a. Solar Spectrum and Air Mass 1.5G

The efficiency of solar cell is sensitive to incident solar power as well as spectrum of light and the intensity of light is not constant during all seasons, at all the times in the day as well as in all the parts of the world. The standard solar spectrum is given below in the figure 2.11 in comparison with extra-terrestrial and black body spectrum.

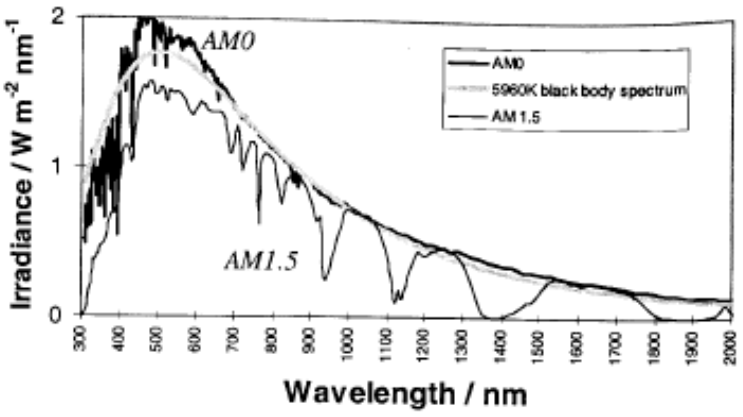

Figure 2.11. Extra- terrestrial solar spectrum compared with the 5760 K black body spectrum reduced by factor 4.6X 10^4 and with standard terrestrial solar spectrum[27].

To facilitate accurate comparison between solar cells measured at different times and location, a standard spectrum and power density is defined[29]. The standard solar spectrum at the Earth's surface is called AM 1.5G, here G is global which includes both direct and diffuse radiation and AM is Air Mass. Air Mass is the path length which light takes through atmosphere normalized to shortest possible path length. It is given by[29]_

$$AM = 1/\cos\theta \qquad (2.13)$$

Here, θ is the angle from vertical (zenith angle). The standard spectrum for temperature latitude is AM1.5, corresponding to the sun being at angle of elevation 42° [27]. This quantifies reduction in the power of light as it is absorbed by air, dust, H_2O, CO_2 etc. while passing through the atmosphere. The calculation gives approximately 970 W/m^2, for convenience of the round number this value is normalized to 1 KW/m^2 and generally referred as 1Sun intensity.

b. Solar Cells Characterization Using I-V Measurement

Electronically Solar cell is equivalent to a current generator in parallel with an assymetric, nonlinear resistive element i.e. diode as shown in figure 2.12. Ideal cell produces a photocurrent which is divided between variable resistance of the diode and the load.

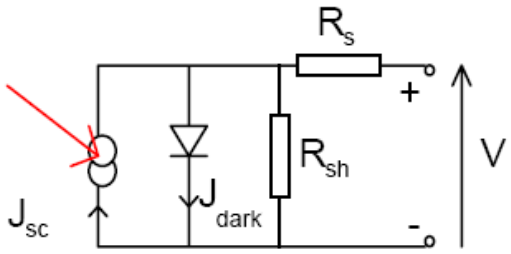

Figure 2.12. Equivalent circuit diagram of a solar cell with shunt and series resistance [27].

The characterization of the solar cells i.e. behavior of equivalent circuit diagram upon illumination and in the dark is as explained below.

IX.b. 1. Solar Cells in the Dark

a) At Equilibrium

Current density through any external load across the solar cell is zero When no bias is applied (V=0) and the cell is not illuminated.

b) Under Applied Bias

When a bias is applied under dark, majority charge carriers are able to move across the junction due to reduced built-in potential. Current flows due to drift of photo-generated electrons and holes. The current density for a cell with applied bias and under dark (J_{dark}) is as shown in figure 2.6 which follows the ideal diode equation[27]

$$J_{dark} \approx J_0 \ (e^{qv/k_BT} - 1) \qquad (2.14)$$

Here, J_{dark} is current density in the dark, J_0 is constant, k_B is Boltzmann's constant, T is temperature is degree kelvin, V is applied bias and q is absolute value of electron charge.

IX. b. 2. Solar Cells under Light

a) At Equilibrium

When the junction is illuminated, an electron-hole pair is created and quasi Fermi levels for an electron- hole splits. The electric field separates charge carriers and forces them to diffuse across the junction. So the current density flows without any applied bias i.e. short circuit current

(I_{SC}). This is the maximum current a cell can produce and as the current depends on materials it is important to measure short circuit current density (J_{SC}) i.e. current per unit area.

b) Under Applied Bias

When a bias is applied to a cell under light the current voltage response is approximated as the sum of short circuit photo-current and dark current and generally given by the equation 2.15[27].

$$J_V = J_{SC} - J_{dark} = J_{SC} - (e^{qv/k_BT} - 1) \tag{2.15}$$

Here, J_V is current density under applied bias, J_{SC} is short circuit current density and J_{dark} is current density under applied bias in the dark. When the contacts are isolated the potential difference is at its maximum value and is called as open circuit voltage (V_{OC}). This state occurs when dark current exactly cancels out the short circuit current. For the ideal diode condition the open circuit voltage is given by equation 2.16[2727,28].

$$V_{OC} = \frac{kT}{q} \ln\left(\frac{J_{SC}}{J_0} + 1\right) \tag{2.16}$$

The J-V characteristic for a solar cell in all the above mentioned conditions is shown below in figure 2.13. One cannot run a cell at V_{OC} or at J_{SC} as the power output at these points is zero. However, the operating regime for a solar cell is between 0 and V_{OC} where the output power is negative which specifies cell can deliver power. The maximum power one can obtain from the cell is at a point where product of current density and corresponding voltage is maximum i.e. maximum/peak power point as shown in figure 2.13. Maximum power density is shown by the inner rectangle in figure 2.13. The fill factor (FF) for solar cell is defined as squareness of the J-V curve and given by equation 2.17.

$$FF = \frac{J_m \times V_m}{J_{SC} \times V_{OC}} \tag{2.17}$$

Here, FF is fill factor, J_m is maximum current density, V_m is maximum voltage obtained. The efficiency for a solar cell is the maximum power obtained from the cell as a fraction of the incident light power density ($P_{incident}$).

$$\eta = \frac{J_m \times V_m}{P_{incident}} \tag{2.18}$$

Or $$\eta = \frac{J_{SC} \times V_{OC}}{P_{incident}} \times FF \qquad (2.19)$$

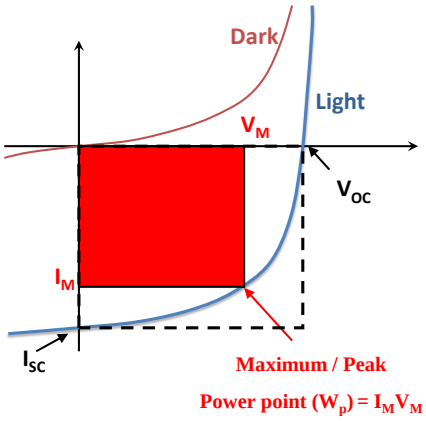

Figure 2.13. I-V characteristic for a solar cell in dark and under light. Maximum power from the cell can be calculate using values of voltage corresponding to maximum current[27].

IX. c. Parasitic Resistances

Power is dissipated through contacts as well as due to the presence of defects in real devices. These dissipations are equivalently denoted by the presence of series resistance (R_S) and parallel or shunt resistance (R_{Sh}). The series resistance arises due to presence of any barrier for current flow. It includes defects, the material's inherent property, resistive contacts etc. Shunt or parallel resistance generally arises due to the leakage of current through the cell, around the edges and between contacts of different polarity[30]. The fill factor and hence the efficiency of the cell will be affected because of the presence of these parasitic resistances. For an efficient solar cell R_S should be as small as possible and R_{Sh} should be very high. After considering contribution from parasitic resistances the diode equation becomes[27]_

$$J_V = J_{SC} - J_{dark} = J_{SC} - J_0\left(e^{q(V+J_V A R_S)/k_B T} - 1\right) - \frac{V + J_V A R_S}{R_{SH}} \qquad (2.19)$$

We have used Scientech Solar simulator with AM 1.5G and 100 mW/cm^2 intensity. Keithley 2611 source meter and LabView based program is used for I-V measurement of solar cells. Cells

are always checked in the dark room to avoid effect from stray light. After collecting the data the analysis is done using the software provided along with solar simulator. In that software equation 2.17 is fitted for the obtained I-V characteristics to get information about $R_{S,}$ R_{SH} and FF.

X. Conclusions

We have used the above discussed techniques to study optical, structural and electrical properties of QDs synthesized in our lab. The UV-VIS absorption technique is used to track the absorption spectra of the synthesized QDs. The PL capability of the QDs has been studied using PL spectrometer. We have also calculated the PL QY of these QDs. The PL lifetime of the charge carriers in the QDs is analyzed using decay data obtained in TCSPC. Average hydrodynamic radius of the QDs is studied using FCS and DLS. The intensity dependent behavior of the QDs is further explained using FCS. The study of crystal structure and average crystallite size calculation is done using XRD. The XRD data is also used to analyze presence of strain in the crystals using W-H analysis. Topography, morphology and chemical composition of QDs is studied using SEM and HRTEM. Further these microscopy techniques have been used to analyze size of the QDs. We have used the synthesized QDs for applications as sensitized solar cells. The performance of the device is checked using I-V characteristics.

XI. References

[1] http://teaching.shu.ac.uk/hwb/chemistry/tutorials/molspec/uvvisab3.htm

[2] H. H. Wilard, L. L. Meritt Jr., J. A. Dean and F. A. Settle, Instrumental methods of analysis, CBS publisher.

[3] L. Brus, Electronic Wave Functions in Semiconductor Clusters: Experiment and Theory. J. Phys. Chem. 90, 2555–2560, 1986.

[4] Al. L. Efros and M. Rosen, The electronic structure of semiconductor nanocrystals, Annu. Rev. Mater. Sci., 30, 475–521, 2000.

[5] W. W. Yu, L. Qu, W. Guo, and X. Peng, Experimental Determination of the Extinction Coefficient of CdTe, CdSe, and CdS Nanocrystals, Chem. Mater. 15, 2854-2860, 2003.

[6] A. V. R. Murthy, Padmashri Patil, Shouvik Datta, and Shivprasad Patil, Photoinduced Dark Fraction Due to Blinking and Photodarkening Probability in Aqueous CdTe Quantum Dots, J. Phys. Chem. C, 117, 13268−13275, 2013.

[7] G. G. Stokes , On the change of refrangibility of light. Phil TransR Soc (London) 142:463–562, 1852.

[8] R. Joseph, J. Lakowicz, Principle of fluorescence spectroscopy, 2nd Ed., Kluwer Academic, New York, 1999.

[9] Padmashri Patil, Clan Latlanzuala, Shouvik Datta, Sensitized solar cell from Type-II CdTe/CdSe core/shell nanocrystals synthesized without seed purification at low temperature, J. Alloys and Comp., 607, 230-237, 2014.

[10] http://www.picoquant.com/images/uploads/page/files/7253/technote_tcspc.pdf

[11] D. Magde, E. L. Elson, W. W. Webb, Thermodynamic fluctuations in a reacting system: Measurement by fluorescence correlation spectroscopy, Phys. Rev. Lett., 29, 705–708, 1972.

[12] J. Widengren and U. Mets, Conceptual basis of fluorescence correlation spectroscopy and related techniques as tools in bioscience. In Single molecule detection in solution, 69–120. Edited by C. H. Zander, J. Enderlein, R. A. Keller. Wiley-VCH, Darmstadt, Germany. 2002.

[13] N. L. Thompson, Topics in fluorescence correlation spectroscopy, volume 1, springer.

[14] https://www.dkfz.de/Macromol/teaching/files/fcs_practical.pdf

[15] B.D. Cullity and S.R. Stock, Elements of X-Ray Diffraction, 3rd Ed., Prentice-Hall Inc., 167-171, 2001.

[16] Padmashri Patil, Shouvik Datta, Do we need to revisit the Bohr exciton radius of hot excitons? arXiv:1105.2205v4.

[17] P. Scherrer, "Bestimmung der Grösse und der inneren Struktur von Kolloidteilchen mittels Röntgenstrahlen," Nachr. Ges. Wiss. Göttingen, 26, 98-100, 1918.

[18] A. Patterson, The Scherrer Formula for X-Ray Particle Size Determination. Phys. Rev. 56 (10), 978–982, 1939.

[19] J. I. Langford and A. J. C. Wilson, "Scherrer after Sixty Years: A Survey and Some New Results in the Determination of Crystallite Size," J. Appl. Cryst. 11, 102-113, 1978.

[20] G. K. Williamson, W. H. Hall, X-ray line broadening from filed aluminium and wolfram**,** Acta Metallurgica, 1, 22-31. 1953.

[21] http://prism.mit.edu/xray

[22] Dynamic Light Scattering, chapter 7 written by B. CHU, Stony Brook University, Soft-Matter Characterization, Vol. 2, edited by Redouane Borsali, Robert Pecora, Springer.

[23] B. J. Berne and R. Pecora, Dynamic Light Scattering: With Applications to Chemistry, Biology, and Physics, Wiley.

[24] J. Goldstein, D. E. Newbury, D. C. Joy, C. E. Lyman, P. Echlin, E. LIfshin, L. Sawyer, and J. R. Michael. Scanning Electron Microscopy and X-ray Microanalysis (3 ed). Springer, 2003.

[25] P. J. Goodhew, and F. J. Humphreys, Electron Microscopy and Analysis, 2nd edition, Taylor and Francis, New York. A succinct summary of SEM, TEM, and AEM, 1988.

[26] http://priede.bf.lu.lv/ftp/pub/TIS/atteelu_analiize/ImageJ/apraksti/tutorials_and_examples.html

[27] J. Nelson, Physics of solar cell, Imperial college press,

[28] P. Wurfel, Physics of solar cell from basic principles to advanced concepts, Wiley-VCH, second edition.

[29] http://pveducation.org/pvcdrom/properties-of-sunlight/air-mass

[30] M. A. Green, Third Generation Photovoltaics, Advanced Solar Energy Conversion, Springer.

Chapter 3

Synthesis of Cadmium Telluride Quantum Dots and their Application in Sensitized Solar Cells

I. Introduction

Semiconductor materials are of prime importance in electronic as well as optoelectronic applications. Having energy bandgap between ~0.3 eV to ~3 eV make these materials whose properties can be tuned using accessible electronic and optical transitions. That makes these materials important for applications like transistors, diodes, light emitting displays, solar cells, etc. compared to metals and insulators. As we have seen in ***Chapter 1,*** spatial quantum confinement of charge carriers further helps to tune the range of possible electronic transitions (e.g. absorption/emission spectra) in these materials[1] via size effects. Many structural, optical and electrical properties of these materials also changes as a result of such spatial quantum confinement[2]. This in effect allows technology to create faster[3], compact[4], more efficient and affordable applications based on the size tunable physical properties. Basic physics and technology applications of such semiconductor nanocrystals or Quantum Dots (QDs) were extensively studied since from 1988[2].

Cadmium Telluride (CdTe) is a group II-VI semiconductor alloy having bulk band gap ~ 1.44 eV[5]. This is a favourable band gap for solar cell application because it nearly matches with the maximum of the solar spectrum which can further be used to optimize solar cell's power

conversion efficiency. Thus, it has been used as photo-absorber in solar cell since 1958[6,7]. Thin film solar cell using CdTe is considered as one of the alternative option over crystallite Silicon (Si)[8] because of its high photo-absorption coefficient and extinction coefficient. The highest power conversion efficiency achieved till 2013 using the second generation, vapour deposited CdTe thin film technology is ~19.6%[9]. Moreover, third generation solar cells promise even higher efficiency at reduced material cost using solution processed CdTe QDs. Therefore, extensive research is being done to use CdTe QDs as photo-absorber in nano-photovoltaic cells. The exciton Bohr radius of CdTe is ~65 Å which is highest compared to other II-VI materials from this group. Thus, in CdTe, one can practically play over a larger spatial size range for tuning the absorption and emission wavelengths. This material further demonstrate high photoluminescence (PL) quantum yields (QY)[10] which made it popular for use in optoelectronics including use in biological imaging and labelling application[11], light-emitting diodes (LEDs)[12,13,14], microarrays of multi-coloured light emitting pixels[15] and photosensitive films[16,17].

As we have seen in ***Chapter 1***, Quantum Dot Sensitized Solar Cell (QDSSC) represents third generation solar cells which not only promise practical advantages like ease in fabrication, cost effectiveness but also offer the technical possibilities of hot electron extraction and multiple carrier generation etc to enhance the effective power conversion efficiency. Therefore, it is considered more promising for future generation solar cells which can have the possibility to improve the performance much above dye sensitized solar cells (DSSC)[18,19,20,21,22,23]. There are different ways to sensitized/anchor these QDs on porous TiO_2 surface[24] in order to use them as sensitizer/ photo-absorber:

(1) In-situ growth of QDs by chemical bath deposition (CBD)[25],

(2) Deposition of pre-synthesized colloidal QDs by linker assisted adsorption[18,2121,26,27] &

(3) Use of Successive Ion Layer Adsorption and Reaction (SILAR) method[28,29,30,31].

Methods (1) and (3) follow in-situ growth for deposition of QDs using Cadmium and tellurium ions, but they usually lead to less than full coverage of TiO_2, due to uneven growth of QDs, which affects V_{OC} and thus the efficiency of solar cell[24]. Compared to that, use of pre-synthesized QDs with bi-functional molecule as capping layer are found to be better for tethering QDs on TiO_2 and so efficiency gets enhanced[32,33].

In chemical method of synthesis, two different strategies are used for production of semiconductor QDs with bi-functional molecules as capping layer like use of non-aqueous and aqueous solvents. The former strategy requires high temperature and so a high boiling solvent like trioctylphospine-oxide (TOPO) trioctophospine (TOP) which are commonly known as TOPO-TOP based synthesis routes. However, this particular strategy has many apparent drawbacks including toxicity of the above chemicals, requirement of more energy input due to temperatures. So this TOPO-TOP based synthesis route is not so environment friendly and also costlier. Moreover use of these QDs to make uniform thin films for any particular application is always considered as an issue due to their non-solubility in water. As such three different approaches have been used to get water soluble QDs:

a) Ligand exchange[34, 35, 36, 37,38],

b) Encapsulation into water soluble shell[39,40] and

c) Arrested precipitation in water[41,42].

But these approaches also include many processing steps and thus have additional disadvantage of being time-consuming, costly and complicated. The second strategy is aqueous, and as the name implies, it is non-toxic and due to lower boiling point of water, it requires less energy input thus making this a comparatively cheaper, highly reproducible, and water soluble QDs compatible for use in various applications. However, all solution processed QDs use bi-functional organic molecules which not only acts as capping ligands for QDs but they also allow for active control of the kinetics of synthesis and nucleation process. This is exploited in controlling the size, shape of these QDs. Further one uses these to passivate the surface dangling bonds[43,44] and also to make these soluble by careful choice of hydrophilic and hydrophobic geometry. Thiol based capping ligands also work as bi-linker molecules. They are good in capping QDs in aqueous medium and the terminal hydroxyl [–OH] group interacts and anchors with the carboxylic [–COOH] group from TiO_2 nanoparticles. This enhances the improved binding of QDs on electron harvesting TiO_2 layer and this type of interaction improves efficiency photo-generated charge transfer and thereby help in making better sensitized solar cells[32,33]. Aqueous synthesis of CdTe QDs have been reported earlier with different thiol based capping ligands like thioglycolic acid[45,46], 1-thioglycerol[46,47], mercaptoethylamine[4646], or L-cystein[4646], mercapto-propanoic acid[48,49] and mercapto-succinic acid[50].

In this chapter we will see how thiol based capping ligands like Mercapto-succinic acid (MSA) can be used for synthesis of good quality CdTe QDs, how to tether the resultant CdTe QDs on porous TiO_2 film for use in QDSSC and how the performance of resultant QDSSC depends on these procedures.

II. Materials and Methods for Synthesis

a. Chemicals Used

All chemicals are used as purchased without any further purification. Cadmium chloride, sodium borohydride, mercapto-succinic acid, Zinc Acetate ($Zn(OAC)_2$) and boric acid are purchased from Merck, sodium tellurite is purchased from LobaChemie, trisodium citrate is purchased from Thomas Baker. Terpineol, ethyl cellulose, rhodamine-6G is purchased from Sigma Aldrich, F:SnO2 (FTO) coated glass is purchased from Solaronix (7 Ω/square). TiO_2 (P25 Degussa was a generous gift from Evonik). Ethanol and methanol are HPLC grade. 18 MΩ/cm de-ionized (DI) water is used as solvent.

b. Synthesis Procedure

Wet chemical reaction is carried out in a three neck flask, first neck is used for water condensation (as the reaction proceeds at slightly higher temperature water condenser is usually used to condense water vapour), second one is used for monitoring temperature and third one is utilized to take out the aliquots. Mercaptosuccinic Acid (MSA) capped CdTe QDs are synthesized by modifying the procedure developed by E. Ying, et. al.[50]. All reactions proceeded in buffer solutions of boric acid and trisodium citrate. The requirement of buffer solution is to withstand the changes resulting from addition of sodium borohydride as given in the following reaction 3 and 4. Here 15 mM boric acid and 15 mM trisodium citrate is used in 50 ml DI water to make a buffer solution of pH 8. Precursor solution for CdTe QDs is made by adding cadmium chloride (1 mM), sodium telluriteNa_2TeO_3 (0.25 mM), and mercapto-succinic acid (3 mM) in 50 ml of buffer solution of pH 8 at 25 ^oC. After vigorous stirring of precursors for 5 min, 20 mg of sodium borohydride ($NaBH_4$) is added into the precursor solution. Reaction proceeds with formation of following products and bi-products.

$$4TeO_3^{2-} + 3BH_4^- \rightarrow 4Te^{2-} + 3B(OH)_3 + 3OH^- \quad \text{..... (1)}$$

$$CdL + Te^{2-} \rightarrow CdTe + L^{2-} \text{ where L= MSA} \quad \text{..... (2)}$$

$$BH_4^- + H_2O \rightarrow B(OH)_3 + OH^- + H_2 \quad \text{..... (3)}$$

$$BH_4^- + 2O_2 \rightarrow B(OH)_3 + OH^- \quad \text{..... (4)}$$

After reaction proceeds for 10 min at room temperature the flask is attached to a water condenser and refluxed at 80 ˚C under open air condition. Aliquots are collected at different time intervals after starting the reaction and labeled as #1, #2, #3….

c. TiO_2 Paste Preparation

0.75 g of P25 Degussa TiO_2 powder is taken in a clean and dry motor pestle. 0.13 ml of acetic acid is added into it with sustained grinding for 5 minutes to make uniform and complete spreading of acetic acid. After that 0.13 ml DI water is gradually added into it with continuous grinding. The procedure is repeated for five times. In order to avoid lump formation we have not added all the water at once. Then 0.32 ml of ethanol is added into it with continuous grinding. The addition and grinding is repeated for 5 minutes. Care has been taken not to leave anything dried and un-mixed. The mixture is then transferred in a round bottom flask using 15ml ethanol. The resultant solution is kept for 5 minutes under stirring and then 5 minutes under sonication. The sonication and stirring are repeated for at least 30 times. Then 2.5 gm of terpineol and solution of ethyl cellulose are added in it and again it is kept under stirring for 20 minutes. For making solution of ethyl cellulose 0.38 gm ethylene cellulose is added in 3.85 ml ethanol and sonicated till it mixed well. Now the resultant solution is stirred for 20 minutes. Finally, uniform slurry without any visible granules is formed. The extra solvent is then evaporated using rota-vapour. This TiO_2 paste is used for making porous thin film on FTO glass by doctor blade technique.

d. Cleaning of FTO Coated Glass and Deposition of Porous TiO_2 Film

Conducting transparent glasses coated with Fluorinated Tin Oxide (FTO) are purchased from Solaronix (7 Ω/square). Diamond cutter is used to cut the glass. Care has been taken not to scratch the conducting side. Pieces of FTO glass are then sonicated with water and ethanol each

for 15 minutes. After sonication, the glass pieces are heated at 450 ˚C for 5 minutes to remove any leftover organic molecules which made them ready for use as an electrode. TiO_2 is then deposited on conducting side by doctor blade technique on these cleaned and dried FTO glasses. After one deposition films are kept in oven preheated at 160 ˚C for 10 minutes. The deposition is repeated for 3 times with heating at 160 ˚C after each deposition. Finally the TiO_2 coated FTO glass is annealed at 450 ˚C for half an hour. The heating at high temperature confirms removal of organic molecules which are added for smooth formation of TiO_2 paste. This heating step also makes the film porous at nanoscale. Three such coating make ~10 micron thick TiO_2 layer. In order to remove pin holes and recover it from cracks the TiO_2 film is treated with aqueous $TiCl_4$ (0.04 M) and finally sintered at 450 ˚C for 30 mins.

III. Characterization of Quantum Dots

Figure 3.1 shows the X-Ray Diffraction spectrum from drop casted thin film samples of CdTe QDs. The representative X-Ray diffraction peak positions corresponding to bulk CdTe material is shown here for reference[51]. The XRD spectra of CdTe QDs corresponding to (111), (220) and (311) planes show zinc blend cubic crystalline structure[51] of CdTe.

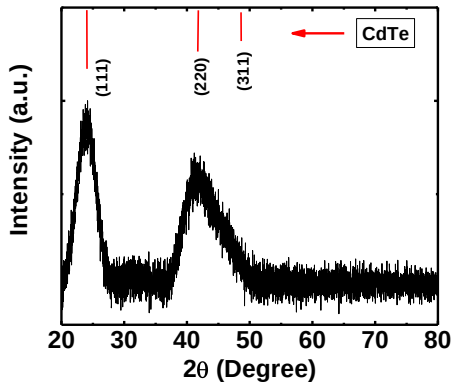

Figure 3.1. XRD spectrum of CdTe QDs. The characteristic peaks shows zinc blend crystal structure.

The absorption spectra for different aliquots of CdTe QDs collected at different refluxing time intervals are studied using UV-VIS absorption spectroscopy and it is given below as figure 3.2. Here, we have used samples with same concentrations (e.g. 20 μL of as prepared colloidal solution of QDs in 2 mL of D. I. water). Further growth of these aliquots can be restricted by

sudden cooling of these QDs. We have done this by keeping the solution containing vial in ice bath or in ice cold water. Growth of the QDs i.e. red shift in absorption is clearly visible with increase in reflux time. Form figure 3.2 it is clear that the fine control on size of QDs is gained by collecting aliquots at short intervals. The emission of photons from excited QDs is nothing but PL. The PL spectra for the same set of sample is also studied and given in figure 3.3.The image for CdTe QDs indicating their PL ability is given as figure 3.4.

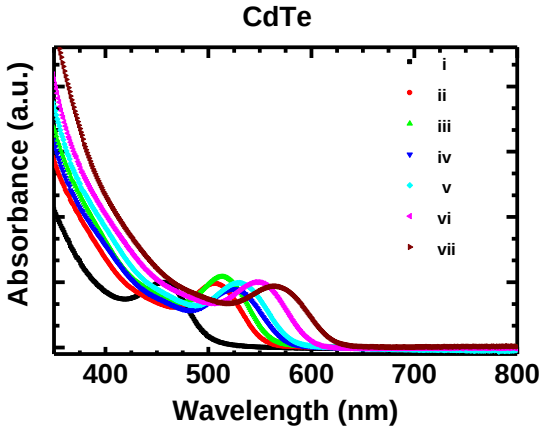

Figure 3.2. Absorption spectra for different size CdTe QDs.

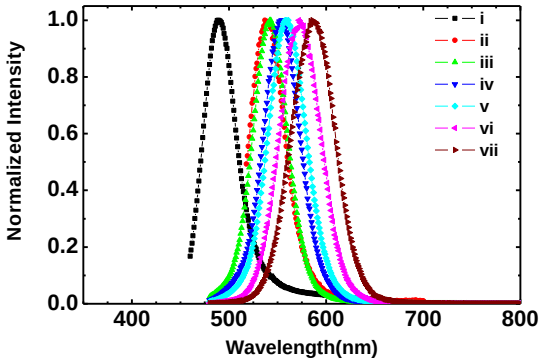

Figure 3.3. Photoluminescence spectra for consequently growing CdTe QDs. This proves that PL for QDs can be tuned easily by varying growth time.

Figure 3.4. Image of fluorescent colloidal CdTe QDs. A UV lamp is used to excite QDs.

PL QY for a sample measures the number of photons that come out with respect to the number of photons incident. PL QY is calculated for CdTe QDs by exciting the QDs sample and reference sample at 490nm and collecting PL spectrum. The resultant PL peak intensities are further used to calculate QY using following formula[52]

$$Q_s = Q_r \frac{A_s}{A_r} * \frac{OD_r}{OD_s} * \frac{n_s^2}{n_r^2}$$

Here, Q_s is QY of the sample, Q_r is PL QY of the reference material (Rhodamine 6g), We used fresh Rhodmine-6g solution in water as reference with a value of $Q_r = 95\%$[52]. A_s is area under the curve of photoluminescence spectrum for sample, A_r is area under the curve of PL spectrum for reference material, OD_r is optical density for reference, OD_s is optical density for sample (it is kept constant ~0.1 OD and the values are taken from respective recorded excitonic absorption spectrum), n_r and n_s are refractive indices of the solvent (water) for both reference and sample material. The measured PL QY is ~ 85% for sample this is highest compared to reported CdTe QDs with absorption maxima at 510 nm and it is observed that it decreases further with increase in size as shown in figure 3.5. The reason for high PL QY is reported[53] as more and more free thiols and cadmium ions would be released from the cadmium thiol complexes in the acidic range, so the surface coverage of the nanoparticles with MSA is increased when the CdTe solution becomes acidic. Therefore, more trap sites on the CdTe surface would be neutralized/removed, thus leading to higher PL efficiency.

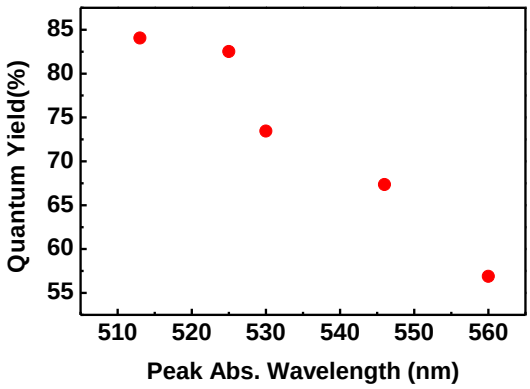

Figure 3.5. PLQY for MSA capped CdTe QDs.

Due to high PL QY we have used these QDs for Fluoresce Correlation Spectroscopy (FCS) in order to understand effect of blinking on hydrodynamic sizes of QDs. We have also tried to understand the charge transfer mechanism in blinking. The details of this study will be discussed in ***Chapter 7*** [54].

IV. Quantum Dot Sensitized Solar Cells Using CdTe QDs

a. Fabrication of Solar Cells

These CdTe QDs are used as sensitizer in QDSSC. QDs are deposited on TiO_2 coated FTO glass by pipetting solution of QDs on top of the TiO_2, where it stays for 1-2 hours[55]. Loading of the core/shell QDs can be checked from the apparent color change of the TiO_2. The resultant photoanode is then washed with ethanol and water. The ZnS layer is then coated on TiO_2 –QDs film by twice dipping the QDs loaded film in aqueous 0.1 M $Zn(OAc)_2$ and 0.1 M Na_2S solution for 1 min./dip. Once the ZnS coating is done photo-anode is made ready by washing the film with ethanol. The cell's assembly is done with QDs sensitized electrode with ZnS layer as photo-anode and Au as counter cathode using 50 miron thick scotch spacer with 10microlit polysulfide electrolyte. Nominal cell area is kept constant ~0.16 cm^2. The polysulfide electrolyte consisted of Na_2S (0.5 M), Sulfur powder (2 M) and KCl (0.2 M) in water and methanol (3/7 volume ratio)[56].

b. Characterization of QDSSCs

We have fabricated devices with typical area around 0.16 cm^2. When we have fabricated QDSSC using CdTe QDs we could not get satisfactory results at first, the efficiency is very low due to poor photocurrent i.e. short circuit current density (J_{SC} ~ 0.23 mA/cm^2) and open circuit voltage (V_{OC} ~ 0.24 V). This poor photo-response for a cell with CdTe QDs as sensitizer is understood from J -V characteristic as shown figure 3.6. Earlier reports revealed that utilization of CdTe QDs in photo-electrochemical cell for electric energy conversion has been limited[57,58,59,60]. It is observed that CdTe reacts with aqueous Na_2S present in electrolyte and this reaction creates a CdS layer outside CdTe QDs[60]. The valence band levels for CdTe, CdS and oxidation/reduction levels for electrolyte are such that electron transfers from electrolyte to CdS, but such transfers are not possible from CdS to CdTe[60]. This failure of scavenging holes from CdTe results in photo-degradation and further limits use of CdTe in SSC.

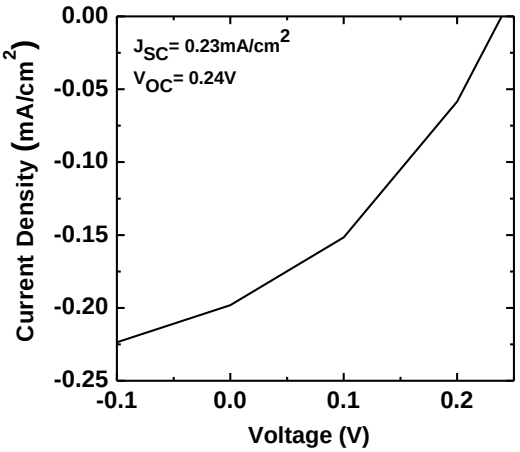

Figure 3.6. J-V characteristic for CdTe sensitized solar cell. The poor performance is due to reaction of CdTe with electrolyte.

V. Conclusions

Low temperature, aqueous based synthesis method for good quality CdTe QDs is developed in our lab. MSA capping is found good in order to get higher PL QY as well as tethering these QDs on porous TiO_2 layer. We have used these QDs in SSC as photo-absorber. However, the efficiency for cells is very low due to poor photocurrent. The poor efficiency is

mainly due to photo-degradation of CdTe in contact with electrolyte. This further creates inability for scavenging holes from CdTe and thus performance degrades under exposure of light. Due to excellent optical properties of the CdTe material as a photo-absorber we don't wanted to change the material. However, we tried to avoid the degradation and the inability of hole scavenging using type-II heterostructure nanoparticle. The synthesis method for such heterostructure and the improvement in cell performance will be discussed in next ***Chapter 4***.

VI. References

[1] http://www.columbia.edu/cu/chemistry/fac-bios/brus/group/pdf-files/semi_nano_website_2007.pdf Brus, L.E. (2007). "Chemistry and Physics of Semiconductor Nanocrystals."

[2] M. A. Reed, J. N. Randall, R. J. Aggarwal, R. J. Matyi, T. M. Moore and A. E. Wetsel, Observation of discrete electronic states in a zero-dimensional semiconductor nanostructure, Phys. Rev. Lett. 60 (6): 535–537, 1988.

[3] L. Greenemeier, (5 February 2008). "New Electronics Promise Wireless at Warp Speed". Scientific American.

[4] E. Prati, M. De, B. Marco, C. Matteo, F. M. Simonei, D. Kotekar-Patil, M. Ruoff, K. Dieter Few electron limit of n-type metal oxide semiconductor single electron transistors. Nanotechnology 23 (21): 215204, 2012.

[5] D. A. Jenny and R. H. Bube, Semiconducting CdTe, Phys. Rev. 96, 5, 1954.

[6] B. Goldstein, Properties of PV Films of CdTe, Phys. Rev 109 (2), 601, 1958.

[7] Y. A. Vodakov, G. A. Lomakina, G. P. Naumov and Y. P. Maslakovets, A P-N Junction photocell made of CdTe, Soviet Physics, Solid State 2 (1), 1, 1960.

[8] K. Zweibel, J. Mason, V. Fthenakis, A Solar Grand Plan, Scientific American, Jan 2008. CdTe PV is the cheapest example of PV technologies. and prices are about 16¢/kWh with US Southwest sunlight.

[9] M. A. Green, Y. Emery, W. W. Hishikawa, E. D. Dunlop, Solar Efficiency Tables (version 42). Progress in Photovoltaics: Research and Application 21: 827-837.

[10] S. F. Wuister, I. Swart, F.van Driel, S. G. Hickey and C. de Mello Donega, Highly luminescent water soluble CdTe quantum dots, Nanoletter, 3(4), 503-507, 2003.

[11] G. Entine, D. A. Garcia, D. E. Tow, Review of CdTe medical applications, Rev. Phys. Appl. 12, 355, 1977.

[12] N. P. Gaponik, D. V. Talapin, A. L. Rogach and A. Eychmuller, Electrochemical Synthesis of CdTe Nanocrystal/Polypyrrole Composites for Optoelectronic Applications, J. Mater. Chem., 10, 2163-2166, 2000.

[13] M. Gao, C. Lesser, S. Kirstein, H. Mohwald, A. L. Rogach and H. J. Weller, Electroluminscence of different colors from polycation/CdTe nanocrystal self-assembled films, J. Appl. Phys. 87, 2297-2302, 2000.

[14] C. Bertoni, D. Gallardo, S. Dunn, N. Gaponik and A. Eychmuller, Fabrication and characterization of red-emitting electroluminescent devices based on thiol-stabilized semiconductor nanocrystals, Appl. Phys. Lett. 90, 034107, 2007.

[15] M. Gao, J. Sun, E. Dulkeith, N. Gaponik, U. Lemmer and J. Feldmann, Lateral pattering of CdTe Nanocrystal films by electric field directed layer by layer assembly, Langmuir, 18, 4098-4102, 2002.

[16] D. V. Talapin, S. K. Poznyak, N. P. Gaponik, A. L. Rogach and A. Eychmuller, A. Synthesis of surface modified colloidal semiconductor nanocrystals and study of photo-induced charge separation and transport in nanocrystal-polymer composites, Physica E, 14, 237-241, 2002.

[17] D. M. Guldi, I. Zilbermann, G. Anderson, N. A. Kotov, N. Tagmatarchis and M. Prato, J. Mater. Chem., 15, 114, 2005.

[18] Gary Hodes, Comparison of dye- and semiconductor-sensitized porous nanocrystalline liquid junction solar cells, J. Phys. Chem. C,112, 17778–17787, 2008.

[19] A. Kongkanand, K. Tvrdy, K. Takechi, M. Kuno and P. V. Kamat, Quantum dot solar cells. Tuning photoresponse through size and shape control of CdSe-TiO2 architecture, J. Am. Chem. Soc. 130, 4007−4015, 2008.

[20] M. C. Beard, J. M. Luther, A. G. Midgett, O. E. Semonin, J. C. Johnson and A. J. Nozik, IEEE Phot. Spec. Conf., 000370−000375, 2010.

[21] I. Robel, M. Kuno and P. V. Kamat, Size-Dependent electron Injection from Excited CdSe Quantum Dots into TiO_2 Nanoparticles, J. Am. Chem. Soc., 129, 4136−4137, 2007.

[22] Y. Yang, W. Rodriguez-Cordoba, X. Xiang and T. Q. Lian, Multiple exciton generation and dissociation in PbS quantum dot-electron acceptor complexes, Nano Lett., 12, 303−309, 2012.

[23] A. J. Nozik, M. C. Beard, J. M. Luther, M. Law, R. J. Ellingson and J. C. Johnson, Semiconductor quantum dots and quantum dot arrays and applications of multiple exciton generation to third generation photovoltaic solar cell, Chem. Rev., 110, 6873−6890, 2010.

[24] Y. Keyou, C. Wei, and Y. Shihe, Significantly Enhanced Open Circuit Voltage and Fill Factor of Quantum Dot Sensitized Solar Cells by Linker Seeding Chemical Bath Deposition, J. Phys. Chem. C, 117, 92−99, 2013.

[25] L. J. Diguna, Q. Shen, J. Kobayashi and T. Toyoda, High efficiency of CdSe quantum- dot-sensitized TiO2 inverse opal solar cells, Appl. Phys. Lett., 91, 023116, 2007.

[26] I. Robel, V. Subramanian, M. Kuno, P. V. Kamat, Quantum Dot solar cells. Harvesting light energy with CdSe nanocrystals molecularly linked to mesoscopic TiO_2 films, J. Am. Chem. Soc.128, 2385−2393, 2006.

[27] I. Mora-Sero, S. Gimenez, T. Moehl, F. Fabregat-Santiago, T. Lana-Villareal, R. Gomez and J. Bisquert, Improving the performance of colloidal quantum-dot-sensitized solar cells, Nanotechnology, 19, 424007, 2008.

[28] Y. L. Lee and Y. S. Lo, Highly Efficient Quantum-Dot-Sensitized Solar Cell Based on Co-Sensitization of CdS/CdSe, Adv. Funct. Mater., 19, 604−609, 2009.

[29] H. Lee, H. C. Leventis, S. J. Moon, P. Chen, S. Ito, S. A. Haque, T. Torres, F. Nuesch, T. Geiger, S. M. Zakeeruddin, M. Gratzel and M. K. Nazeeruddin, PbS and CdS quantum dot-sensitized solid-state solar cells: "Old Concepts, New Results, Adv. Funct. Mater., 19, 2735−2742, 2009.

[30] R. Plass, S. Pelet, J. Krueger, M. Gratzel and U. J. Bach, Quantum Dot sensitization of organic-inorganic hybrid solar cells, Phys. Chem. B, 106, 7578−7580, 2002.

[31] H. Lee, M. K. Wang, P. Chen, D. R. Gamelin, S. R. Zakeeruddin, M. Gratzel and M. K. Nazeeruddin, Efficient CdSe quantum prepared by an improved successive ionic layer adsorption and reaction process, Nano Lett., 9, 4221−4227, 2009.

[32] J. R. Mann and D. F. Watson, Adsorption of CdSe Nanoparticles to Thiolated TiO_2 Surfaces: Influence of Intralayer Disulfide Formation on CdSe Surface Coverage, Langmuir, 23, 10924–10928, 2007.

[33] D. Pernik, K. Tvrdy, J. G. Radich and P. V. Kamat, Tracking the Adsorption and Electron Injection Rates of CdSe Quantum Dots on TiO_2: Linked Versus Direct Attachment, J. Phys. Chem. C, 115, 13511–13519, 2011.

[34] C. B. Murray, D. J. Norris and M. G. Bawendi, Synthesis and characterisation of nearly monodisperse CdE (E= sulphur, selenium, tellurium) semiconductor nanocrystallites, J. Am. Chem. Soc., 115, 8706-8715, 1993.

[35] D. V. Talapin, A. L. Rogach, A. Kornowski, M. Haase, H. Weller, Highly Luminescent Monodisperse CdSe and CdSe/ZnS Nanocrystals Synthesized in a Hexadecylamine – Trioctylphosphine Oxide – Trioctylphospine Mixture, Nano Lett., 1, 207-211, 2001.

[36] L. Qu, Z. A. Peng and X. Peng, Alternative Routes toward High Quality CdSe Nanocrystals Nano Lett., 1, 333-337, 2001.

[37] D. V. Talapin, A. L. Rogach, I. Mekis, S. Haubold, A. Kornowski, M. Haase and H. Welle, Synthesis and Surface Modification of Amino-Stabilized CdSe, CdTe and InP Nanocrystals, Colloids Surf. A, 202, 145-154, 2002.

[38] H. Mattoussi, J. M. Mauro, E. R. Goldman, G. P. Anderson, V. C. Sundar, F. V. Mikulec and M. G. Bawendi, Self-assembly of CdSe-ZnS quantum dots biaconjugates using an engineered recombinant protein, J. Am. Chem. Soc., 122, 12142-12150, 2000.

[39] D. Gerion, F. Pinaud, S. C. Williams, W. J. Parak, D. Zanchet, S. Weiss, and A. P. Alivisatos, Synthesis and properties of biocompatible water-soluble silica-coated CdSe/ZnS semiconductor quantum dots. J. Phys. Chem. B, 105, 8861-8871, 2001.

[40] B. Dubertret, P. Skourides, D. J. Norris, V. Noireaux, A. H. Brivanlou and A. Libchaber, In vivo imaging of quantum dots encapsulated in phospholipid micelles. Science, 298, 1759-1762, 2002.

[41] I. Sondi, O. Siiman, S. Koester and E. Matijevic, Preparation of aminodextran CdSnanoparticle complexes and biologically antibodyaminodextran –CdS nanoparticles conjugates, Langmuir, 16, 3107-3118, 2000.

[42] J. O. Winter, T. Y. Liu, B. A. Korgel and C. E. Schmidt, Recognition Molecule Directed Interfacing Between Semiconductor Quantum Dots and Nerve Cells, Adv. Mater., 13, 1673-1677, 2001.

[43] Kiran P. Kadlag, Padmashri Patil, M. Jagadeeswara Rao, Shouvik Datta, Angshuman Nag, Luminescence and Solar Cell from Ligand-Free Colloidal $AgInS_2$ Nanocrystals, Cryst. Eng. Comm, 16, 3605-3612, 2014.

[44] A. L. Rogach, T. F., T. A. Klar, J. F., N. Gaponik, V. Lesnyak, A. Shavel, A. Eychmuller, Y. P. Rakovich, and J. F. Donegan, Aqueous Synthesis of Thiol-Capped CdTe Nanocrystals: State-of-the-Art, J. Phys. Chem. C, 111, 14628-14637, 2007.

[45] M. Gao, S. Kirstein, H. Mohwald, A. L. Rogach, A. Kornowski, A. Eychmuller and H. Weller, Electroluminescence of Different Colors from Polycation/CdTe Nanocrystal Self-Assembled Films, J. Phys. Chem. B, 102, 8360, 1998.

[46] N. Gaponik, D. V. Talapin, A. L. Rogach, K. Hoppe, E. V. Shevchenko, A. Kornowski, A. Eychmuller and H. Weller, Thiol-capping of CdTe nanocrystals: an alternative to organometallic synthetic routes, J. Phys. Chem. B, 106, 7177, 2002.

[47] A. L. Rogach, L. Katsikas, A. Kornowski, D. Su, A. Eychmuller, H. Weller and H. Ber. Bunsen-Ges. Synthesis and Characterization of Thiol-Stabilized CdTe Nanocrystals, Phys. Chem. 100, 1772, 1996.

[48] H. Zhang, Z. Zhou, B. Yang and M. J. Gao, Vesicles with superior stability at high temperature, Phys. Chem. B, 107, 8, 2003.

[49] L. Li, H. F. Qian, N. H. Fang and J. C. Ren, Significant enhancement of the quantum yield of cdte nanocrystals synthesized in aqueous phase by controlling the pH and concentrations of precursor solutions. Lumin., 116, 59–66, 2006.

[50] E. Ying, D. Li, S. Guo, S. Dong and J. Wang, Synthesis and Bio-Imaging Application of Highly Luminescent Mercaptosuccinic Acid-Coated CdTe Nanocrystals. PLoS ONE 3(5): e2222. doi:10.1371/journal.pone.0002222, 2008.

[51] R. J. Bandaranayake, G. W. Wen, J. Y. Lin, H. X. Jiang, and C. M. Sorensen, Structural phase behavior in II–VI semiconductor nanoparticles, Appl. Phys. Lett. 67, 831, 1995.

[52] J. R. Lakowicz, Principles of Fluorescence Spectroscopy, 2nd Ed., Kluwer Academic, New York, 1999.

[53] M. Gao, S. Kirstein, H. Mohwald, A. L. Rogach and A. Kornowski, Strongly photoluminescent CdTe nnanocrystals by proper surface modification. J. Phys. Chem. B, 102, 8360–8363, 1998.

[54] A.V.R. Murthy, Padmashri Patil, Shouvik Datta, Shivprasad Patil, Photoinduced dark fraction due to blinking and photodarkening probability in aqueous CdTe quantum dots. J. Phys. Chem. C. 117, 13268-75, 2013.

[55] Z. Pan, H. Zhang, K. Cheng, Y. Hou, J. Hua, and X. Zhong, Highly efficient inverted type-I CdS/CdSe core/shell structure QD-sensitized solar cells, ACS Nano, 6, 3982, 2012.

[56] Y.-L. Lee and C.-H. Chang, Efficient polysulfide electrolyte for CdS ... solar cells, J. Power Sources, 185, 584, 2008.

[57] S. M. McGregor, I. M. Dharmadasa, I. Wadsworth and C. M. Care, Growth of CdS and CdTe by Electrochemical Technique for Utilization in Thin Film Solar Cells. Opt. Mater. 6, 75–82, 1996.

[58] A. Kampmann and D. Lincot, Photoelectrochemical Study of Thin Film Semiconductor Heterostructures: Junction Formation Processes in CdS/CdTe Solar Cells. J. Electroanal Chem. 418, 73–81, 1996.

[59] Mathew, X.; Bansal, A.; Turner, J. A.; Dhere, R.; Mathews, N. R.; Sebastian, P. J. Photoelectrochemical Characterization of Surface Modified CdTe for Hydrogen Production. J. New Mater. Electrochem. Syst. 5, 149–154, 2002.

[60] J. H. Bang and P. V. Kamat, Quantum Dot Sensitized Solar Cells. A Tale of Two Semiconductor Nanocrystals: CdSe and CdTe, ACS NANO, 3 (6), 1467–1476, 2009.

Chapter 4

Aqueous Synthesis of CdTe/CdSe Core/Shell Quantum Dots and their Application in Sensitized Solar Cell

I. Introduction

Currently world is facing a huge energy crisis and demand will continue to increase by many folds in the near future. We have also seen that dependence on non-renewable energy sources cannot give us a permanent solution as these sources are exhaustible and often produce non-repairable damage to earth's environment. So a more promising way to satisfy such huge energy demands without creating pollution is use of renewable energy sources like sunlight through solar cells. Great efforts have been made to make affordable solar cells so that power can be generated at a cost lower than the cost of traditional electricity generation. A third generation solar cell is considered very promising for increasing efficiency and making the production processes affordable. Though the measured efficiency for these devices is low compare to the first generation solar cells it can be used for niche applications such as charging battery in the mobile phones, running small toys and watches etc. As these devices has less operational lifetime and doesn't require high power conversion efficiency, solar cells with somewhat reasonable efficiency of even 5-10% made at a lower manufacturing cost can be used to reduce overall cost of these applications. Sensitized solar cells (SSC) are a class of third

generation cells which cost ~1/3rd to 1/5th of the other semiconductor solar cells based crystalline materials and or vapor deposited thin films. The comparatively lesser cost is mainly due to lower material utilization rate in third generation solar cells. A lot of research is being done in this field since the first sensitized solar cell report is published[1]. The importance of QDs in this regard is also discussed in ***Chapter 3***. There we have seen the method to synthesize CdTe QDs in aqueous medium at low temperature. The problem of self-destruction of CdTe QDs in contact with electrolyte and as a result, a non-efficient sensitized solar cell is also discussed in ***Chapter 3.*** According to literature, use of doped QDs[2,3], co-sensitization[4,5,6] and core/shell heterostructure QDs[7,8,9,10] enables better power conversion efficiency compared to use of single QDs. This may be due to limitation of absorption range of single QDs as well as stability issues related to particular QDs[11,12,13,14,15].

Core/shell (CS) heterostructure QDs of II-VI semiconductors have found a wide range of applications in optoelectronics[16,17], bio-imaging[18] and photovoltaics[19,20,21] etc. CdTe/CdSe is one such type-II heterostructure CS material. In type-II heterostructures, the core and shell are made up of two different semiconducting materials with a particular valence and conduction band alignment at the hetero-interface as shown in figure 4.1a Figure 4.1b shows schematic for core/shell hetrostructure which clearly differentiates the core, shell and capping layer material.

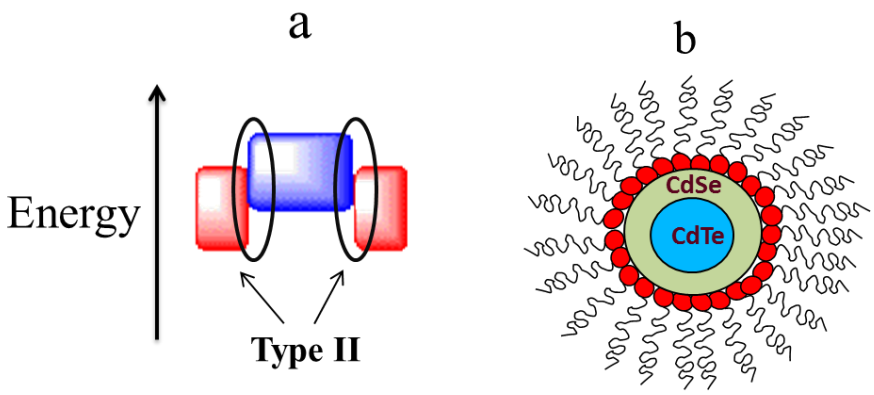

Figure 4.1. Schematic describing a) band alignment in type-II heterostructure and b) core, shell and capping layer (micelles like structure after CdSe) together forming core/shell heterostructure.

The band alignment of these semiconductor QDs is such that it efficiently assists the all important charge separation of photo-excited electron hole pairs[22,23,24]. This charge separation

process effectively slows down the radiative recombination rates of photo-generated carriers, which allows better harvest of photo-generated electron-hole pairs in photovoltaic cells[19,25] and also in photoconductive devices[19]. Therefore, lot of attention has been focused on the synthesis[25,26,27,28] of these core/shell QDs as well as on their use in nano-photovoltaics.

There are many reports on synthesis of different type-II hetero-structures like CdSe/ZnTe[29,30,31], CdTe/CdSe[27,32,33,34,35], CdTe/CdSe alloys[36], CdSe/CdS[26,37,38,39] etc. using a variety of complex wet chemical methods involving elaborate purification techniques. There are also reports[18,2827,28] which explain the mechanism of charge transfer in CS QDs as a function of shell thickness but most of these have been synthesized using hazardous chemicals and at high temperatures of >250 ˚C but to the best of our knowledge, there is only one report[8] using these QDs for solar cells (η ~ 2.4%). Moreover, the effect of varying shell thickness on solar cell performance is not well studied.

In this chapter we report the investigations of a simple aqueous synthesis of CdTe/CdSe based CS heterostructure QDs grown without any seed purification at considerably lower temperature of 80 ˚C. These materials reveal good structural, optical quality as well as comparatively similar power conversion efficiency of ~2% for such material system. A quicker and procedurally simpler chemical synthesis route is always economically desirable for large scale production of these heterostructure QDs. The low temperature aqueous synthesis technique without seed purification presented here provides one such simple and economic processing method to grow good quality of CdTe/CdSe core shell QDs for mass production. We have also demonstrated that the solar cell parameters of these sensitized cells are strong functions of the shell thickness as expected for such charge separating type-II heterostructures. The schematic diagram showing CdTe/CdSe adsorbed on TiO_2 along with ZnS layer and charge transfer process between them is given as figure 4.2. The assembly of QDs on TiO_2 is another important factor which affects the performance of SSC. The MSA capping ligand here works as a bi-linker molecule whose one end is connected to QDs and other end helps in tethering QDs on TiO_2.

In general these bi-linker molecules are insulating in nature. So their presence in between QDs and TiO_2 degrade the charge transport and hence affect the short circuit current density (J_{SC}). The sintering of photoanode is known for removal of such bi-linker molecules[10,33,40,41,42]. The effect of sintering sensitized photoanode at different temperature for improvement of J_{SC} is also presented in this chapter.

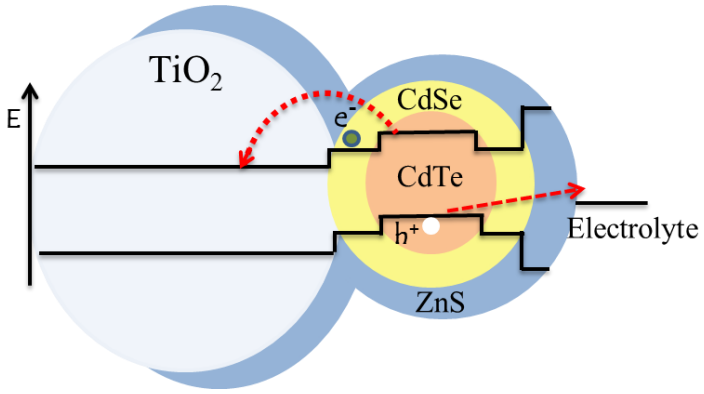

Figure 4.2. Schematic diagram describing the charge separation and charge transfer processes in CdTe/CdSe based sensitized solar cell. The system consists of CdTe/CdSe CS QDs adsorbed on TiO_2 electrode and then coated with a thin ZnS layer. Here, electron hole pair is photo generated in CdTe and these electrons are transferred to TiO_2 via CdSe and are then collected at FTO contact. The electron from electrolyte probably tunnels to neutralize the vacancy to complete the photo electrochemical cycle.

II. Experimental Methods

a. Chemicals Used For Synthesis

All chemicals utilized in this study are used as purchased without any further purification or treatments. Cadmium chloride, sodium borohydride, mercapto-succinic acid and boric acid, acetic acid, sodium sulfide, sulfur powder, titanium tetrachloride, and potassium chloride are purchased from Merck. Sodium tellurite and sodium selenite are purchased from Loba Chemie. Trisodium citrate is purchased from Thomas Baker. Terpineol, ethyl cellulose, rhodamine-6g are purchased from Sigma Aldrich F:SnO_2 (FTO) coated glass is purchased from Solaronix (8 ohm/square). Degussa P-25 TiO_2 nanoparticles are a generous gift from Evonik. Ethanol and methanol are HPLC grade. De-ionized (D. I.) water with 18 MΩ-cm is used.

b. Synthesis of CdTe Core QDs (i.e. Seed Solution)

CdTe QDs are synthesized using the procedure developed in our lab[43] and as discussed in ***Chapter 3***. Reaction is carried out in a three neck flask, where first neck is used for water condensation; second one for monitoring temperature and third one take out aliquots. Reactions

proceeded in buffer solutions of boric acid and trisodium citrate, where 15 mM of boric acid and 15 mM of trisodium citrate are used in 50 ml de-ionized water to make a buffer solution of pH-8. Precursor solution for CdTe QDs are made with cadmium chloride (1 mM), sodium tellurite Na_2TeO_3 (0.25 mM), and mercapto-succinic acid (MSA) (3 mM) in 50 ml of buffer solution of pH-8 at 25 ˚C. After vigorous stirring (~900 rpm) of precursors for 5 minutes, 20 mg of sodium borohydride ($NaBH_4$) is added into the solution. This reaction is carried out for 10 minutes inside the flask. After that flask is attached to the condenser and then heated along with stirring at 80˚C under ambient condition. Aliquots are collected at different time intervals after starting the reaction and are characterized further. We used these CdTe QDs as seeds with and without purification for further synthesis of CdTe/CdSe CS QDs heterostructure. Structural and optical properties for CS QDs with and without purification are studied and discussed below in detail.

c. Synthesis of CdTe/CdSe core/shell heterostructure QDs

c. 1. With Purification of Seed Solution

Traditional CS synthesis processes consist of rigorous purification of CdTe seed QDs[25,44]. In this method, we stop the reaction after attaining certain peak wavelength of excitonic absorbance of these CdTe QDs (here in this case absorbance peak ~507 nm). We have purified CdTe QDs which involves precipitation of QDs with ethanol and washing four times using a centrifuge (~6000-7000 rpm). We assume that there is not much loss of CdTe QDs while washing. These purified CdTe QDs are subsequently dispersed into 43 ml of buffer solution of pH 8 and subsequently heated to 80 ˚C along with stirring of ~900 rpm. To make top CdSe shell layer on CdTe core, we have mixed 0.001 M sodium selenite precursor and 0.02 g of $NaBH_4$ in 7 ml deionized water and at last we have added it to the hot purified solution of seed CdTe QDs. Finally after 10 minutes into the reaction, we have enriched the solution with Cd^{2+} ions by adding 0.5 mM $CdCl_2$ and 1.5 mM MSA. Four such aliquots are collected at different time intervals which then used for further characterization and compared with CS QDs synthesized without purification of seeds. These samples are labeled as CdTe, CS1, CS2, CS3 and CS4 (Core QDs used as seeds are labeled as CdTe). Note that CS QDs has nearly same absorption maximum wavelength to that of CS QDs synthesized without purification of seeds.

However, we have not labeled these CS QDs by their absorption maximum just to avoid confusion.

c. 2. Synthesis of CdTe/CdSe CS QDs Without Purification of Seed Solution

In this procedure we have not purified the seed CdTe QDs. Here we allow CdTe QDs to increase until the QDs absorbance matched with desired wavelength; the size of the QD is correlated to the absorbance of QDs. Once we get the desired absorbance wavelength, we have added 1 mM sodium selenite precursor in as prepared seed CdTe QDs solution at 80 ˚C. Thereafter, we have enriched this solution with Cd^{2+} ions by adding 0.5 mM cadmium chloride. CdSe is then allowed to grow on the CdTe QDs with heating at 80 ˚C and continuous stirring of ~900 rpm. Aliquots are collected at different time intervals from the three neck flask and used for further characterization. Four representative CdTe/CdSe core/shell QDs are selected and its optical as well as structural properties are studied and compared with that of CS QDs synthesized after purification of core QDs. The QDs are labeled with its absorption maximum wavelength as QD_{534}, QD_{568}, QD_{592} and QD_{606}. The same set of CS QDs is used as sensitizer for the fabrication of sensitized solar cell.

d. Fabrication of Sensitized Solar Cells

The FTO coated glass electrodes are cleaned as discussed in ***Chapter 3 section II-D,*** using diluted soap solution, water and ethanol and finally heated at 450 ˚C for 10 mins in order to remove contaminants. P25 TiO_2, acetic acid, terpineol, ethyl cellulose, water and ethanol are used to prepare TiO_2 paste; detailed procedure is given in ***Chapter 3 section II-C*** (The exact procedure followed for preparation is also given here[45]).

Even though QDs are of high quality and stable for long time, it is still a great challenge to assemble uniform layer of previously synthesized QDs on mesoporous TiO_2 with high area coverage. In order to improve the material loading and surface covering we have used freshly prepared MSA capped aqueous QDs. The as prepared QDs suspension (with absorbance '2' at first excitonic absorption peak) was pipetted directly on TiO_2 electrode where it is allowed to stay for two hours[10,36]. QDs loaded TiO_2 are then washed using ethanol and water. The loading of core/shell QDs can be checked from the coloring of TiO_2. The ZnS layer is then coated on TiO_2–QDs film by twice dipping the QDs loaded film in aqueous 0.1 M $Zn(OAc)_2$ and 0.1 M

Na_2S solution for 1 min./dip. Once the ZnS coating is done, photo-anode is made ready by washing the film with ethanol and sintering it at ~200 ˚C, ~400 ˚C in ambient for 5 mins.

Finally, the cells are prepared by assembling QDs sensitized electrode with ZnS layer as photo-anode and Au as counter cathode using 50 μm thick scotch spacer with 10 microlit polysulfide electrolyte. The polysulfide electrolyte consists of Na_2S (0.5 M), Sulfur powder (2 M) and KCl (0.2 M) in water and methanol (3/7 volume ratio)[46]. Several such cells are made and one with best efficiency is chosen as final data. Nominal cell area is kept constant ~0.16 cm^2.

III. Results and Discussions

a. Structural and Optical Properties

In this section we will discuss both structural and optical qualities of these CS heterostructure QDs using X-ray diffraction (XRD) spectroscopy, optical absorption spectroscopy, steady state photoluminescence spectroscopy and finally by TCSPC. Some of these optical spectroscopy results for CdTe/CdSe CS QDs are described in Table #4.1. Figure 4.3 shows the evolution of XRD spectra for core/shell QDs synthesized without purification of seeds.

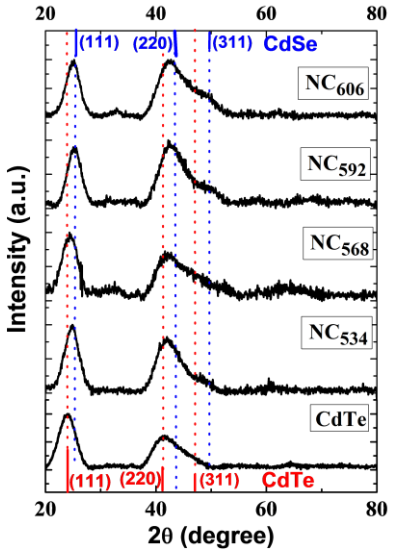

Figure 4.3. Evolution of core/shell crystal structure for CdTe/CdSe synthesized using unpurified core QDs is shown using XRD pattern. The planes for CdTe and CdSe are given for reference.

Here the CdTe QDs are the core QDs used as seeds for forming core/shell structure and rest of the samples are CS structures after consecutive growth of shell layer. The representative X-Ray diffraction peak positions corresponding to bulk CdTe and bulk CdSe materials are shown at the bottom and top of the figure for reference[47]. The XRD spectra of CdTe QDs shows peaks with d-values that corresponding to (111), (220) and (311) planes of the cubic phase of CdTe[47] (a_{CdTe}= 0.648 nm[44]). We noticed that XRD peaks shift to higher angles as compared to that of only CdTe QDs as soon as CdSe shell forms on these CdTe seeds and finally matches with the generic CdSe peaks. The (311) peaks start appearing at 51˚ after shell growth which is not visible in only CdTe. Moreover, we identify these dominant XRD peaks of CS QDs mostly with (111), (220), (311) planes of cubic crystallites of CdSe[47] (a_{CdSe} = 0.605 nm) thus confirming the formation of top shell layer. This reaffirms the formation of CdSe shell layer on top of CdTe core. Moreover, nearly similar spectral features of XRD are observed for CS QDs synthesized with purified seed QDs as given in figure 4.4. From figure 4.3 and figure 4.4 it is clear that similar shift occur in the planes features corresponding to (111) and (220) to higher angles instead of showing two independent peaks. This supports our argument that it cannot be a mixture of two differently grown QDs[33]. This gradual shifting of peak to higher angle also indicates presence of strain at the interface due to lattice mismatch of CdTe and CdSe QDs[44].

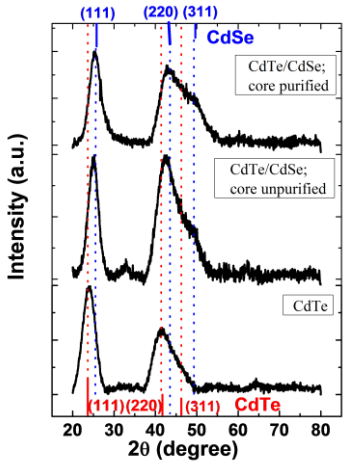

Figure 4.4. XRD spectra for CdTe and CdTe/CdSe CS NCs synthesized using unpurified and purified seed NCs.

The morphology of seed CdTe and QD_{606} CS QDs synthesized using unpurified core is studied using HR-TEM and images are given as figure 4.5 and 4.6 respectively. The image clearly shows that CdTe QDs are nearly spherical. Magnified HRTEM image of representative QD sample is given as left inset for both of the samples.

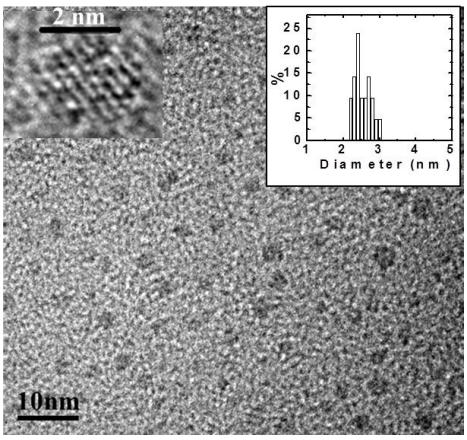

Figure 4.5. Structural characterization for MSA capped CdTe QDs using HRTEM. The measured median diameter of CdTe QDs is ~2.3 nm.

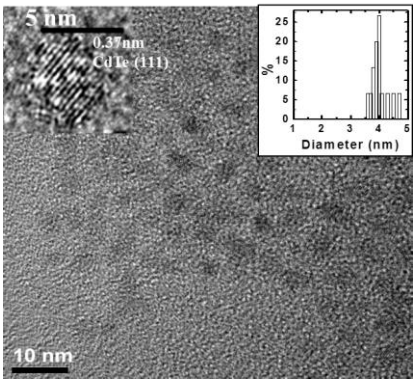

Figure 4.6. HRTEM image for thickest shell CdTe/CdSe CS QDs synthesized using unpurified core QDs i.e. QD_{606} sample. By scrutinizing high-resolution TEM, the lattice fringe of CdTe (111) is clearly reflected.

Diameters of QDs are first analyzed using 'ImageJ' software. This procedure is repeated and values are averaged to minimize the error. The average QDs diameter is assessed via this statistical analysis of measured HRTEM images of these QDs. The final histogram of percentage of such QDs having a particular size range is shown as right inset for both the samples in figure 4.5 and 4.6. The median diameter of CdTe QDs is estimated from the HRTEM image and it is

found to be ~2.3 nm. Similarly, the HRTEM image CdTe/CdSe core–shell structures also shows nearly spherical shape. The median particle size (~ 4 nm from the HRTEM images) is found to be higher than that of CdTe seed QDs. By scrutinizing high-resolution TEM, the lattice fringe of CdTe (111) is clearly reflected as shown in left inset of figure 4.6. From both HRTEM images, it can be concluded that the QD diameter increases by about 2 nm upon shell growth. Interestingly, the smallest such CS QDs diameter for QD_{606} is ~3.6 nm. We could not find any CS QDs smaller than this minimum size from the statistical analysis of about fifty CS QDs scanned during the imaging process. This actually means CdSe is growing as shell layer on CdTe seed QDs and not growing separately as independent crystals.

The evolution of optical absorption spectra of CdTe/CdSe CS QDs synthesized without purification of seed QDs is shown in figure 4.7. Here aliquots are taken at different time intervals during the growth of shell layer. The absorption spectra for CdTe/CdSe CS QDs synthesized using purified seed is also given for comparison as figure 4.8. Here in both figure 4.7 and figure 4.8 the spectrum with lowest absorption wavelength is the spectrum for core QDs which is used as seed QDs. Rest of the samples has CdSe shell layers growing on top of respective CdTe seeds.

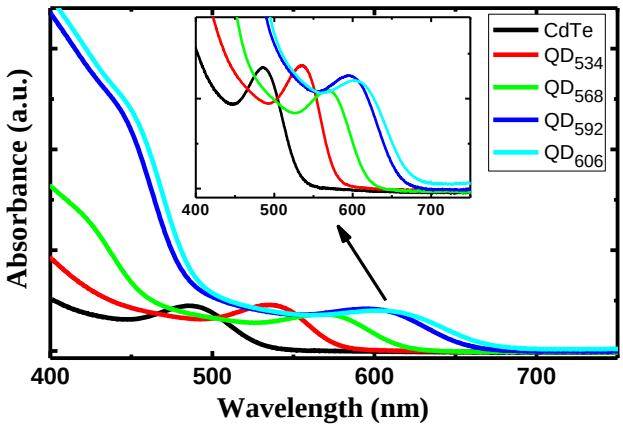

Figure 4.7. Absorption spectra for CdTe/CdSe CS QDs synthesized without purifying CdTe seed particles. Magnified spectra are given as insets for better insight of the red shifts of the excitonic absorption peaks.

A preliminary growth of the CdSe shell layer actually red shifts the absorption peak in both cases. This behavior continues and further growth of CdSe shell layer gradually shifts these excitonic peaks to higher and higher wavelength. Moreover, there is a growing presence of a

shoulder like feature as shown in figure 4.7 and 4.8 which is totally absent in MSA capped CdTe seed QDs (Please refer ***Chapter 3*** figure 3.3). Additionally, we also observe that the shoulder like absorption edge becomes prominent in thickest CdSe shell layer samples. So this shoulder like second absorption feature can certainly be assigned to the direct optical absorption in the CdSe shell layer only[48] . However, this red shift of excitonic peak and CdSe shoulder are present in both CS QDs synthesized using both purified and unpurified seeds.

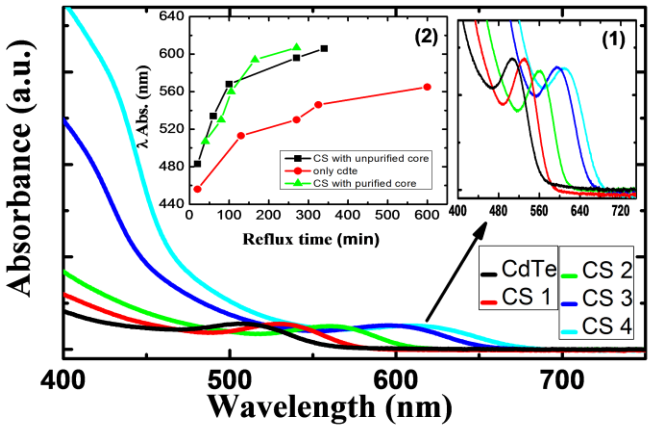

Figure 4.8. Absorption spectra for CdTe/CdSe CS QDs synthesized after purification of seed QDs. Inset 1 is given for better insight of the red shifts of the excitonic absorption peaks and inset 2 shows change in wavelength of excitonic peak of QDs with refluxing time.

The evolution of optical spectra for only CdTe is also studied for comparison (***Chapter 3,*** figure 3.3). Interestingly, while experimenting, we observed that the CdTe growth (red shift in absorption spectra) takes ~ 9 hours for getting absorption peak shifts from 456 nm to 565 nm in contrast to that CS QDs synthesized by both ways takes only one and half hour time for getting nearly same shift (for core/shell QDs the refluxing time is counted after addition of sodium borohydride in the aqueous solution of reagents as mentioned in synthesis section. In case of CdTe/CdSe CS QDs synthesized by using purified seeds the reflux time is calculated without considering the purification interval). The plot for reflux time and the absorption red shift is given as inset (2) of figure 4.8. Here, in case of CdTe, the significant red shift of optical absorption spectra is due to slow increase in size of QDs with time as a result of Ostwald's ripening effect. It is easy to understand that with increasing heating time, size of the CdTe QDs increases which subsequently decreases its band gap due to the relaxation of size confinement of

charge carriers and thereby causing the redshift. Similarly one can also understand red shift of the shoulder like feature (figure 4.7 and 4.8) representing the CdSe band edge with increasing CdSe shell thickness as time passes. However, the reason for getting such relatively quicker red shift with increasing refluxing time during formation of CdSe shell is not very well understood although it is well known that reaction towards the formation of both only CdTe and only CdSe proceed with similar rate. Moreover, not much difference in the optical absorption spectra is observed for CdTe/CdSe CS QDs synthesized using purified and unpurified seeds. This also reasserts why the redshift in unpurified CS QDs cannot come from any further growth of only CdTe material, as qualitatively similar red shift is also observed in CS QDs synthesized using purified seeds i.e. even in absence of any tellurium reagents and other byproducts from the CdTe seed synthesis. This sizable difference between growths of only CdTe seed QDs with respect to those CS QDs may explain the striking similarity in physical properties of CdTe/CdSe CS QDs grown with and without purification. It is possible that the amount of Te^{2-} precursor is already depleted while forming seed CdTe QDs for nearly one hour of heating and not oxidized. Therefore, any further quicker growth of these unpurified CdTe seeds can be governed mainly by the presence of additional Se^{2-} (as Se^{2-} are available in excess quantity as compared to that of depleted Te^{2-}) in the reactant solution.

The PL spectra of these CdTe/CdSe CS QDs synthesized by both methods are studied and given as figure 4.9 and 4.10.

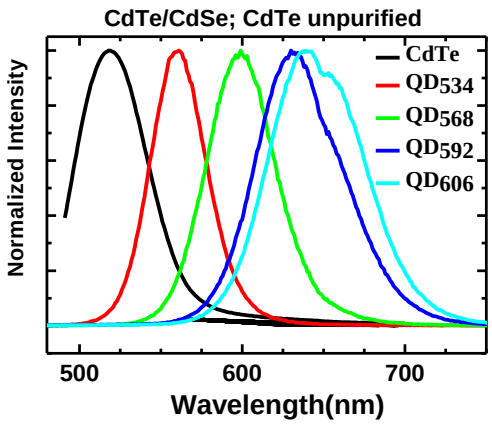

Figure 4.9. PL spectra for CdTe/CdSe CS QDs synthesized without purification of seeds.

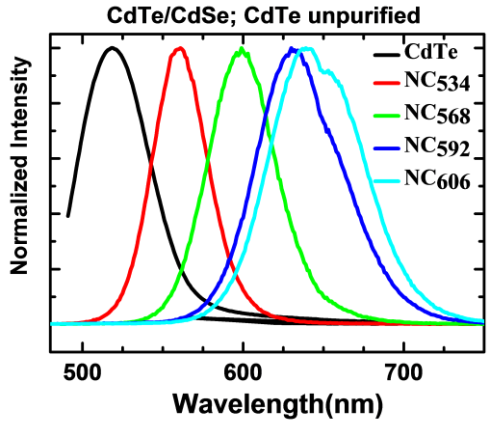

Figure 4.10. PL spectra for CdTe/CdSe QDs synthesized after purification of seeds.

The ability of these QDs to cover long range wavelength is clearly visible from these spectra. The quantitative similarities between the red shift of both ways synthesized QDs importantly emphasizes the similarity in optical properties of these methods.

PL Quantum Yield (QY) is calculated for these CS QDs synthesized by using both methods. For calculating PL quantum yield (QY) all samples are excited at 520nm. The resultant PL peak intensities are further used to calculate QY for CdTe/CdSe CS QDs synthesized by both procedures using the formula given in ***Chapter 2, section II***. Figure 4.11 shows QY plots for CdTe/CdSe CS QDs synthesized by both procedures.

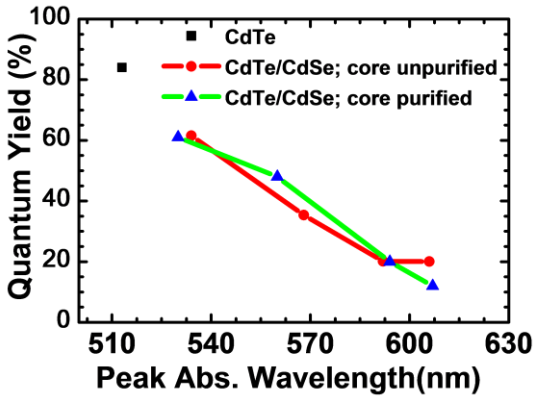

Figure 4.11. PL QY for CdTe seed QDs and CdTe/CdSe CS QDs synthesized by both procedures are plotted with respect to wavelength of excitonic absorption.

We want to emphasize that these estimates of PL QY (maximum QY ~60%) of CdTe/CdSe CS QDs are as good as or even better than any such CS QDs made by using aqueous

routes[27].The wavelength on X axis corresponds to peak excitonic absorption wavelength for CS QDs (from figure 4.7 and figure 4.8). We observe that the maximum quantum yield of CdTe/CdSe CS QDs is ~60% for QD_{534} and also for CS2, for thickest shell QDs in both varieties of CS QDs it further decreases to ~15%. This is possibly explained by the expected type-II band alignment at CdTe/CdSe core-shell hetero-interface. The main reason for observed decrease in PL QY with thicker shells might be that after photo-absorption one of the charge carriers (say hole) is confined to core and other (say electron) is transferred to shell. So probability for these delocalized charge carriers (either electrons or holes) to be trapped by non-radiative surface states at the CS heterostructure interface is high. This can certainly lead to non-radiative re-combinations[49] which ultimately reduces the PL QY of these type-II band gap heterostructures. Large lattice mismatch (~7%) and strain between core (CdTe) and shell (CdSe) layers can create such non-radiative channels at the heterojunction interface of CS and thereby reduce PL efficiency of core-shell materials[26,44]. Most interestingly this variation of PL QY is almost similar in CdTe/CdSe CS QDs prepared by both procedures. This again emphasizes that both varieties of CS QDs are qualitatively similar with respect to optical absorption, type-II charge separation and final PL QY.

In order to understand reasons for decrease in PL QY with increasing CdSe shell thickness, we have studied PL lifetime of photoluminescence using TCSPC for CdTe/CdSe CS QDs synthesized by both procedures as well as for CdTe seed QDs. The result for CS QDs synthesized using unpurified core QDs is shown in figure 4.12. Photoluminescence decays are measured using time correlated single photon counting (TCSPC) setup from Horiba Jobin Yvon IBH, USA. As a pulse excitation source we have used 405 nm photo-excitation source from IBH, UK (NanoLED-405L). The photoluminescence decay for CS QDs is tail-fitted using a double-exponential decay function given by equation 4.1,

$$I(t) = a_1 \exp(-t/\tau_1) + a_2 \exp(-t/\tau_2) \qquad (4.1)$$

Plots are fitted such that reduced chi-squared parameter (χ^2) approaching 1 and resulting small residual. Here, τ_1 and τ_2 are the photoluminescence decay constants obtained from above data analysis and a_1 and a_2 are the corresponding pre-exponential factors. The average lifetime τ_{avg} is calculated as an intensity-weighted sum of the two lifetime components. The obtained values of

τ_1, τ_2 and calculated average lifetime τ_{avg} for CS QDs synthesized with unpurified core QDs are given in Table 4.1.

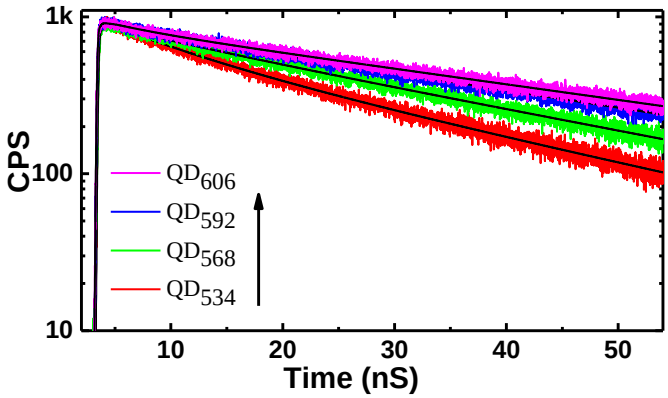

Figure 4.12. TCSPC results for CS QDs synthesized using unpurified core QDs. Straight lines are the fit to all these curves.

Table 4.1. The chart summarizes emission wavelength and luminescence lifetime as a function of shell thickness for CdTe/CdSe CS QDs synthesized without purification CdTe seed QDs. TCSPC data of CS QDs are fitted with equation 4.1.

Sample	**λ emission (nm)**	**Quantum Yield (%)**	**τ_1 (ns)**	**τ_2 (ns)**	**a_1 (%)**	**a_2 (%)**	**τ_{avg} (ns)**
QD_{532}	561	61	7.2	26	30	70	20.3
QD_{568}	598	35	6.9	31	11	89	28.3
QD_{592}	630	31	5.9	39.2	10	90	35.8
QD_{606}	640	19	4.8	43.6	10	90	39.7

It is noticeable from figure 4.14 and Table 4.1 that average lifetime is a function of shell growth as it is increases with CdSe shell thickness. The thinnest shell (QD_{532}) has average lifetime of ~20 ns which has been increased to ~39.7 ns for QD_{606}. This type of change in lifetime is absent in case of only CdTe (as shown in figure 4.13). This shows that type-II band alignment of CdTe/CdSe core shell structure is actually driving the charge separation process

and thus providing additional active pathways for non-radiative recombination which is competing with radiative luminescence. Such dependence of PL lifetime on shell thickness can only take place when the rate of any additional non-radiative charge trapping process is affected by electron delocalization in the type-II shell layer. Moreover, this happens when non-radiative trapping rates become comparable to the type-II radiative processes and thereby selectively consume a section of photo-excited charge carriers. Such long average lifetime also implies that there are non-radiative decay channels which dominated over radiative decay channels in CS QDs having thicker CdSe shells. This may evidently hinder the CS QDs from achieving high QY (figure 4.11).

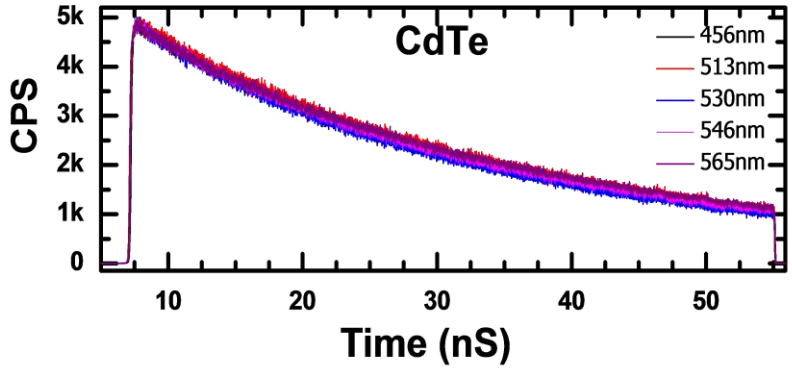

Figure 4.13. TCSPC results showing lifetime of charge carriers in case of CdTe QDs. Comparatively there is no change in lifetime.

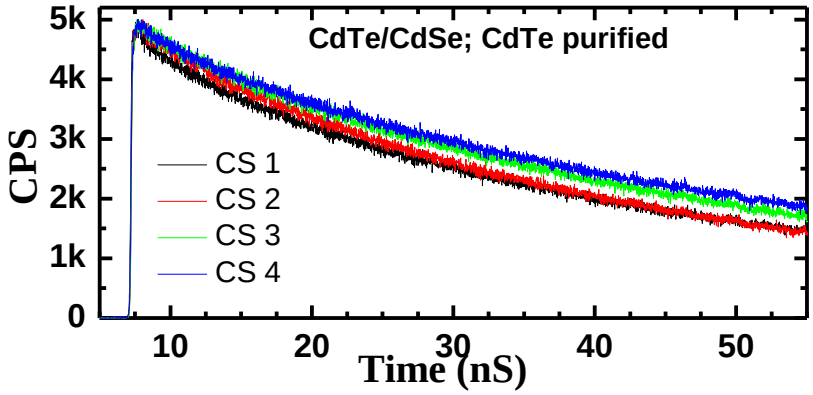

Figure 4.14. TCSPC results for CdTe/CdSe CS QDs synthesised with purified core QDs.

Furthermore, qualitatively similar dependence of PL lifetime on shell thickness is observed in CS QDs synthesized using purified core QDs. The decays spectra for CdTe/CdSe CS QDs synthesized using purified core are given as fig 4.14 for comparison. This similarity proves that optical properties for both types of CS QDs are comparable.

b. Quantum Dot Sensitized Solar Cells Using CdTe/CdSe Core-Shell QDs

We have fabricated Quantum Dot Sensitized Solar cells (QDSSCs) with FTO/TiO_2 along with unpurified CdTe/CdSe CS QDs/ZnS as photo-anode and gold electrode as cathode along with a polysulfide electrolyte in between the electrodes. Fig 4.1 shows a schematic describing the charge separation and charge transfer processes in such type-II sensitized solar cells. Here electron-hole pair is generated in CdTe/CdSe CS QDs after absorbing photons. These photo-generated electrons get transferred from CdTe/CdSe CS QDs to mesoporous TiO_2 layer and are finally collected by the FTO contact. At the same time, photo-generated holes are scavenged by the polysulfide based redox electrolyte which thereby regenerates the reduced QDs. The charge separation and transfer to different electrodes via transparent conducting oxide and electrolyte is a very important process. Trapping of charge carriers also causes a reduction in current density. CdTe is known for a poor SSC efficiency due to inability of hole scavenging using polysulfide electrolyte. On other hand, CdSe shows superior performance as it is more stable[11]. Many more studies have been done on alloy/heterostructure QDs with CdTe as main constitutent[36]. It has been shown that having alloyed formation improves chemical stability of these QDs due to hardened lattice structure and decreased inter-diffusion[36] of polysulfide inside CdTe. Likewise here in this study we are using CdTe/CdSe CS QDs as sensitizer.

As we have seen in ***Chapter 3,*** loading of QDs on TiO_2 coated electrode is found to be one of the major challenges in SSC. Direct growth of QDs on TiO_2 suffers from broad optical absorption due to uncontrolled growth and hence low power conversion efficiency. On the other hand post-synthesis assembly of pre-synthesized QDs shows improvement in efficiency. In case of pre-synthesized QDs the capping ligands are generally bi-linker molecules, here it is MSA. While assembling the pre-synthesized QDs the –SH group is attached to QDs and the terminal carboxyl group of capped QDs can effectively bind the TiO_2 surface. The efficient loading of QDs on TiO_2 is studied by varying loading time. We found that the efficient sensitization is happened only after two hours of loading. Figure 4.15 shows the effect of core/shell QDs

sensitization duration on I-V characteristic of QDSSC. Beyond two hours the excess loading of QDs on TiO_2 gives decrease in J_{SC}. This may be due to excess QDs attached on TiO_2, which can act as electron blocking resistive layers. The unaffected open circuit voltage (V_{OC}) may highlight the fact of unaltered size of core/shell QDs due to aggregation as well as interaction of dangling bonds of QDs.

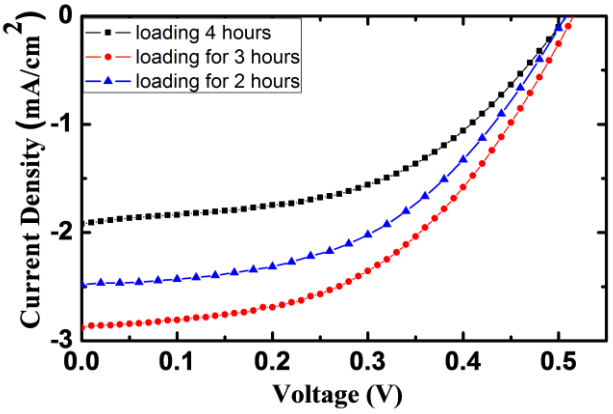

Figure 4.15. Effect of loading duration on performance of sensitized solar cell.

In order to get higher efficiency the photo-generated charge carriers have to be collected at the respective electrodes without much delay. Significant delay in charge collection due to trappings at electronic defects in the conduction path reflects with decrease in J_{SC}. The organic linker molecules are insulating in nature and presence of such layer can also provide further barriers for transport of charge carriers. The removal of bi-linker molecule is very important in the device fabrication process and that can be done by sintering the sensitized photoanode. The effect of sintering sensitized photoanode at different temperature is studied. Figure 4.16 shows J-V characteristic for SSC fabricated using QD_{606} (i.e. thickest shell CS QDs) and sintered at different temperature. The sintering is done in muffle furnace in controlled manner. Photo-anode without sintering at all is used as reference. Few photo-anodes are heated at 200˚C. We found that sintering at 200˚C increases the current density by 29% compared to non-sintered photo-anodes. Further sintering at high temperature ~400 ˚C is done in controlled manner because we observed that film cracks due to sudden increase in temperature. So the sintering of photo-anodes at high temperature is done with first heating photo-anode at 250 ˚C for 10mins and then further kept at 400 ˚C for 5 mins. We established that the sintering of photoanode is a very beneficial step for these CdTe/CdSe based CS nanoparticles sensitized cell as it shows

improvement in the photocurrent. The measured current density is found to be increased compared to the without sintered photo-anodes and photo-anodes sintered at 200 ˚C. However, not much effect of sintering is observed on open circuit voltage (V_{OC}). The parameters J_{SC}, V_{OC} including efficiency (η) and fill factor (FF) for cells sintered at different temperature are given in the table 4.2 for comparison. The only obvious reason for getting such high improvement in current density is removal of bi-linker molecules through sintering. The sintering of sensitized photo-anode at 400 ˚C is found to increase J_{SC} by 102% and overall efficiency by 83% compared to non-sintered photo-anodes.

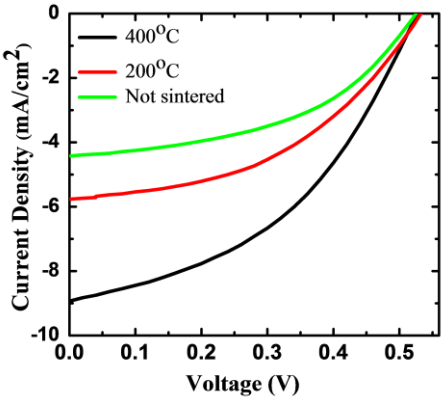

Figure 4.16. Effect of sintering photoanode on J_{SC} and efficiency.

Table 4.2. Effect of sintering temperature on the performance of solar cell is studied. Parameters obtained from J-V characteristic in figure 4.16. Software from Science-tech is used in order to extract values of FF.

Sintering Temperature	**J_{SC} mA/cm^2**	**V_{OC} V**	**FF**	**η %**
RT	4.4	0.52	0.47	1.08
200 ˚C	5.7	0.53	0.46	1.39
400 ˚C	8.9	0.53	0.42	1.98

As we have seen in ***Chapter 3***, CdTe undergoes degradation due to reaction with polysulfide. Here we will address the following question. Will the shell layer on CdTe help to improve the efficiency of SSC as it tries to minimize the direct contact of electrolyte with CdTe? In this study

we used fixed core i.e. CdTe and effect of shell layer thickness i.e. CdSe on SSC performance is studied. Samples with different shell thickness and so different absorption maximum wavelength are like QD_{534}, QD_{568}, QD_{592} and QD_{606} used as sensitizer. Figure 4.17 shows I-V characteristic for SSC fabricated using CdTe/CdSe CS QDs with different shell thickness after sintering at 400˚C. The observed values of short circuit current density (J_{SC}), open circuit voltage (V_{OC}) and fill factor (FF) is given in table 4.3. In this experiment we did not find any change in V_{OC}. But much larger increment is observed in J_{SC} and so in the efficiency of SSC. The systematic increase in J_{SC} is attributed to the extending light absorption range with increase in shell thickness. The second possible reason might be the increased separation of CdTe/CdSe interface from electrolyte. If the chemical instability of CdTe is affecting the current density and efficiency, then the increased shell thickness might have succeeded in creating blocking layer in between electrolyte and QDs. Therefore, higher the thickness, higher is the blocking/separation of electrolyte and CdTe and so the higher current density and efficiency. Apart from electrolyte/CdTe separation we also had the benefit of having type-II heterostructures, which activates charge separation. Radiative recombination is a major problem in solar cell which affects the current density. These type-II CdTe/CdSe core/shell hetero-structure spatially separates charge carriers into two different materials (core and shell) which suppress radiative recombination probability. This is also proved from QY measurement and life time data as shown figure 4.11 and 4.12. As a result we found large ~300% increase in J_{SC} in the QD with thickest shell as compared to CS QDs having thinner shells.

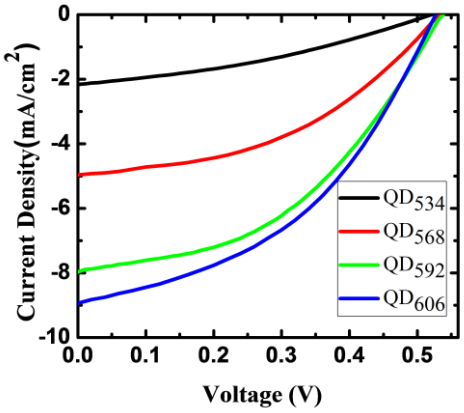

Figure 4.17. J-V characteristic for SSC fabricated with different shell thickness core/shell QDs.

Table 4.3. Parameters obtained from I-V characteristic given in figure 4.17. Here SSCs are fabricated with CS QDs having different shell thickness. The effect of shell thickness on the J_{SC} and η is tabulated here.

Sample	**J_{SC} (mA/cm^2)**	**V_{OC} V**	**FF**	**η %**
QD_{534}	2.2	0.52	0.35	0.4
QD_{568}	5	0.53	0.45	1.19
QD_{592}	8	0.53	0.44	1.86
QD_{606}	8.9	0.53	0.42	1.98

The overall highest efficiency observed in these SSC with largest shell thickness is ~2%. This is close to the value of 2.4% reported for SSC of similar material systems prepared using complex synthesis routes at much higher synthesis temperatures. Comparable efficiency is also observed for the sample having highest shell thickness in case of CdTe/CdSe core/shell QDs synthesized using purified core i.e. CS4. Apart from having similarity in optical and structural properties, both cells with purified and unpurified QDs also show comparable power conversion efficiency which proves importance of this easy and quick synthesis method.

IV. Conclusions

Cost is one of the most important primary concerns of Solar Cell fabrication. Therefore, any research in solar energy materials is important if it provides a better and economic way of making good quality materials for solar cells having reasonable efficiency. Here we are reporting a novel synthesis step which can reduce the overall time and cost of material synthesis as well as solar cell fabrication. We have showed that aqueous wet chemical nanofabrication of charge separating type-II CdTe/CdSe CS QDs at low enough temperature of ~ 80 ˚C using purified and unpurified cores finally produce CS heterostructure QDs having good structural and optical properties. We have also demonstrated that one can use such easy and quick synthesis of

CdTe/CdSe CS QDs without seed purifications to fabricate sensitized solar cells having power conversion efficiency of ~2%. This nanofabrication strategy aims towards procedural simplification of CS synthesis with additional benefit of high reproducibility. Longer PL lifetimes observed in both cases of CS QDs with thicker shells implies that more non-radiative decay channels are being added at the CS junction with increasing CdSe shell layer. This causes a significant decrease in PL QY in CS QDs having thicker shells. Most interestingly, luminescence decay rates of these CdTe/CdSe CS heterostructure QDs prepared by both procedures are also nearly similar. This similarity again reflects on the importance and utility of this economic route of using unpurified seeds in aqueous synthesis for mass production of such technologically important CdTe/CdSe CS QDs for their application in optoelectronics and nano-photovoltaic devices. We also found that the sintering of sensitized TiO_2 photo-anode at high temperature (~400 ˚C) is very important in order to remove insulating ligands and thereby improve performance of the devices. The efficiency and short circuit current density is also found to be a function of shell thickness as it is increases three fold with increase in shell thickness.

V. References

[1] B. O'Regan, M. Gratzel, A low cost, high efficiency solar cell based on dye sensitized colloidal TiO_2 films, Nat. 335, 737-740, 1991.

[2] P. K. Santra, P.V. Kamat, Mn-doped quantum dot sensitized solar cells: a strategy to boost efficiency over 5%, J. Am. Chem. Soc. 134, 2508-2511, 2012.

[3] J. Luo, H. Wei, Q. Huang, X. Hu, H. Zhao, R. Yu, D. Li, Y. Luo and Q. Meng, Highly efficient core–shell $CuInS_2$–Mn doped CdS quantum dot sensitized solar cells, Chem. Commun., 49, 3881-3883, 2013.

[4] Y.-L. Lee, Y.-S. Lo, Highly efficient quantum-dot-sensitized solar cell based on co-sensitization of CdS/CdSe, Adv. Funct. Mater. 19, 604–609, 2009.

[5] G. Zhu, L. Pan, T. Xu, Z. Sun, CdS/CdSe-Cosensitized TiO_2 photoanode for quantum-dot-sensitized solar cells by a microwave-assisted chemical bath deposition method, ACS Appl. Mater. and Interface 3, 3146-3151, 2011.

[6] J. Tian, R. Gao, Q. Zhang , S. Zhang , Y. Li , J. Lan , X.i Qu and G. Cao, Enhanced performance of cds/cdse quantum dot cosensitized solar cells via homogeneous distribution of quantum dots in TiO_2 film. J. Phys. Chem. C, 116 (35), pp 18655–18662, 2012.

[7] X.-Y. Yu, B.-X. Lei, D.-B. Kuang, C.-Y. Su, Highly efficient CdTe/CdS quantum dot sensitized solar cells fabricated by a one-step linker assisted chemical bath deposition, Chem. Sci. 2, 1396-1400, 2011.

[8] S. Itzhakov, H. Shen, S. Buhbut, H. Lin, D. Oron, Type-II quantum-dot-sensitized solar cell spanning the visible and near-infrared spectrum, J. Phys. Chem. C 117, 22203-22210, 2013.

[9] Z. Ning, H. Tian, C. Yuan, Y. Fu, H. Qin, L. Sun, H. Agren, Solar cells sensitized with type-II ZnSe–CdS core/shell colloidal quantum dots, Chem. Commun.47, 1536-1538, 2011.

[10] Z. Pan, H. Zhang, K. Cheng, Y. Hou, J. Hua, X. Zhong, Highly efficient inverted Type-I CdS/CdSe Core/Shell structure QDs sensitized solar cells, ACS Nano 3, 3982-3991, 2012.

[11] J. H. Bang, P. V. Kamat, Quantum dot sensitized solar cells. A tale of two semiconductor nanocrystals: CdSe and CdTe, ACS Nano 3, 1467-1476, 2009.

[12] S. M. McGregor, I. M. Dharmadasa, I. Wadsworth and C. M. Care, Growth of CdS and CdTe by electrochemical technique for utilization in thin film solar cells. Opt.Mater., 6, 75–82, 1996.

[13] D. M. Guldi, I. Zilberman, G. Anderson, N. A. Kotov, N. Tagmatarchis and M. Prato. Nanosized inorganic/organic composites for solar energy conversion. J. Mater. Chem., 15, 114–118, 2005.

[14] X. Wang, H. Zhu, Y. Xu, H. Wang, Y. Tao, S. Hark, X. Xiao and Q. Li, Aligned ZnO/CdTe Core-shell nanocable arrays on indium tin oxide: synthesis and photoelectrochemical properties, ACS Nano, 4 (6), 3302–3308, 2010.

[15] H. McDaniel, N. Fuke, J. M. Pietryga, and V. I. Klimov, Engineered $CuInSe_xS_{2-x}$ quantum dots for sensitized solar cells, J. Phys. Chem. Lett., 4 (3), 355–361, 2013.

[16] J. Zhao, J. A. Bardecker, A. M. Munro, M. S. Liu, Y. Niu, I.-K. Ding, J. Luo, B. Chen, A. K.-Y. Jen, D. S. Ginger, Efficient CdSe/CdS quantum dot light-emitting diodes using a thermally polymerized hole transport layer, Nano Lett. 6, 463-467, 2006.

[17] A. Makhal, H. Yan, P. Lemmens S. K. Pal, Light harvesting semiconductor core-shell nanocrystals: ultrafast charge transport dynamics of CdSe-ZnS quantum dots, J. Phys. Chem. C 114, 627-632, 2010.

[18] S. Deka, A. Quarta, M. G. Lupo, A. Falqui, S. Boninelli, C. Giannini, G. Morello, M. D. Giorgi, G. Lanzani, C. Spinella, R. Cingolani, T. Pellegrino, L. Manna, CdSe/CdS/ZnS double shell nanorods with high photoluminescence efficiency and their exploitation as bio-labeling probes, J. Am. Chem. Soc. 131, 2948-2958, 2009.

[19] H. Wang, T. Wang, X. Wang, R. Liu, B. Wang, H. Wang, Y. Xu, J. Zhang, J. Duan, Double-shelled ZnO/CdSe/CdTe nanocable arrays for photovoltaic applications: microstructure evolution and interfacial energy alignment, J. Mater. Chem. 22, 12532-12537, 2012.

[20] H. Zhong , Y. Zhou, Y. Yang, C. Yang, and Y. Li, Synthesis of Type II CdTe−CdSe nanocrystal heterostructured multiple-branched rods and their photovoltaic applications, J. Phys. Chem. C, 111 (17), 6538–6543, 2007.

[21] K. Wang, J. Chen, W. Zhou, Y. Zhang, Y. Yan, J. Pern and A. Mascarenhas, Direct growth of highly mismatched type II ZnO/ZnSe core/shell nanowire arrays on transparent conducting oxide substrates for solar cell applications, Adv. Mater., 20 (17), 3248-3253, 2008.

[22] H. Wang, T. Wang, X. Wang, R. Liu, B. Wang, H. Wang, Y. Xu, J. Zhang, J. Duan, Double-shelled ZnO/CdSe/CdTe nanocable arrays for photovoltaic applications: microstructure evolution and interfacial energy alignment, J. Mater. Chem. 22, 12532-12537, 2012.

[23] S. A. Ivanov, A. Piryatinski, J. Nanda, S. T., K. R. Zavadil, W. O. Wallace, D. Werder and V. I. Klimov, Type-II Core/Shell CdS/ZnSe nanocrystals: synthesis, electronic structures, and spectroscopic properties, J. Am. Chem. Soc. 129, 11708-11719, 2007.

[24] L. P. Balet, S. A. Ivanov, A. Priyatinski, M. Achermann and V. I. Klimov, Inverted core/shell nanocrystals continuously tunable between type-I and type-II localization regimes, Nano Lett. 4, 1485-1488, 2004.

[25] P. Reiss, M. Protiere, L. Li, Core/Shell semiconductor nanocrystals, Small 5, 154-168, 2009.

[26] E. Groeneveld, S. v. Berkum, M. M. van Schooneveld, A. Gloter, J. D. Meeldijk, D. J. van den Heuvel, H. C. Gerritsen, C. de M. Donega, Highly luminescent (Zn,Cd)Te/CdSe colloidal heteronanowires with tunable electron−hole overlap, Nano Lett. 12, 749-757, 2012.

[27] S. Taniguchi, M. Green, S. B. Rizvi, A. Seifalian, The one-pot synthesis of core/shell/shell CdTe/CdSe/ZnSe quantum dots in aqueous media for in vivo deep tissue imaging, J. Mater. Chem. 21, 2877-2882, 2011.

[28] D. N. Dirin, R. B. Vasiliev, M. S. Sokolikova, A. M. Gaskov, Synthesis, morphology and optical properties of colloidal CdTe/CdSe and CdTe/CdS nano heterostructures based on CdTe Tetrapods, Inorg. Mat. 47, 23-28, 2011.

[29] M. W. DeGroot, N. J. Taylor, J. F. Corrigan, Molecular nanocluster analogues of CdSe/ZnSe and CdTe/ZnTe core/shell nanoparticles, J. Mater. Chem. 14, 654-660, 2004.

[30] T. Mokari and U. Banin, Synthesis and Properties of CdSe/ZnS Core/Shell Nanorods, Chem Mater., 15 (20), 3955–3960, 2003.

[31] D. Gerion , F. Pinaud , S. C. Williams , W. J. Parak , D. Zanchet, S. Weiss and A. P. Alivisatos, Synthesis and properties of biocompatible water-soluble silica-coated cdse/zns semiconductor quantum dots, J. Phys. Chem. B, 105 (37), 8861–8871, 2001.

[32] M.-Q Dai, W. Zheng, Z. Huang, L.-Y. L. Yung, Aqueous phase synthesis of widely tunable photoluminescence emission CdTe/CdS core/shell quantum dots under a totally ambient atmosphere, J. Mater. Chem. 22, 16336-16345, 2012.

[33] W. Zhang, G. Chen, J. Wang, B.-C. Ye, X. Zhong, Design and synthesis of highly luminescent near-infrared-emitting water-soluble CdTe/CdSe/ZnS core/shell/shell quantum dots, Inorg. Chem. 48, 9723-9731, 2009.

[34] K. Yu, B. Zaman, S. Romanova, D-S. Wang, J. A. Ripmeester, Sequential synthesis of Type II colloidal CdTe/CdSe Core–Shell nanocrystals. 1 (3), 332-338, 2005.

[35] R. Zeng, T. Zhang, J. Liu, S. Hu, Q. Wan, X. Liu, Z. Peng and B. Zou, Aqueous synthesis of type-II CdTe/CdSe core–shell quantum dots for fluorescent probe labeling tumor cells, Nanotechnology 20, 095102, 2009.

[36] Z. Pan, K. Zhao, J. Wang, H. Zhang, Y. Feng, X. Zhong, Near-Infrared absorption of $CdSe_xTe_{1-X}$ alloyed quantum dot sensitized solar cells with more than 6% efficiency and high stability, ACS Nano 7, 5215-5222, 2013.

[37] J. Jack Li , Y. Andrew Wang , Wenzhuo Guo , Joel C. Keay , Tetsuya D. Mishima , Matthew B. Johnson , and Xiaogang Peng, Large-scale synthesis of nearly monodisperse CdSe/CdS core/shell nanocrystals using air-stable reagents via successive ion layer adsorption and reaction, J. Am. Chem. Soc. 125 (41), 12567–12575, 2003.

[38] X. Peng , M. C. Schlamp , A. V. Kadavanich and A. P. Alivisatos , Epitaxial growth of highly luminescent CdSe/CdS Core/Shell nanocrystals with photostability and electronic accessibility, J. Am. Chem. Soc., 119 (30), 7019–7029, 1997.

[39] I. Mekis , D. V. Talapin , A. Kornowski, M. Haase and H. Weller, One-pot synthesis of highly luminescent cdse/cds core−shell nanocrystals via organometallic and "greener" chemical approaches, J Phy. Chem. B, 107 (30), 7454–7462, 2003.

[40] S. –Q. Fan, B. Fang, J. H. Kim, B. Jeong, C. Kim, J.-S Yu and J. Ko, J. Ordered multimodal porous carbon as highly efficientcounter electrodes in dye-sensitized and quantum-dot solar cells. Langmuir, 26, 13644–13649, 2010.

[41] S. –Q. Fan, B. Fang, J. H. Kim, B. Jeong, C. Kim, J.-S Yu and J. Ko, Hierarchical nanostructured spherical carbon with hollow core/mesoporous shell as a highly efficient counter electrode in CdSe quantum-dot-sensitized solar cells. Appl. Phys. Lett., 96, 063501, 2010.

[42] S. –Q. Fan, B. Fang, J. H. Kim, B. Jeong, C. Kim, J.-S Yu and J. Ko, J. Highly efficient CdSe quantum-dot-sensitized TiO2 photoelectrodes for solar cell applications. Electrochem. Commun., 11, 1337–1339, 2009.

[43] A.V.R. Murthy, Padmashri Patil, Shouvik Datta, Shivprasad Patil, Photoinduced dark fraction due to blinking and photodarkening probability in aqueous CdTe quantum dots. J. Phys. Chem. C. 117, 13268-75, 2013.

[44] A. M. Smith, A. Mohs, S. Nie, Tuning the optical and electronic properties of colloidal nanocrystals by lattice strain, Nat. Nano Tech. 4, 56-63, 2009.

[45] J.-Y. Liao, B.-X. Lei, D.-B. Kuang, C.-Y. Su, Tri-functional hierarchical TiO2 spheres consisting of anatase nanorods and nanoparticles for high efficiency dye-sensitized solar cells, Energy Environ. Sci. 4, 4079-4085, 2011.

[46] Y.-L. Lee, C.-H. Chang, Efficient polysulfide electrolyte for CdS quantum dot-sensitized solar cells, J. Power Sources 185, 584-588, 2008.

[47] R. J. Bandaranayake, G. W. Wen, J. Y. Lin, H. X. Jiang, C. M. Sorensen, Structural phase behavior in II–VI semiconductor nanoparticles, Appl. Phys. Lett. 67, 831-833, 1995.

[48] C.-H. Chuang, S. S. Lo, G. D. Scholes, C. Buruda, Charge separation and recombination in CdTe/CdSe core/shell nanocrystals as a function of shell coverage: probing the onset of the quasi Type-II regime, J. Phys. Chem. Lett. 1, 2530-2535, 2010.

[49] S. Kim, B. Fisher, H-J. Eisler, M. Bawendi, Type-II quantum dots: CdTe/CdSe(core/shell) and CdSe/ZnTe(core/shell) heterostructures, J. Am. Chem. Soc. 125, 11466-11467, 2003.

Chapter 5

Ligand-Free, Non-Toxic $AgInS_2$ Quantum Dots for Sensitized Solar Cells

I. Introduction

We have discussed in ***Chapter 3*** that size-tunable, non-reacting, stable colloidal Quantum Dots (QDs) are desirable for achieving higher efficiency in Quantum Dot sensitized solar cell (QDSSC). Further in ***Chapter 4*** we have shown that, how core/shell heterostructure of CdTe/CdSe QDs can achieve this goal. In ***Chapter 4,*** we have also seen that efficiency increases by many folds with use of core/shell structure. The need of capping/ligand molecule is to make QDs soluble, stable in colloidal solution, non-oxidizing as well as to prevent agglomeration to control the final active sizes of these QDs[1] as discussed in previous chapters. We have discussed that these ligands/capping molecules are insulating in nature, so presence of such insulating capping layers creates barrier for charge transfer and further affects the resultant power conversion efficiency of any QDSSCs. We have also discussed that one way to overcome this barrier is high temperature sintering of photo-anode[2,3,4]. There are several reports which show increase in efficiency of solar cell by sintering of photo-anode at higher temperature but it is also

well known fact that sintering also leads larger crystallite size and thereby it decreases the enhanced photo-absorption due to reduced quantum confinement effect. Additionally, various post-synthesis surface modification procedures have been reported previously in order to replace the insulating organic ligands with an electronically conducting ligand[5,6,7,8,9,10,11,12,13,14,15]. Talapin et al. demonstrated very high charge carrier mobilities from a QD film by using inorganic ligands like molecular metal chalcogenides and chalcogenides[16,17]. There are also reports of single-step synthesis of all-inorganic colloidal nanocrystals (NCs), for example, oxide NCs with OH^-/H_2O on the surface[18,19]. Instead of all that tedious synthesis and fabrication processes, here we present results on QDSSC fabrication using ligand-free QDs[20].

Our collaborator Dr. Angshuman Nag, IISER-Pune previously reported a generic protocol for synthesis of binary and ternary ligand-free metal sulfide NCs[21]. $AgInS_2$ is a I-III-VI_2 semiconductor which can crystallize in both chalcopyrite and orthorhombic phases exhibiting direct band gaps of 1.87 and 1.98 eV, respectively, at room temperature[22]. The band gap is suitable for absorption and emission of visible light, and thus $AgInS_2$ is an interesting alternative for both solar cell and light emitting applications. Synthesis of colloidal $AgInS_2$ QDs has been reported rather recently using both thermolysis of precursors of molecular metal-sulfur complex and reaction of metal cations and sulfur[23,24,25,26,27,28,29,30,31,32]. So far, the main emphasis has been on the luminescence property of $AgInS_2$ QDs for biological application,[31,33,34,35,36] along with two reports on photovoltaic cell[30,37] and a report on nonlinear optical property[23]. Very recently, $AgInS_2$ QDs[38] and Cu-doped $AgInS_2$ QDs[39] have also been incorporated in organic-inorganic hybrid optoelectronic devices.

We have used this ligand-free $AgInS_2$ QDs synthesized by members of the research group headed by Dr. Angshuman Nag using a method similar to ref [21], followed by a post-synthesis thermal annealing of QDs that modifies the size and defect density of QDs[20]. Here, we have shown that a modification of defect states plays a crucial role not only in determining the optical absorption and light emission but also in solar cell performance of these QDs. In this work, we have used solution processed ligand-free $AgInS_2$ QDs grown by Dr. Angshuman Nag's research group to form photo-anode of quantum dot sensitized solar cells (QDSSC) exhibiting 0.8% power conversion efficiency. We have shown that open circuit voltage (V_{OC}), Short circuit

current density (J_{SC}) and the efficiency increases systematically with a decrease in the mid-gap defect states of $AgInS_2$ QDs.

II. Experimental Section

Synthesis Procedure

The details about chemicals required, synthesis procedure and purification technique for $AgInS_2$ QDs is given in reference[21] as well as in the supporting information of reference[20]. The ligand-free $AgInS_2$ QDs are synthesized by Dr Angshuman Nag's research group at IISER-Pune and supplied to us for sensitized solar cell fabrication.

III. Results and Discussions

a. Optical Properties of $AgInS_2$ QDs

The organic capping layer gives stability, solubility to the QDs as well as avoids their agglomeration. In ligand free QDs this step is completed by providing extra negative charge on QDs surface by carrying out the reaction with excess S^{2-} while QDs are forming. Presence of negative charge on QD's surface makes them repel from each other and thus providing colloidal stability in a polar solvent. The presence of negative charge on the surface is further confirmed by Dr. Nag's group using ζ-potential[20]. Other proofs for ligand-free QDs are also provided in the same report using FTIR and TGA analysis by Dr. Angshuman Nag[20,21].

UV-Visible absorption spectrum of $AgInS_2$ QDs processed at reaction temperature is studied by Dr. Angshuman Nag's group[20]. The spectrum is a broad featureless one with a significant absorption observed at energies even below the band gap of bulk $AgInS_2$. According to them this type optical absorption behavior cannot be explained by a broader size distribution of QDs[20]. Dr. Nag's group observed that the QDs form a stable colloidal solution even after centrifuging at 7000 rpm for 10 minutes which suggest the lower energy absorption tail is not arising from scattering of light by agglomerated QDs. Further they observed that annealing of the colloidal QDs at a higher temperature reduces the absorbance of the tail below bulk band gap,

this appears as a blue shift in the absorption onset. His group also observed that the $AgInS_2$ QDs annealed at 150 ˚C show appearance of excitonic absorption feature around 2.1 eV, which is higher than the band gaps of both orthorhombic and chalcopyrite $AgInS_2$, suggesting confinement of charge carriers in QDs[20]. Moreover, they have also studied TEM images of $AgInS_2$ QDs for QDs dispersion after heating from 70 to 150 ^oC which shows an increase in QD's size from 2.5 nm to 5.8 nm[20]. Therefore the blue-shift in absorbance onset is not because of decrease in QDs size with increasing annealing temperature, as in contrast, QDs size actually increased with increasing annealing temperature[20]. This information will be particular useful to analyze the results of solar cell made out of these nanomaterials. Selected area electron diffraction (SAED) patterns are also studied by his group which shows that the crystal structures of QDs remain same i.e. orthorhombic phase during the annealing process[20]. Therefore, there is no possibility of different crystal structure modifying the band gap after annealing the QD's dispersion.

To put things in to proper perspective for analysisng the results of QDSSC made using these ligand free $AgInS_2$ QDs, they note that the absorption tail at energies lower than the band gap has also been observed previously in doped/disordered semiconductors, and is often termed as Urbach tail[20,40,41]. Plots of absorbance in logarithmic scale vs photon energy show somewhat linear regions below bulk band gap suggesting the possibility of Urbach tails in $AgInS_2$ QDs[20]. According to Dr. Nag, conclusive assignment is not possible from these data since the typical UV-visible absorption spectrometer cannot measure absorbance over several orders of magnitude, which is required to study Urbach tail. Generally, such a tail arise from light absorption involving localized states in the mid gap region. Ag-S and In-S bonds have different strengths, and are known to generate various defects like interstitial Ag, Ag vacancy, S vacancy and interstitial S in bulk $AgInS_2$ crystal[20,41]. These defect states are localized states with poor overlap of electronic wave-functions and typically have a poor absorption coefficient. High defect density, and consequently, closer proximity of defects, both owing to small QDs size, lead to measurable defect-state related absorption in QDs[40]. According to Dr. Nag's observation, an increase in annealing temperature reduces lower energy absorption tail by[20] (i) improving the crystallinity by reducing intrinsic defects, and (ii) increasing the QD size due to reduced surface related defects. Also, larger QDs with lesser defects can increase the spatial separation between

defect sites, which in turn reduces the absorption coefficient. Apart from the absorption spectroscopy results PL excitation (PLE) spectra and PL decay dynamics for $AgInS_2$ QDs annealed at 150˚C is also studied by Dr. Angshuman Nag's group[20]. All these studies suggest defect-related emissions arising from smaller QDs have higher energies compared to those arising from larger QDs within the same sample of QD ensemble. So, we have used two different samples of $AgInS_2$ QDs. One which is as prepared without any post-synthesis annealing that contains lot of defects hence shows below band gap absorption. And 2nd one is sample which is annealed at 150˚C after completion of reaction that contains comparatively less defects. We have tried to see how such defect related electronic transitions play an active role in the photovoltaic characteristics of QDSSC made using these differently processed ligand free $AgInS_2$ QDs.

Based on these studies they have come up with a schematic showing defect state which can contribute in the light emission process via two different paths[20]. They suggest one path describes emission involving transitions from (to) localized defect states to (from) delocalized valence (conduction) band and another path describes emission involving two dip and localized defect states, and termed as donor-acceptor (D-A) transition[20]. Luminescence from increase in annealing temperature increases the QD size, and exhibit a red shift in PL spectra[20].

b. Quantum Dot Sensitized Solar Cells (QDSSCs)

Broad band absorption of sun light, large absorption coefficient and non-toxic nature of the material has motivated researchers to develop QDSSCs using these I-III-V_2 semiconductors as photosensitizer[42,43,44,45] having size tunable energy gap. We have fabricated QDSSCs having FTO/TiO_2/Ligand-free $AgInS_2$ QDs as anode and gold electrode as cathode along with a polysulfide electrolyte in between the electrodes. The preparation of thin film of TiO_2 electrode is discussed in ***Chapter 3 section IId and IIe***. $AgInS_2$ QDs dispersed in DMF is then pipetted directly on the mesoporous TiO_2 film and allowed to stay for 2 hrs at room temperature[46]. The loading of QDs on porous TiO_2 thin film is confirmed from the changed color of anode as shown in figure 5.1.

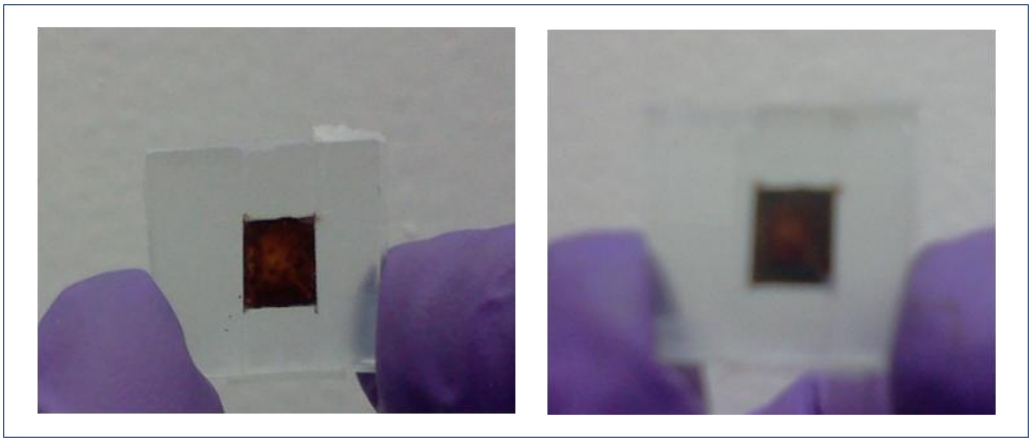

Figure 5.1. Color obtained by porous TiO_2 after loading of $AgInS_2$ QDs a) front side and b) back side of photo-electrode.

The final photoanode is made by washing the resulting film with ethanol and sintering it at 100 ˚C inside a N_2 filled glove box for 1hr. The cell is prepared by assembling QDs sensitized electrode and Au as counter electrode using 50 micron thick scotch spacer with 10 microlit polysulfide electrolyte. The polysulfide electrolyte consists of Na_2S (0.5 M), sulfur powder (2 M) and KCl (0.2 M) is mixed solvent containing methanol : water (7:3 v/v)[4]. The cell area is kept constant to 0.16 cm^2. The cells are illuminated using Newport solar simulator provided with AM1.5G at one sun intensity (100 mW/cm^2). Current density-voltage (I-V) characterization is done using Keithley 2611 source meter.

The absorbance of photons generates electron-hole pairs. For efficient solar cell functionalization, photo generated charge carriers should be separated and collected at the anode and cathode without any loss due to recombination/trapping. Many a times the presence of electronic defects acts as trapping centers to charge carriers which further affects the overall charge collection and so the current density and open circuit voltage. In case of $AgInS_2$ sensitized solar cell the mechanism for charge transfer is as shown in Figure 5.2. Here, the $AgInS_2$ QDs works as sensitizer/photo-absorber. The absorption of photons generates electron-hole pairs in these QDs.

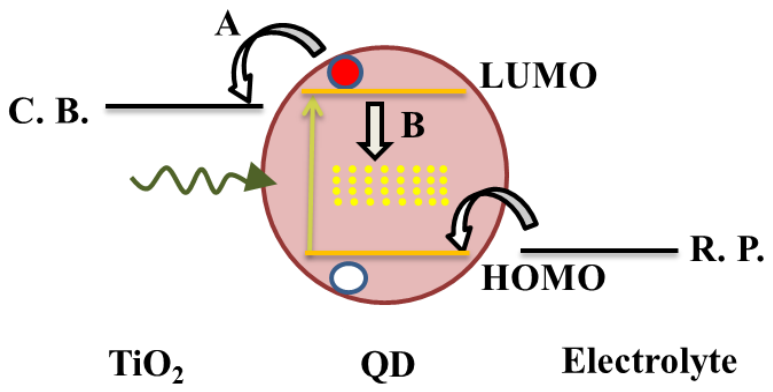

Figure 5.2. Charge transfer mechanism for sensitized solar cell. CB is conduction band for TiO_2, and RP is redox potential for electrolyte. Arrows demonstrate direction of electron transfers. Channel A represents the electron transfer from QDs to TiO_2 and channel B represents non-radial recombination of electron and hole via defect state. Arrows represents the direction of electron transfer.

The process A in figure 5.2 shows such transfer of charge carriers like the photo-generated electrons can be transferred from ligand-free $AgInS_2$ QDs to mesoporous TiO_2. These electrons are finally collected by the FTO contact. At the same time, photo-generated holes are scavenged by the polysulfide based redox electrolyte which thereby regenerates the QDs. To the date it is well known that polysulfide is stable electrolyte, very effective in scavenging holes from photo absorbing material. The other option is iodide/triodide redox. However, the iodide/triodide redox is known to degrade the QD's. The instability using iodide/triodide is caused by the presence of surface states on pre-synthesized QDs which can trap the photo-excited electrons. I_3^- in electrolytes can capture those trapped electrons and lead to the accumulation of holes in QDs, and then cause the degradation[47]. Here the process B indicates loss in charge carriers through trapping/recombination due to presence of defects. The trapping of charge carriers in defects affects the carriers transfer from QDs to electrodes and finally reflect in lower efficiency.

We have measured photocurrent spectrum of a prototype device. Results are given below as figure 5.3. The photocurrent plot qualitatively resembles with UV-visible spectrum of used QDs[20,21].

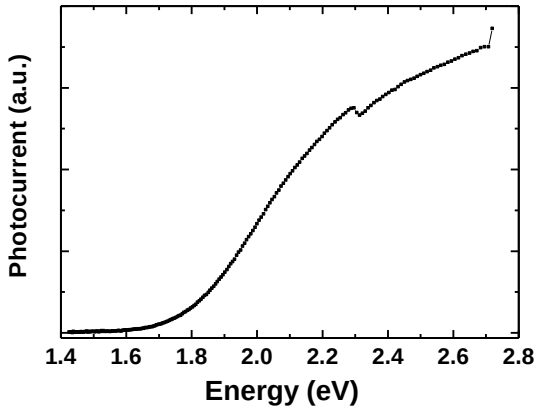

Figure 5.3. Photocurrent response spectrum of $AgInS_2$ sensitized solar cell.

The current density (J) vs voltage (V) characteristics for QDSSCs fabricated using ligand-free $AgInS_2$ QDs prepared after post-synthesis annealing of colloidal QDs at 70 ˚C and 150 ˚C is studied and as given in the figure 5.4. The essential solar cell parameters have been extracted from the plots and provided in Table 5.1.

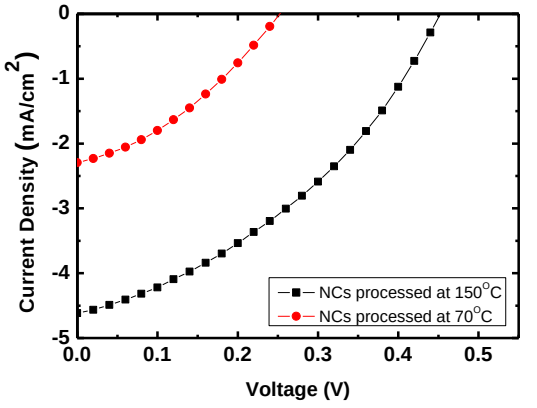

Figure 5.4. J-V characteristics for QDSSC fabricated using two differently processed ligand-free $AgInS_2$ QDs: colloidal QDs annealed at 70 °C and 150 °C.

The band gap of photo-absorbing material (i.e. sensitizing material) is the maximum attainable V_{OC}[48] for a QD. The main hurdle in attaining higher V_{OC} comes from mismatch of energy levels in the photo-absorber and the electrical contacts (CB of TiO_2 and RP of the electrolyte) as well as from the non-radiative recombination rates of electron-hole pair through the defect states of the QD. Presence of defect levels in the QDs at a level below the conduction

band edge of TiO_2 provides significant non-radiative trapping sites for photo-generated charge carriers shown as channel B in Figure 5.2. This certainly reduces the amount of photo-generated charge carriers collected via channel A. On the other hand, absence of these defect sites reduce the trapping of photo-generated charge carriers via channel B, which in-turn increase the amount of charge collection via channel A and J_{Sc}. The measured V_{OC} is proportional to the logarithm of this J_{Sc}. Therefore, any defect mediated reduction in J_{SC} also reduces the V_{OC} and vice versa. From Table 1, we notice that the $AgInS_2$ QDs dispersion annealed at 150 ˚C with a sharper mid-gap absorption tail exhibit higher V_{OC} compared to the QDs annealed at 70 ˚C. Annealing the QDs at 150 ˚C drastically reduces faster defect-related non-radiative decay channels, and the longer lifetime of excited electron is expected[49,50,51] to enhance V_{OC}. Therefore, observed increase in V_{OC} for $AgInS_2$ QDs with increasing annealing temperature can be attributed to the selective removal of mid-gap states as explained by the sharper mid-gap absorption.

Table 5.1. Solar cell parameters obtained from J-V characteristic of respective cells in Figure 5.5. A software from Sciencetech is used in order to extract values of FF, $R_{S,}$, R_{Sh}.

QDs annealing temperature/Size	**V_{OC} (V)**	**J_{SC} (mA/cm^2)**	**FF**	**R_S (Ω)**	**R_{Sh} (Ω)**	**η (%)**
70^oC/2.5 nm	0.26	2.3	0.32	416	6000	0.20
150^oC/5.8 nm	0.45	4.62	0.39	270	6300	0.80

Any impediment to the transport and collection of photo-generated charge carriers also affects the overall efficiency of solar cell as directly reflected in the J_{SC} and FF. Here, R_{Sh} quantifying the contribution from leakage current are nearly similar (~ 6 kΩ) for both the devices suggesting qualitatively similar coverage of TiO_2 films with $AgInS_2$ QDs for both devices. On the other hand, R_S comes from contact resistance of the junction and also from the contribution of defects which limits the transport and collection of photo-generated electron and holes. We found lower R_S values for $AgInS_2$ QDs processed at 150 ^oC (R_S ~270 Ω) compared to QDs processed at 70 ^oC (R_S ~ 416 Ω). As a result, the observed decrease in R_S subsequently increases

FF and J_{SC} values for $AgInS_2$ QDs annealed at higher temperature. Further reduction in defect density is required to improve the FF.

To explain the reason behind use of methanol based electrolyte instead of water based electrolyte we have also checked the cell's performance using only aqueous solution based polysulfide as shown in figure 5.5. Here we have used water as solvent for polysulfide electrolyte. This exhibit similar results but with somewhat lower J_{SC} compared to methanol based polysulfide electrolyte. The reason behind obtaining better performance using methanol based electrolyte as compared to water based electrolyte is the fact that an aqueous solution has high surface tension which results in a poor penetrating and wetting of the TiO_2 porous matrix, leading to a poor efficiency of a QDSSC. Compared to water, ethanol and methanol has low surface tension. As photocurrent relies directly on contact between the electrolyte and the QD surface (for hole extraction), use of methanol can increase J_{SC}[52,53] by increasing the penetration and better coverage of TiO_2 surface with QDs.

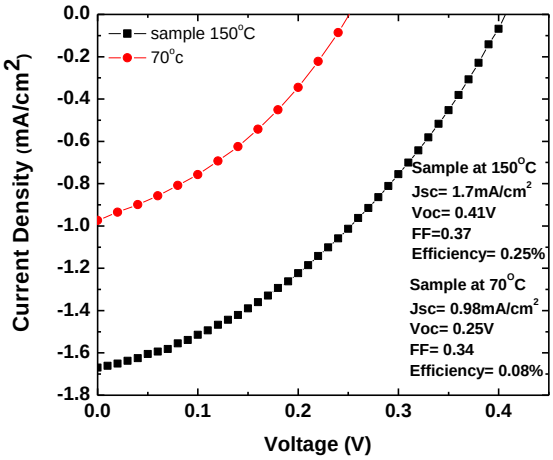

Figure 5.5. J-V characteristics for QDSSC fabricated using two differently processed ligand-free $AgInS_2$ QDs using water based electrolyte.

The EIS measurement done for QDSSC with $AgInS_2$ processed at 150 ˚C using a PARSTAT 2273 Potentiostat from Princeton Applied Research. The EIS measurements are carried out by applying a DC bias at open circuit voltage (V_{OC} = 0.25 V) and also at zero applied bias. EIS is measured with a sinusoidal voltage having rms amplitude of 10 mV in a frequency range from 10^{-2} Hz to 10^5 Hz. The data agrees well with this R_S values as shown in figure

5.4.We have studied EIS response with and without applied bias (fig. 5.6 a, b respectively) in dark as well as under light. The response of solar cell with applied bias is clearly visible in EIS study. Generally, additional arc/semicircles are present at relatively high frequency in the EIS plots. These are usually due to an energy level mismatch between anode work function and the donor molecules[54]. This device does not exhibit any such additional characteristic high frequency arc/semicircular feature related to intrinsic limitations of majority carrier transport. This can be attributed to removal of defects from larger QDs obtained at higher annealing temperature.

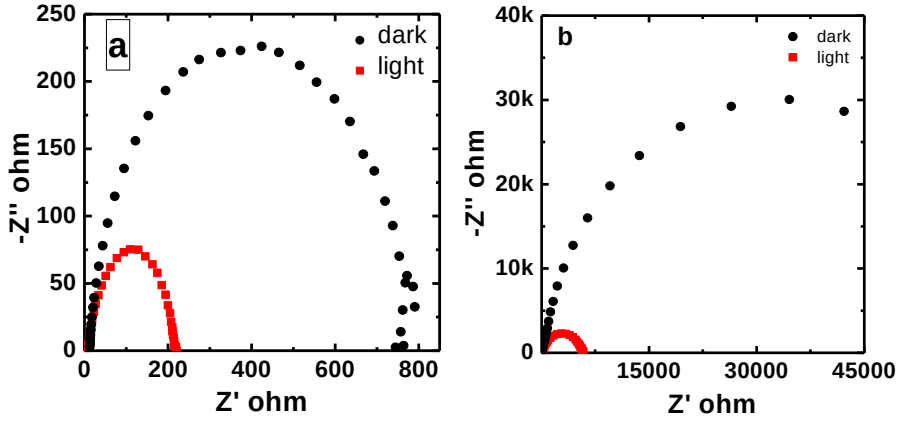

Figure 5.6. EIS response for $AgInS_2$ based QDSSC a) under applied forward bias b) without any applied bias.

The observed improvements in J_{SC}, V_{OC}, and FF with $AgInS_2$ QDs having lesser mid-gap defects are evident from the final efficiency of these QDSSCs. Cells with QDs annealed at 150 ˚C gives an overall maximum efficiency of 0.8% which is ~4 times higher compared to the cells with QDs annealed at low temperature. We note that the ref.[11] of organic capped $AgInS_2$ QD based QDSSC shows a lower value of J_{SC} = 0.91 $mAcm^{-2}$ because of the presence of insulating organic ligands on QD surface, however, our best QDSSC with ligand-free $AgInS_2$ QDs exhibit J_{SC} = 4.62 $mAcm^{-2}$. The higher J_{SC} of our QDSSC can be attributed to easy extraction/transport of charge carries from ligand-free $AgInS_2$ that does not have any insulating organic layer on the QD surface. However, the obtained efficiency (0.8%) is still low compared to that (~5%) of best QDSSCs based on other semiconductor QDs. Apart from optimization of device fabrication, one intrinsic hurdle for high efficiency $AgInS_2$ QD based QDSSC appears to be the high density of

intrinsic defects in the synthesized QDs. This high defect density is not unique to Dr. Nag's synthesis, and rather common in most of organic capped $AgInS_2$ QDs synthesized so far.

IV. Conclusions

In order to avoid drawbacks related to use of QDs with insulating organic capping layer we have used ligand-Free $AgInS_2$ QDs synthesized by Dr. Nag's group, IISER Pune. They have prepared these QDs using a simple single step synthesis at 70 ˚C followed by annealing at 125 ˚C and 150 ˚C. According to their observation all these samples show significant defect-related photo-absorption at energies below the bulk band gap, probably leading to Urbach tail. According to Dr. Nag, higher annealing temperature reduces intrinsic defects, and at the same time formation of larger QD reduces surface defect contribution. QDSSCs are fabricated using $AgInS_2$ QDs as sensitizers, for that purpose we have used QDs annealed at 70 ˚C and 150 ˚C. The presence of defects in QDs clearly visible in the performance of solar cell as it is reflected in the parameters of cells. QDs dispersion annealed at 150 ˚C show higher values of power conversion efficiency (0.8%), V_{OC} (0.45 V) and J_{SC} (4.62 $mAcm^{-2}$) as a consequence partial removal of defect states, compared to QDs annealed at 70 ˚C (0.2%, 0.26 V and 2.3 $mAcm^{-2}$). The obtained solar cell parameters are superior than the previous reports of $AgInS_2$ QDs based solar cells, owing to the ligand-free nature of our QDs facilitating charge transport, and partial removal of defect states following post-synthesis annealing.

V. References

[1] A. L. Rogach, T. Franzl, T. A. Klar, J. Feldmann, N. Gaponik, V. Lesnyak, A. Shavel, A. Eychmuller, Y. P. Rakovich and J. F. Donegan, Aqueous synthesis of thiol-capped cdte nanocrystals: state-of-the-art, J. Phys. Chem. C, 111, 14628-14637, 2007.

[2] Padmashri Patil, Clan Laltanzuala, Shoouvik Datta, Sensitized Solar Cell from Type-II CdTe/CdSe Core/Shell Nanocrystals Synthesized Without Seed Purification at Low Temperature, J. Alloys and Compound, 607, 230-237, 2014.

[3] Z. Pan, H. Zhang, K. Cheng, Y. Hou, J. Hua, and X. Zhong, Highly efficient inverted Type-CdS/CdSe Core/Shell structure QD-sensitized solar cells, ACS Nano, 6, 3982-3991, 2012.

[4] I. Gur, N. A. Fromer, M. L. Geier, A. P. Alivisatos, Air-Stable all-inorganic nanocrystal solar cells processed from Solution, Science, 462, 310, 2005.

[5] D. Yu, C. J. Wang and P. Guyot-Sionnest, n-Type conducting CdSe nanocrystal solids. Science, 300, 1277, 2003.

[6] M. V. Jarosz, V. J. Porter, B. R. Fisher, M. A. Kastner and M. G. Bawendi, Photoconductivity studies of treated CdSe quantum dot films exhibiting increased exciton ionization efficiency, Phys. Rev. B, 70, 195327, 2004.

[7] D. V. Talapin and C. B. Murray, PbSe Nanocrystal Solids for n- and p-channel thin film field-effect transistors, Science , 310 ,86, 2005.

[8] M. Law, J. M. Luther, O. Song, B. K. Hughes, C. L. Perkins and A. J. Nozik, The Structural, optical and electrical properties of pbse nanocrystal solids treated thermally and with simple amines, J. Am. Chem. Soc., 130, 5974, 2008.

[9] M. S. Kang, A. Sahu, D. J. Norris and C. D. Frisbie, Size dependent electrical transport in CdSe nanocrystal thin films, Nano Lett., 10, 3727, 2010.

[10] M. V. Kovalenko, M. Scheele and D. V. Talapin, Colloidal nanocrystals with molecular metal chalcogenide surface ligands, Science, 324, 1417, 2009.

[11] A. G. Dong, X. C. Ye, J. Chen, Y. J. Kang, T. Gordon, J. M. Kikkawa and C. B. Murray, A generalised ligand-exchange strategy enabling sequential surface functionalization of colloidal nanocrystals, J. Am. Chem. Soc., 133, 998, 2011.

[12] A. Nag, M. V. Kovalenko, J. S. Lee, W. Y. Liu, B. Spokoyny and D. V. Talapin, Metal-free inorganic ligands for colloidal nanocrystals: S^{2-}, H^{S-}, Se^{2-}, HSe^{-}, Te^{2-}, HTe^{-}, TeS_3^{2-}, OH^{-}, and NH^{2-} as surface ligands, J. Am. Chem. Soc.,133, 10612, 2011.

[13] A. T. Fafarman, W. K. Koh, B. T. Diroll, D. K. Kim, D. K. Ko, S. J. Oh, X. C. Ye, V. Doan-Nguyen, M. R. Crump, D. C. Reifsnyder, C. B. Murray and C. R. Kagan, Thiocyanate-capped nanocrystal colloids: vibrational reporter of surface chemistry and solution based route to enhanced coupling in nanocrystal solids, J. Am. Chem. Soc., 133, 15753, 2011.

[14] E. L. Rosen, R. Buonsanti, A. Llordes, A. M. Sawvel, D. J. Milliron and B. A. Helms, Exceptionally mild reactive stripping of native ligands from nanocrystal surfaces by using meerwein's salt, Angew. Chem. Int. Ed., 51, 684, 2012.

[15] K. Kravchyk, L. Protesescu, M. I. Bodnarchuk, F. Krumeich, M. Yarema, M. Walter, C. Guntlin and M. V. Kovalenko, Monodisperse and inorganically capped Sn and Sn/SnO_2 nanocrystals for high-performance Li-ion battery anodes, J. Am. Chem. Soc., 135, 4199, 2013.

[16] J. S. Lee, M. V. Kovalenko, J. Huang, D. S. Chung and D. V. Talapin, Band-like transport, high electron mobility and high photoconductivity in all-inorganic nanocrystal arrays, Nat. Nanotechnol., 6, 348, 2011.

[17] D. S. Chung, J. S. Lee, J. Huang, A. Nag, S. Ithurria and D. V. Talapin, Low voltage, hysteresis feee and high mobilitytransistors from all-inorganic colloidal nanocrystals, Nano Lett., 12, 1813, 2012.

[18] R. Viswanatha, S. Sapra, S. Sen Gupta, B. Satpati, P. V. Satyam, B. N. Dev and D. D. Sarma, Understanding the quntum size effects in ZnO nanocrystals, J. Phys. Chem. B, 108 , 6303, 2004.

[19] Y. X. Zhao, E. A. Hernandez-Pagan, N. M. Vargas-Barbosa, J. L. Dysart and T. E. Mallouk, A High Yield Synthesis of Ligand-Free Iridium Oxide Nanoparticles with High Electrocatalytic Activity, J. Phys. Chem. Lett., 2, 402, 2011.

[20] K.P. Kadlag, Padmashri Patil, M. J. Rao, Shouvik Datta and A. Nag, Luminescence and Solar Cell from Ligand-Free Colloidal $AgInS_2$ Nanocrystals, Crys. Chem. Engg. 16, 3605-3612, 2014.

[21] K. P. Kadlag, M. J. Rao and A. Nag, Ligand-Free, Colloidal, and Luminescent Metal Sulfide Nanocrystals, J. Phys. Chem. Lett., 4, 1676, 2013.

[22] J. L. Shay, B. Tell, L. M. Schiavon, H. M. Kasper and F. Thiel,Energy bands of $AgInS_2$ in the chalcopyrite and orthorhombic structures, Phys. Rev. B, 9, 1719, 1974.

[23] L. Tian, H. I. Elim, W. Ji and J. J. Vittal, One Pot Synthesis and Third-order Nonlinear Optical Properties of AgInS2 Nanocrystals, Chem. Commun., 41, 4276, 2006.

[24] W. M. Du, X. F. Qian, J. Yin and Q. Gong, General synthesis of I–III–VI_2 ternary semiconductor nanocrystals, Chem- Euro. J., 13, 8840, 2007.

[25] T. Torimoto, T. Adachi, K. Okazaki, M. Sakuraoka, T. Shibayama, B. Ohtani, A. Kudo and S. Kuwabata, Facile synthesis of ZnS-AgInS2 solid solution nanoparticles for a color-adjustable luminophore, J. Am. Chem. Soc., 129, 12388, 2007.

[26] D. S. Wang, W. Zheng, C. H. Hao, Q. Peng and Y. D. Li, General synthesis of I-III-VI2 ternary semiconductor nanocrystals. Chem. Commun., 2556, 2008.

[27] R. G. Xie, M. Rutherford and X. G. Peng, Formation of high-quality I-III-VI semiconductor nanocrystals by tuning relative reactivity of cationic precursors, J. Am. Chem. Soc., 131, 5691, 2009.

[28] Z. Y. Feng, P. C. Dai, X. C. Ma, J. H. Zhan and Z. J. Lin, Appl. Phys. Lett.,96, 2010.

[29] T. Ogawa, T. Kuzuya, Y. Hamanaka and K. Sumiyama, Synthesis of Ag–In binary sulfide nanoparticles—structural tuning and their photoluminescence properties, J. Mater. Chem., 20, 2226, 2010.

[30] S. J. Peng, S. Y. Zhang, S. G. Mhaisalkar and S. Ramakrishna, Synthesis of AgInS2 nanocrystal ink and its photoelectrical application. Phys. Chem. Chem. Phys., 14, 8523, 2012.

[31] M. D. Regulacio, K. Y. Win, S. L. Lo, S. Y. Zhang, X. H. Zhang, S. Wang, M. Y. Han and Y. G. Zheng, Aqueous synthesis of highly luminescent $AgInS_2$–ZnS quantum dots and their biological applications, Nanoscale, 5, 2322, 2013.

[32] G. Manna, S. Jana, R. Bose and N. Pradhan, Mn-doped multinary CIZS and AIZS nanocrystals, J. Phys. Chem. Lett., 3, 2528, 2012.

[33] T. Uematsu, S. Taniguchi, T. Torimoto and S. Kuwabata,Emission quench of water-soluble ZnS–$AgInS_2$ solid solution nanocrystals and its application to chemosensors, Chem. Commun., 7485, 2009.

[34] T. Torimoto, S. Ogawa, T. Adachi, T. Kameyama, K. I. Okazaki, T. Shibayama, A. Kudo and S. Kuwabata,Remarkable photoluminescence enhancement of ZnS–$AgInS_2$ solid solution nanoparticles by post-synthesis treatment, Chem. Commun., 46, 2082, 2010.

[35] J. Y. Chang, G. Q. Wang, C. Y. Cheng, W. X. Lin and J. C. Hsu, Strategies for photoluminescence enhancement of $AgInS_2$ quantum dotsand their application as bioimaging probes, J. Mater. Chem., 22, 10609, 2012.

[36] X. S. Tang, W. B. A. Ho and J. M. Xue, Synthesis of Zn-Doped $AgInS_2$ Nanocrystals and Their Fluorescence Properties, J. Phys. Chem. C, 116, 9769, 2012.

[37] T. Sasamura, K. Okazaki, A. Kudo, S. Kuwabata and T. Torimoto, Photosensitization of ZnO rod electrodes with $AgInS_2$ nanoparticles and ZnS-$AgInS_2$solid solution nanoparticles for solar cell applications, RSC Advances, 2, 552, 2012.

[38] M. J. Deng, S. L. Shen, X. W. Wang, Y. J. Zhang, H. R. Xu, T. Zhang and Q. B. Wang, Controlled synthesis of QgInS2 nanocrystals and their application in organic-inorganic phtotodetectors, CrystEngComm, 15, 6443, 2013.

[39] A. Guchhait and A. J. Pal, Copper-diffused AgInS2 ternary nanocrystals in hybrid bulk-heterojunction solar cells: near infrared active photovoltaics. ACS Appl. Mater. Interfaces, 5, 4181, 2013.

[40] P. Guyot-Sionnest, E. Lhuillier and H. Liu, A mirage study of CdSe colloidal quantum dot films, Urbach tail, and surface states, J. Chem. Phys., 137, 154704, 2012.

[41] J. Krustok, J. Raudoja, M. Krunks, H. Mandar and H. Collan, Nature of the native deep localised defect recombination centers in the chalcopyrite and orthorhombic AgInS2, J. Appl. Phys., 88, 205, 2000.

[42] M. Powalla, M. Cemernjak, J. Eberhardt, F. Kessler, R. Kniese, H. D. Mohring and B. Dimmler, Sol. Energy Mater. Sol. Cells, 90, 3158, 2006.

[43] V. Probst, J. Palm, S. Visbeck, T. Niesen, R. Tolle, A. Lerchenberger, M. Wendl, H. Vogt, H. Calwer, W. Stetter and F. Karg, Sol. Energy Mater. Sol. Cells, 90, 3115, 2006.

[44] P. K. Santra, P. V. Nair, K. G. Thomas and P. V. Kamat, $CuInS_2$-Sensitized Quantum Dot Solar Cell. electrophoretic deposition, excited-state dynamics, and photovoltaic performance, J. Phys. Chem. Lett., 4, 722, 2013.

[45] S. Siebentritt, L. Gütay, D. Regesch,Y. Aida, V. Depredurand, Sol. Energy Mater. Sol. Cells, 119, 18, 2013.

[46] Pan, Z. X.; Zhang, H.; Cheng, K.; Hou, Y. M.; Hua, J. L.; Zhong, X. H.,highly efficient inverted type-I CdS/CdSe core/shell structure qd-sensitized solar cells, Acs Nano, 6, 3982, 2012.

[47] G. Niu, L. Wang, R. Gao, B. Ma, H. Dong and Y. Qiu, J. Mater. Chem., 22, 16914, 2012.

[48] S. R. Raga, E. M. Barea and F. Fabregat-Santiago, Analysis of the origin of open circuit voltage in dye solar cells, J. Phys. Chem. Lett., 3, 1629, 2012.

[49] G. Li, M. Liang, H. Wang, Z. Sun, L. N. Wang, Z. H. Wang and S. Xue, Significant enhancement of open-circuit voltage in indoline-based dye-sensitized solar cells via retarding charge recombination, Chem. Mater., 25, 1713, 2013.

[50] P. K. Santra and P. V. Kamat, Mn-doped quantum dot sensitized solar cells: a strategy to boost efficiency over 5%, J. Am. Chem. Soc., 134, 2508, 2012.

[51] S. Buhbut, S. Itzhakov, I. Hod, D. Oron and A. Zaban, Photoinduced dipoles: A new method to convert photons to photovoltage in quantum dot sensitized solar cells, Nano Lett., 13, 4456, 2013.

[52] H. McDaniel, N. Fuke, N. S. Makarov, J. M. Pietryga and V. I. Klimov Nature Communications 4, 2887, 2013.

[53] Y.-L. Lee, C. -H. Chang, Journal of Power Sources 185, 584–588, 2008.

[54] A. Guerrero, S. Loser, G. Garcia-Belmonte, C.J. Brus, J. Smith, H. Miyauchi, S. I. Stupp, J. Bisquert, T. J. Marks. Solution-processed small molecule: fullerene bulk-heterojunction solar cells: impedance spectroscopy deduced bulk and interfacial limits to fill-factors, Phys. Chem. Chem. Phys., 2013, 15, 16456, 2013.

Chapter 6

Investigation towards an Effective Size Window for Impact Ionization in PbS Quantum Dots

I. Introduction

As explained in the introduction ***Chapter 1***, currently there is huge need to fabricate highly efficient and affordable nanophotovoltaic devices. Many research groups are trying to address these issues using nanomaterials. Multiple Exciton Generation (MEG) or Carrier Multiplication (CM) is one among many such directions where energy on absorbed photon ($h\nu$) is at least more than twice the lowest energy gap (E_g) inside a semiconductor quantum dot (QD). Thus MEG or CM is a process of producing more than one electron-hole pairs as a result of single photon absorption[1] and thereby it has the potential to enhance the quantum yield above 100%. MEG has attracted great scientific interests as the process has strong caliber to enhance the power conversion efficiency beyond the maximum attainable thermodynamic efficiency[2] of a single junction solar cells. It was also predicted earlier that CM or MEG[3,4] can be very efficient in these quantum confined structures of semiconductors if these additional e-h pairs generated

per absorbed photon can be harvested inside cell. The reason for expecting higher probability of MEG in QDs is due to presence of stronger carrier-carrier interaction and lack of well-defined translational momentum in spatially localized quantum-confined levels[5]. Consequently, one expects that fabrication of solar cells using these QDs may be able to exploit CM to increase efficiency to further reduce average price per watt in solar cells. Efficient MEG/CM process in many semiconductor QDs were subsequently reported by several groups[6,7]. However, some recent experimental results and theoretical analyses generated further controversies about the precise nature of the physics of such CM processes in semiconductor QDs as compared to their bulk counterparts[8,9,10,11].

In solids, attractive coulomb interaction can produce bound states of electron-hole pairs called excitons during optical absorptions as discussed in ***Chapter 1***. Most spectral studies of QDs were focused primarily on the lowest excitonic transitions where one can comfortably neglect the presence of strong dispersions in dielectric response[12-15]. Here, we report collisional broadening of excitonic resonance in lead sulfide (PbS) QDs in room temperature optical absorption spectra at excitation energies (≥ 5.9 eV) much higher than its bulk band gap (~0.4 eV). Statistical description of these highly energetic photo-generated carriers maintains an effective temperature $T_{Hot\ Carrier}$ higher than the equilibrium temperature $T_{Lattice}$ of the material; thereby we call these 'hot' excitons. However, femto second time domain studies at such photo-excitation wavelengths (~210 nm) are not very commonplace and currently out of scope for this work. As an alternative, we have investigated absorption spectra of these PbS QDs over a wide range sizes starting from large particles with bulk like band structure to strongly confined particles of very small sizes with discrete density of states. It is also understood that breakdown of momentum conservation for excitons confined inside these QDs can allow such 'hot' excitonic states to have finite center-of-mass momentum $K = k_e + k_h$ and center-of-mass kinetic energy, where k_e and k_h are momentum of electrons and holes.

The absorption peak observed at energy ≥5.9 eV is known as E_3 critical points of PbS. This is due to electronic transitions (Σ_4 to Σ_7) around M_1 critical point and transitions (Δ_4 to Δ_6) around M_2 critical point[16]. Excitonic transitions around such saddle points in the electronic band structure are known as 'hyperbolic excitons' as the constant energy surfaces around these critical points in the joint density of states are hyperboloids. In connection with the observed E_3

excitonic resonance in PbS, we explore the following issues – (a) Is the classic definition of Bohr exciton radius (a_B) precise enough to describe transitions involving 'hot' excitons much above the fundamental band gap? (b) How to quantify the dispersive dielectric response in the coulomb interaction of electron-hole bound pair for hot excitons? (c) What are the implications of a dynamically screened effective Bohr radius for exciton-exciton scattering inside QDs? We will try to look forward to find answers to these questions on hot exciton physics throughout this chapter. Here, we will discuss the important role of collisional broadening of 'hot' excitons via 'zero phonon coupling' to the 'extended' band structure of PbS over wide range of sizes and measurement temperatures. In this context, we will elaborate how any empirical re-definition of the Bohr exciton radius may affect the mean free path of exciton-exciton collision and the basic understanding of MEG/CM. We will argue in favor of a minimum size cut-off or effective size window for MEG/CM as a result of significant reduction of collisional broadening in the strong confinement regime$\left(radius < \frac{1}{3} a_B \right)$[17], where the QDs can be quasi-ballistic for inverse Auger processes.

Unmistakably, such an effective size window for MEG/CM was not reported so far in earlier studies which were mostly focused on so called strongly confined very small QDs only. We will also discuss how the gradual size variations of these QDs from bulk like weakly confined particles to strongly quantum confined particles can affect the excitonic absorption spectra. We have also presented size dependence of the energy broadening and their corresponding blue shift of excitonic resonance as well as its overall aging and temperature variation to support our arguments. This will highlight the crucial roles of QDs sizes and importance of the Auger like non-phonon energy relaxation mechanisms manifested as collisional broadening in the physics of 'hot' excitons. MEG/CM is a direct consequences of hot-exciton physics and therefore, our results on the effects of excitonic collisions on absorbance spectra of PbS QDs, although observed at energies much above the visible range of solar spectrum, may help us in understanding the physics of MEG/CM for photovoltaic applications. Our analyses are further substantiated by somewhat similar temperature dependence and aging behavior in PbSe QDs too. Slight difference between PbSe and PbS originates only from the smaller excitonic binding energy and lesser band gap of PbSe as compared to PbS. This makes

excitons in PbSe to experience enhanced coulomb screening effects due to the presence of larger number of free carriers. Care has certainly been taken to ensure that observed results are not coming from any artifacts including capping ligands or any other chemical compounds like water, reagents etc. used in the synthesis.

II. Experimental Methods

a. Chemicals Used

Chemicals used in the wet chemical synthesis of PbS QDs are Lead Acetate $Pb(CH_3COO)_2$ and Sodium Sulfide (Na_2S). Thio-glycerol (3-Mercapto-propane-1,2 diol or TG) was used as capping agent. Deionized water (~18 MΩ/cm) was used as solvent. All chemicals were purchased from Sigma Aldrich and used without further purifications.

b. Synthesis Procedure

Synthesis is done in a two neck, round bottom flask with 18 MΩ/cm de-ionized water as solvent. 10 mL of 0.02 M Lead Acetate was initially heated to 80 $^{\circ}$C. Then another 10 mL of 0.02 M Sodium Sulfide and TG was added drop wise to hot lead acetate. The mixture was stirred continuously at 80°C for half an hour. Quantity of TG was varied during the reaction (from none for the uncapped sample to 120 μL in steps of 20 μL) to get a wide range of QDs sizes. After the reaction, particles were first washed with de-ionized water and then centrifuged for 10 minutes. This sequence of washing and purification was repeated for a total of 5 times. Finally, these are re-dispersed in de-ionized water for further optical characterizations. 20 μL of this final aqueous dispersion of PbS QDs is then mixed with 3 mL of de-ionized water inside a quartz cuvette for optical absorption studies.

III. Results and Discussions

a. Size Determination of QDs and Evidence of Excitonic Resonance In Optical Absorbance

The X-ray diffraction (XRD) spectra of PbS QDs establish crystalline nature of cubic structure of PbS as shown in figure 6.1. The 2θ peak positions at 26.0 °, 30.1 °, 43.1 °, and 51.1 ° can be indexed respectively to planes (111), (200), (220), and (311) of cubic rocksalt structure of PbS. All peaks from graphs are used to estimate the mean crystallite diameters using Debye-Scherrer method and we will refer this diameter as the size of these PbS crystallites throughout this report. Estimated mean crystallite sizes (diameters) are also mentioned in figure 6.1.

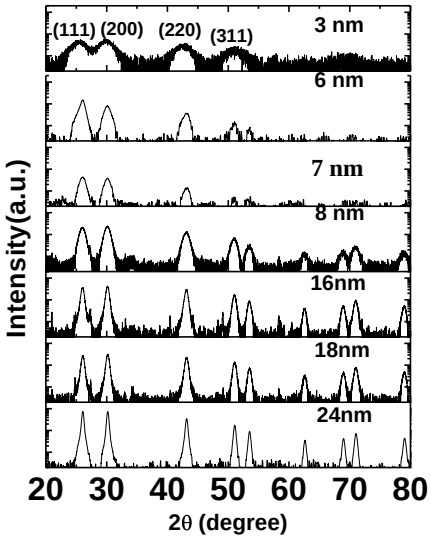

Figure 6.1. XRD spectra for different size TG capped PbS QDs.

Clearly the width of the Bragg peaks increases with decreasing crystallite sizes. We subsequently use these mean crystallite sizes in our study. Further analysis of the powder diffraction spectra using Williamson-Hall method showed very little strain (< 0.05%) in these crystallites, which substantiate the validity of our calculation based on Debye-Scherrer formula.

The room temperature optical absorption study of freshly prepared uncapped PbS QDs dispersed in de-ionized water is studied and given as figure 6.2. In the optical absorption spectra,

we see a strong resonance (~5.9 eV≈ $1.1\times E_3^{Bulk}$) just above E_3 critical points of bulk PbS[16,18] (E_3^{Bulk} = 5.3 eV) in this weakly confined[17] quasi-bulk PbS QDs with mean diameter ~24 nm. Absorption edges are also observed in this quasi–bulk sample near 3.5 eV and 2.1 eV which are slightly above the respective E_2 (3.14 eV) and E_1 (1.94 eV) critical point transitions of bulk PbS.

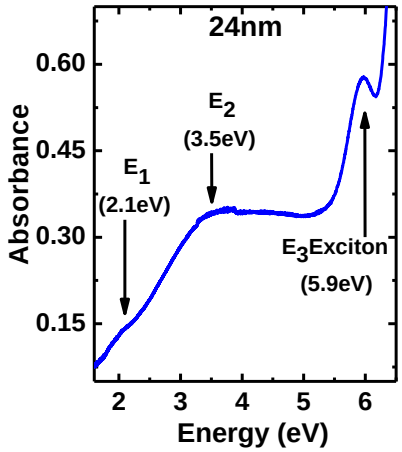

Figure 6.2. Room temperature optical absorption spectrum of freshly prepared un-capped PbS QDs.

Similar absorption spectra for the lowest E_0 transition is given as figure 6.3 for reference. Understandably, excitonic resonances around low energy critical points, such as E_0, in such small band gap material like PbS can easily be suppressed[16] by strong coulomb screening in presence of large numbers of charge carriers near the band edge. Although, existence of bulk/surface electronic defects can decrease free charge carrier density and thereby reduce the effect of such coulomb screening on excitonic resonances. It should be noted that similar excitonic resonances at energies much higher than the fundamental band gap was also reported in optical reflectivity studies of bulk PbS crystals at low temperatures[1718]. Moreover, as discussed above, momentum is not a good quantum number for strongly confined QDs[17], but the residual presence of bulk like extended band structure on the density of states of PbS QDs over the wide size range studied here is not fully unexpected in quasi bulk QDs. Such lingering effects of bulk band structure on the energy levels of semiconductor QDs were predicted[19] theoretically under the truncated crystal approximation too.

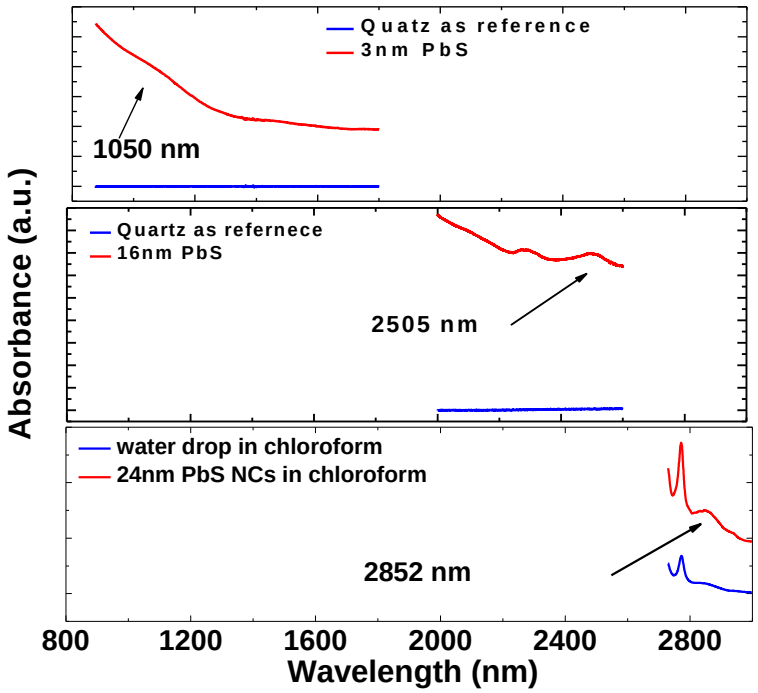

Figure 6.3. E_0 optical absorption transitions in different sized PbS QDs.

b. Size Variation and Blue Shift of E_3 Resonance

In figure 6.4, we compare the optical absorption spectra of uncapped and TG capped PbS QDs (having a_B ~ 18 nm) of various diameters. Absorbance peak of E_3 exciton resonance blue shifts and increases monotonically with decreasing QDs size (as shown in the inset of the figure 6.4), which indicate that oscillator strength for excitonic absorption is still size dependent in PbS QDs even under weak confinement $(radius \sim 3a_B)$[17]. The above enhancement of absorbance with decreasing size clearly says that the contribution from light scattering is not significant. Moreover, observed size dependence and blue shift also rules out the contamination due to TG ligands or any other floating molecular species other than solid PbS as the cause of this E_3 excitonic resonance. We see that E_3 spectrum of this weakly confined PbS QDs having 24nm crystallite diameter is gradually broadened into an absorption edge in ~16 nm PbS. Yet, below 16 nm, we observe progressive sharpening with decreasing size.

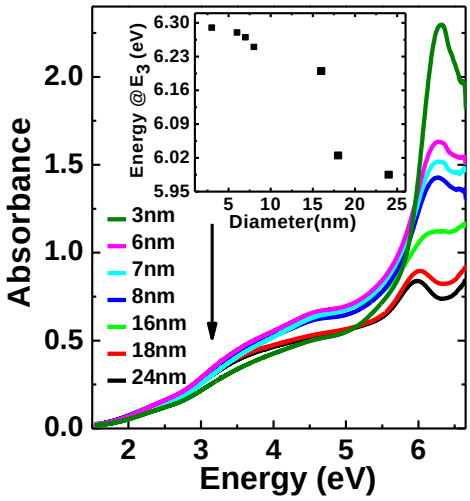

Figure 6.4.The variation of excitonic resonance with the size of PbS QDs. Molar concentrations of PbS were kept same for all particle sizes during the measurements except for 3 nm. There it was kept at 50% of the rest to avoid the saturation of optical absorption. The inset shows change in E3 energy w.r.t. size of QDs.

Further understanding of this unusual evolution of excitonic broadening with crystallite size will be presented near the end of Section III D and in the beginning of Section III E. These spectra are fitted with Voigt line shapes from which we estimate both inhomogeneous width (Gaussian) and homogenous width (Lorentzian) of the E_3 resonance. Lorentzian widths are nearly ~ 1.5 times the respective Gaussian widths for particles ≥16 nm. In general, magnitude of excitonic transition is inversely proportional to its broadening parameter. Nevertheless, inhomogeneous width of E_3 exciton is not monotonically decreasing with size (figure 6.5). Nominal use of Heisenberg uncertainty relation $\Delta E\,\Delta t \sim \hbar$ with homogeneous broadening (ΔE) estimates the life time (Δt) of such states around femto-seconds domain.

Moreover, the magnitude of maximum possible energy broadening width ΔE_{max} = $[\Delta E(R_{Min}) - \Delta E(R_{Max})]$ is calculated using $\Delta E = \frac{h^2}{8R^2}\left[\frac{1}{m_e^*}+\frac{1}{m_h^*}\right] - \frac{1.8e^2}{4\pi\varepsilon R}$, where ΔE_{max} is difference between the energy position for minimum ($R=R_{min}$) and maximum ($R=R_{max}$) QDs radius, R=D/2 is the radius of the crystallite as estimated by XRD, h is the Planck constant, e electronic charge, ε is the static dielectric constant, m_e^*, m_h^* are the effective mass of electron and hole.

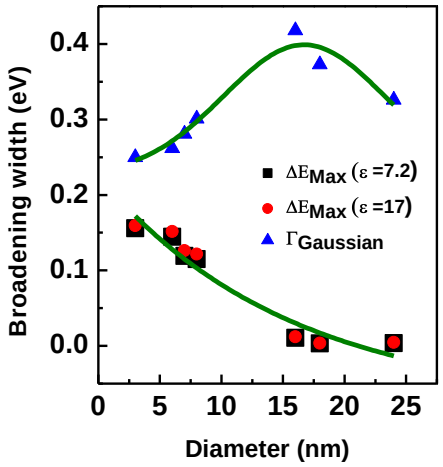

Figure 6.5. De-convoluted Gaussian component of the E_3 excitonic line width has a maximum around 16nm. Maximum possible energy broadening (ΔE_{max}) due to the size distribution is much smaller than both the estimated inhomogeneous line widths for all sizes.

These ΔE_{max} values (figure 6.5) are well below the estimated line widths of E_3 resonances and have qualitatively different size dependence for all QDs diameters. Therefore, we can rule out any size distribution effect towards energy broadening of E_3 exciton. Surprisingly, excitonic transitions (figure 6.6) are much above the E_3 critical point of bulk PbS (0.6 eV larger than 5.3 eV) and also larger than its optical phonon energy ~20-27 meV[12,20]. It should also be noted that 5.9 eV energy of E_3 excitonic resonance is still $< 2 \times E_3^{Bulk}$ at 5.3 eV to observe such hot excitonic effects around the E_3 critical point. Although the energy of E_3 excitonic resonance at 5.9 eV may be well within the energy continuum of states above the lowest fundamental E_0 bandgap of PbS but it is certainly not the case for excitons localized around the much larger E_3 gap[16,18,19]. Nonetheless, estimates (using $\mu \approx 0.05\ m_e^0$, m_e^0 is the free electron mass) also shows that this excess energy cannot be explained only by confinement induced enhancement of energy $\Delta E_{Confinement} = \frac{h^2}{8R^2}\left[\frac{1}{m_e^*} + \frac{1}{m_h^*}\right]$ except for strongly confined PbS QDs of mean diameter $\leq$ 3 nm (figure 6.6). Notably, no single power law behavior can describe the variation for all sizes. So it is tempting to attribute this energy difference to – a) failure of effective mass theory[21,22] at smaller sizes, b) non-parabolicity[23] of the band structure at high energies. However, size

dependence of excitonic energy is much slower than $\sim \frac{1}{R^2}$ *or* $\frac{1}{R}$ type of behavior (figure 6.6). Therefore, this extra energy may be credited to excess center-of-mass kinetic energy ($\hbar^2K^2/2M$) of E_3 exciton as a result of non-conservation of momentum inside QDs, where M is the translational mass of exciton ($M = m_e^* + m_h^*$) as mentioned in the introduction.

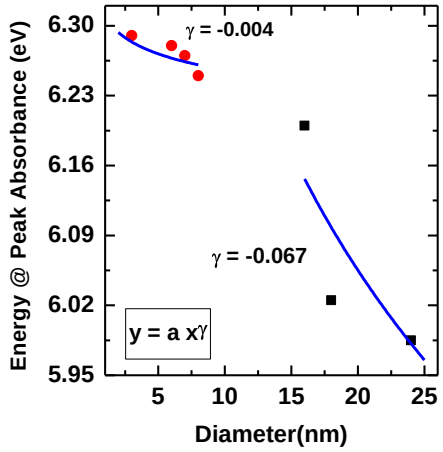

Figure 6.6. Monotonic blue shifts of E_3 excitonic resonance (5.3 eV + ΔE) with decreasing mean crystallite diameter of PbS QDs. Notably, no single power law behavior can describe the variation for all sizes.

c. Dispersion of Dielectric Response at Energies Much Higher Than the Band Gap and the Concept of Effective Bohr Exciton Radius

Generally, high frequency optical dielectric constant[16] of PbS as $\varepsilon = \varepsilon_e + \varepsilon_l = \varepsilon_e(0) \cong \varepsilon_\infty \sim 17$ is used to estimate excitonic parameters, where the subscripts 'e' and 'l' stands for electronic and lattice contributions respectively. Approximating dielectric response with a limiting value like $\varepsilon_e(0) \sim \varepsilon_\infty$ is only valid for $\frac{E_g}{\hbar} >> \omega >> \omega_T$, where E_g is the band gap and ω_T is the frequency of transverse optical phonon[16]. Yet, here we have $\omega_{E_3\ \mathbf{Exciton}} >> \frac{E_3^{Bulk}}{\hbar} >> \frac{E_0^{Bulk}}{\hbar}$. So, the standard dielectric response[24] theory based on 'electro-statics' may not be adequate here. Experimentally, this ε_∞ is estimated from the $E \rightarrow 0$ limit (called the long wavelength limit) of the measured real part of the dielectric constant assuming that the imaginary part (absorbance) more or less

vanishes in that limit. However, in the presence of strong resonant optical absorption as significant contribution from imaginary part of the dielectric response, we have used empirical magnitude of 7.2 for complex $\varepsilon(\omega)$ around 5.9 eV of E_3 excitonic resonance. This value of $|\varepsilon(\omega)|$ is estimated from the reported spectroscopic ellipsometry measurements on crystalline bulk PbS[25]. One can certainly measure $|\varepsilon(\omega)|$ of these QDs to get a better estimate, which is currently beyond the scope for wavelengths ≤ 210 nm. We have found that calculated exciton binding energy $|E_{EX}| = \left| -\frac{1.8e^2}{4\pi\varepsilon R} \right|$ using $|\varepsilon(\omega)| = 7.2$ are higher than that with ε_∞=17 and much larger than optical phonon energy of PbS for all sizes. Reader can see the quantitative details of this variation of excitonic binding energy with size in the Table 6.1.

This can certainly explain the existence of E_3 excitonic resonance in PbS QDs even at room temperature. Assuming that we can still apply the hydrogenic model for exciton physics at such energies, we approximate an *effective Bohr exciton radius (a^*_{Ex}) = 7.6 nm* assuming $|\varepsilon(\omega)| = 7.2$ at E ~5.9 eV, $\mu \approx 0.05\ m_e^0$. Here we assume that an empirical dielectric response in terms of $\varepsilon(\omega)$ can be defined even for the smallest QDs without any additional size dependence and surface polarization effects. This effective Bohr exciton radius (a^*_{Ex})= 7.6 nm also shows that quasi-bulk like uncapped particles with crystallite radius (diameter) of 12 nm (24 nm) can still be treated in the weak confinement regime (radius ~$3a_B$)[17]. This value of $|\varepsilon(\omega)|$ is much larger around E_2 , E_1 , E_0 critical points of PbS[25]. Therefore, binding energy of any excitons around E_2, E_1, E_0 critical points can be much smaller than the binding energy hot excitonic resonance at E_3 critical point. This certainly explains reason for not so significant presence of excitonic resonance at low energy critical points as the presence of effectively large coulomb screening effects[16] as also explained in Section III A.

Table 6.1 Calculated exciton binding energy for PbS QDs using formula $\left|E_{EX}\right| = \left|-\frac{1.8e^2}{4\pi\varepsilon R}\right|$ and ε = 17 and ε = 7.2 respectively.

Samples ; Nano-Crystallite Diameter (nm)	**$\|E_{EX}\|$ (eV) assuming ε_∞ = 17**	**$\|E_{EX}\|$ (eV) assuming $\|\varepsilon\|$ = 7.2**
NO TG PbS ; 24 nm	0.013	0.030
20 TG PbS ; 18 nm	0.017	0.040
40 TG PbS ; 16 nm	0.020	0.045
60 TG PbS ; 8 nm	0.038	0.090
80 TG PbS ; 7 nm	0.044	0.103
100 TG PbS ; 6 nm	0.051	0.120
120 TG PbS ; 3 nm	0.102	0.240

d. Absence of Temperature Variation of Excitonic Resonance Even In Weakly Confined QDs and the Significance of Non-Phonon Energy Relaxations.

Strong coupling of excitons to optical phonons is usually neglected in lead salts because of quasi symmetrical nature of electron and hole bands near its fundamental band gap (E_0). However, electronic band structure near E_3 critical point in PbS is definitely not symmetric ($m_e^* \neq m_h^* \sim E_3$) [16,26]. So, we rather expect the broadening of E_3 exciton to be dominated by Fröhlich type strong polar exciton-phonon interactions[27]. Despite of this, E_3 resonance still survives at room temperature and, most importantly, shows temperature independent shift of excitonic peak (figure 6.7) even for weakly confined (~24 nm) particles. Therefore, it seems likely that '*non-phonon'* energy relaxation mechanisms [27] like inverse Auger processes may be dominating over phonons for this highly energetic E_3 exciton. Further evidences of this assertion come from temperature dependent evolution of excitonic spectra (figure 6.7a) of bigger QDs, which can be ascribed to Auger cooling effects. This assertion is further vindicated by total absence of such

temperature dependence of absorption spectra in smaller QDs (figure 6.7c) which show no signs of agglomeration with time (figure 6.9c) due to their charged nature unlike the bigger ones (figure 6.9a). More details of this aging behavior can be found in Section III F. Extended band structures of a solid are crucial for inverse Auger processes[28-30]. This 'hot' E_3 exciton can easily avail a large number of final density of states required for efficient impact ionization via confinement induced 'zero phonon coupling' to other parts of the PbS band structure in bigger QDs[8,9]. This leads to progressive enhancement of spectral broadening of larger (≥ 16 nm) crystallites with decreasing size. Currently, probing any CM of this 'hot' E_3 exciton with time domain spectroscopy is beyond the scope due to scarcity of suitable deep-UV pulsed lasers at wavelengths ≤ 210 nm. Typically, collisional broadening results in homogeneously broadened line shapes for gas molecules. However, presence of significant inhomogeneous broadening due to anisotropic exciton-exciton collisions can be explained by size confinement induced momentum uncertainty which connects E_3 excitons to different symmetry points in the PbS band structure and a distribution in excitonic K space for such hot excitons.

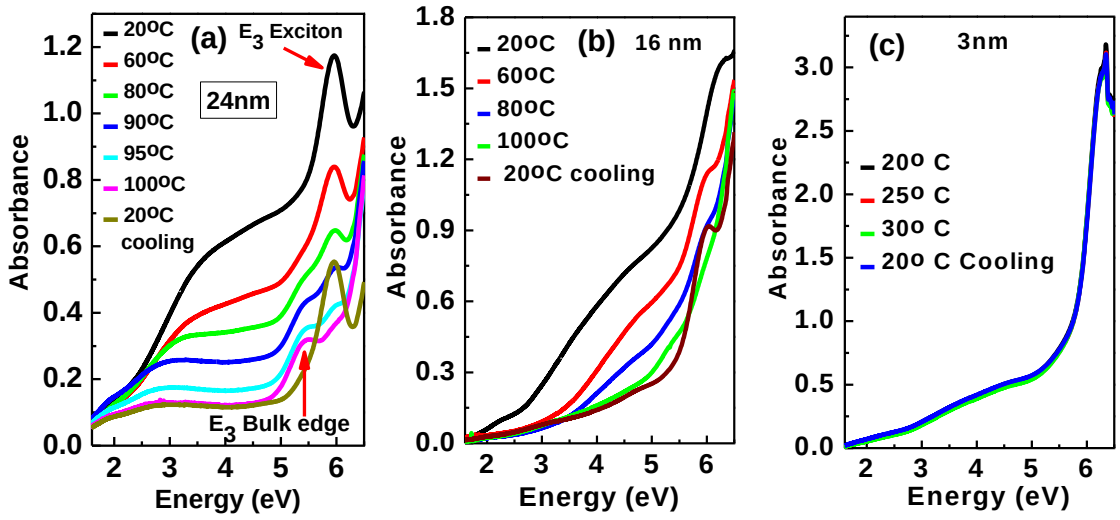

Figure 6.7. (a) Temperature variation of uncapped PbS QDs with mean diameter of 24 nm. (b) Almost similar but less pronounced spectral changes with temperature are also observed for 16 nm PbS during cooling stages. (c) 3 nm PbS shows relative less temperature dependence upto 30 °C.

e. Mean Free Path of Excitonic Collisions and Effective Size Window For Efficient Multi-Excitonic Effects.

Unlike monotonic size variation of the rates of inverse Auger type processes in smaller QDs[31-32], spectral broadening of E_3 exciton (figure 6.2 and 6.5) goes through a maximum around intermediate confinement range. This observation can only be explained if impact ionization and subsequent collisional broadening of E_3 exciton have a minimum size cut off. Moreover, it was predicted that exciton-exciton scattering[33] and impact ionization[34,35] are one of the main causes of carrier multiplication in semiconductor QDs. However, impact ionization can be suppressed in very small structures due to the presence of quasi ballistic transport[36]. This usually happens when the size (diameter) becomes smaller than the inverse Auger mean free path (λ) of exciton-exciton scattering[37]. Estimate based on such models[37] yields $\lambda \sim \left(\frac{\pi^2 M E_{Ex}}{24\mu k_B T}\right)^{0.1} \left(\sqrt{3}\right) a^*_{Ex} \sim 1.93 a^*_{Ex} \cong 15nm$

where D=2R~16 nm, M $\approx$ 0.21 m_e^0, $\mu \approx 0.05 m_e^0$, a^*_{Ex}=7.6 nm around E_3, k_B is Boltzmann constant, T is temperature in Kelvin and E_{Ex}~1/R is the binding energy of E_3 exciton. The values of mean free path of exciton-exciton scattering for different sized QDs are given in the plot 6.8. Interestingly, λ for 16nm PbS is comparable - (i) to the QDs diameter at the transition point of both excitonic broadening (figure 6.5) and (ii) blue shift (figure 6.6) and (iii) the effective Bohr exciton diameter (~15.2 nm) at E_3 resonance. Use of ε_∞ = 17 produces λ >30 nm and one hardly expects any PbS QDs having diameters < 30 nm to undergo MEG/CM in direct contradiction to all experimental reports. However, if we invoke dynamic screening of coulomb interaction[38,39] and $|\varepsilon(\omega)|$ = 7.2 is used, then possibility of collisional broadening of E_3 exciton within a reasonable *'size window'* of operation is restored inside weak-to-intermediate confinement regimes. This clearly resonates with the theoretical statement that strong confinement may not be exclusively needed for efficient CM[19]. Hence we seriously need to re-examine standard excitonic terminologies to understand the physics of carrier multiplication of such 'hot' excitons[38,39] – a) having high center-of-mass velocity and b) created inside a region of dispersive dielectric response which can deviate considerably from its usual high frequency limit of ε_∞. It had also been clearly emphasized[39] that commonplace excitonic parameters like Bohr radius, exciton binding energy can become *"imprecise and ambiguous"* within the framework of Bethe-Salpeter equation which automatically accounts for such dynamical screening. We must however note

that, this expression of λ is calculated for symmetric S-states only and may need revision in some cases.

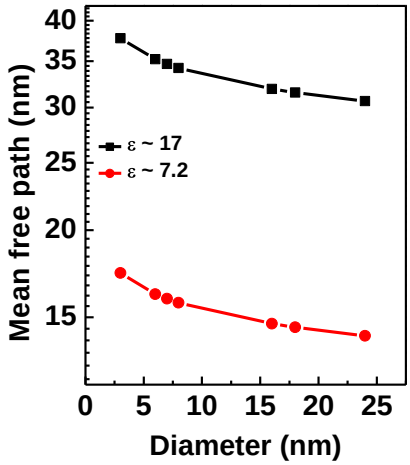

Figure 6.8. This plot demonstrates the comparison of exciton mean free path values calculated using ε = 17 and ε = 7. In case of ε =17, the calculated mean free path for exciton-exciton scattering event is >30 nm. In that case, any significant impact ionization is not possible in any of the PbS QDs under our investigation due their relative small sizes < 24 nm.

f. Role of Dielectric Confinement in the Aging of Absorbance Spectra and the Observed Suppression of Aging in Smaller QDs.

To get further insights into E_3 resonance, aqueous dispersion of PbS QDs of different sizes are deliberately allowed to age and observed variation in optical absorbance are plotted in figure 6.9. We see that, room temperature E_3 excitonic spectra sharpen up with aging (figure 6.9a and 6.9b) in bigger QDs. To understand, we briefly focus on the structural development of these QDs during aging. Hydrodynamic size of uncapped PbS was already very large (>2 micron) compared to its mean QDs diameter of 24 nm. The hydrodynamic size of fresh QDs with diameter of 16 nm was ~30 nm, which gradually increases to around a micron due to aging. However, XRD indicates (figure 6.10) that QDs size hardly increases during aging, which excludes – (a) significant Ostwald ripening, (b) growth of PbS QDs by incorporation[40] of sulfur atoms from thiol based ligands. We understand this increase of hydrodynamic size can come from agglomeration of PbS QDs which incidentally affect dielectric confinement[41] of these

excitons. Overall decrease in absorbance (in spectral range < 5 eV) of QDs can be explained by steady delocalization of excitonic wave function into surrounding material by increased agglomeration and subsequent decrease of oscillator strength.

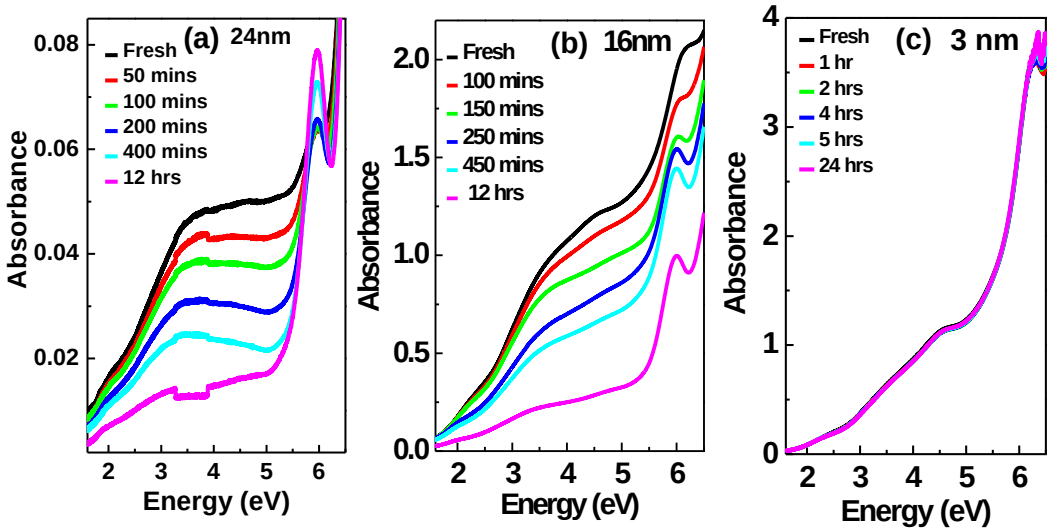

Figure 6.9. Aqueous dispersion of PbS QDs were not sonicated and deliberately allowed to age in order to get better physical insights of the spectral origin of E_3 exciton. (a) Variation of absorbance of E_3 exciton is characteristically opposite to the portion of the spectra at photon energies lower than 5 eV for uncapped PbS QDs with mean diameter of 24 nm. The abrupt changes between 3 eV to 4 eV are due to instrumental artifacts for lamp changes etc at small absorbance. (b) We see qualitatively similar kind of sharpening of E_3 excitonic peak with aging for 16nm PbS. (c) strongly confined PbS nanoparticle with mean diameter 3 nm shows hardly any change with aging as compared to that of 6.9a and 6.9b.

Nonetheless, E_3 excitonic resonance is progressively enhanced and sharpened with aging! Spatial delocalization of excitons can reduce confinement induced momentum uncertainty which further reduce the availability of final states within the extended band structure of PbS. Hence, probability of exciton-exciton scattering and collisional broadening of E_3 exciton also comes down with time. Here we must point out that even for the biggest PbS QDs with mean radius 12nm (figure 6.2), the spatial extent is well within the weak[17] confinement region $\left(\text{radius} \sim 3a_B \right) < a_{Ex}^{*} = 7.6\text{nm}$ for all these quantum effects to influence the excitonic delocalization. Additional defect formation or incorporation of water[42] into the QDs cannot explain such systematic but seemingly opposite aging dependence of – (a) the E_3 excitonic resonance and (b) the absorption spectra in lower energy ranges. Similar effect, although less

pronounced, is observed in 16 nm PbS (figure 6.9b). Here E_3 exciton showed initial red shifts, during aging induced gradual lessening of dielectric confinement, which was absent in larger uncapped samples due to its quasi-bulk nature. Unlike 16 nm PbS, hydrodynamic diameter and absorbance of smaller 3 nm PbS are hardly changing with time (figure 6.9c) This can only happen if these smaller QDs are intrinsically charged as compared to the bigger ones. Mutual coulomb repulsion of charged QDs can prevent agglomeration, sustain the dielectric environment of 3 nm PbS and safeguard the absorbance from aging effect.

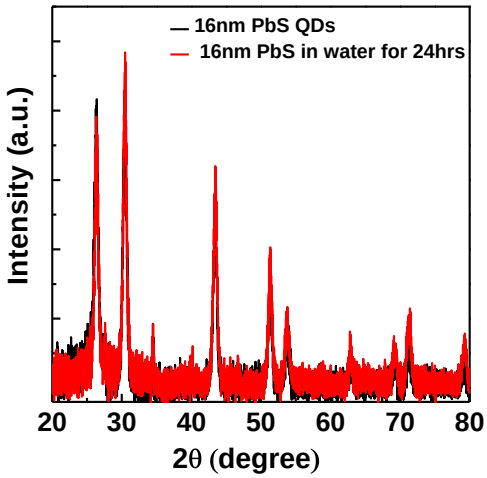

Figure 6.10. XRD spectra for 16nm PbS QDs. One spectrum is recorded on freshly prepared QDs and for other spectra sample is intentionally kept in water for 24 hrs. Drop casted thin films of each sample are used for measurements. It shows that aging doesn't changes crystallite size of ~16 nm PbS QDs. So, all changes observed in UV-VIS absorption (figure 6.9b) of 16 nm PbS aging are due to agglomeration of QDs and not due to Ostwald kind of growth of these QDs.

g. Suppression of Auger Cooling in Smaller QDs

As the E_3 resonance ~ 5.9 eV is fading out with increasing temperature from 20 $^{\circ}$C to 100°C for uncapped quasi-bulk PbS (figure 6.9 a), another peak slowly emerges ~5.3 eV at its expense. Interestingly, 5.3 eV is also the bulk E_3 critical point of PbS! We see no gradual energy shift of the E_3 resonance with increasing temperature but rather a coexistence of E_3 resonance and the bulk like feature from 80 $^{\circ}$C to 95 $^{\circ}$C. Above that temperature, E_3 resonance vanishes altogether. However, we again retrieve this E_3 resonance once temperature is reduced back to 20

°C, except for some aging induced reduction in absorbance and sharpening of the E_3 peak as discussed in the previous section. PbS has a positive temperature coefficient of band gap except under strong confinement regime where excitonic energy hardly[13] varied with temperature. However, we cannot use the same reasoning to explain current observations for this weakly confined quasi-bulk PbS! With increasing phonon scattering and decreasing $\Delta T = (T_{Hot\ Carrier} - T_{Lattice})$ above room temperature, this E_3 exciton has much less access to other parts of PbS band structure for efficient impact ionization. Therefore, emergence of bulk like spectral feature ~5.3 eV with increasing temperature represent Auger cooling[43,44] of energetic 'hot' E_3 excitons to its bulk E_3 band edge by transferring its excess energy mostly to heavier holes ($m_e^* \neq m_h^*$ at E_3)[19]. Prominence of bulk E_3 band edge steadily decrease with decreasing size because of stronger size confinement and consequently lesser density of available ground states at smaller sizes (figure 6.7b). Observed agglomeration (figure 6.7a and 6.7b) of these bigger QDs ($D \geq 16$ nm) also indicates their non-charged nature which may have prevented the suppression of Auger cooling seen in smaller charged QDs[45] (figure 6.7c and 6.9c). QDs diameter also remains same (figure 6.10) which confirms the absence of significant irreversible changes like oxide/defect formation in this range of temperatures. Especially, line width broadening of E_3 exciton with decreasing size and with increasing temperature are qualitatively different. In fact, the temperature coefficient of impact ionization (TC_{II}) depends on its threshold energy (E_i) and the mean free path (λ) of exciton scattering as[46] $TC_{II} = \frac{E_i}{q\varepsilon\lambda}\left[\frac{d\lambda}{\lambda dT} - \frac{dE_i}{E_i dT}\right]$. Spectra of 3nm PbS QDs follows the literature[47] for annealing temperatures >40 °C, where it undergoes Ostwald ripening and we also see that hydrodynamic size of these particles increases to >275 nm. However, the E_3 resonance did not change till 30 °C. This apparent temperature independence of excitonic line width for strongly confined PbS can be ascribed to a set of reasons like – (a) reduction of impact ionization due to charged nature of these strongly confined particles, (b) vanishing of TC_{II} due to mutual cancellation of the above two terms, (c) reduction of collisional broadening and Auger cooling in the ballistic regime, (d) strong surface effects etc. Size dependence of photo-charging[48,49] and/or photo-induced surface trapping[50,51] are currently being investigated.

Recently, it was argued that higher energy excitonic states are bulk like where Bohr exciton radius (a_B) can approach to 'zero' value due to the divergence of effective mass[52]. However, such 'arithmetical' divergence of effective mass happens $(d^2E_{C,V}/dk^2 = 0)$ away from E_3 like critical points $(\nabla_k (E_C - E_V) = 0)$. It is also evident that charged particles with smaller effective masses are easy to accelerate and classical mechanical treatment of effective mass approximation no longer holds where $m^*_{e,h} = \pm\hbar^2 / (d^2E_{C,V}/dk^2)$ starts to diverge[53].

IV. Control Experiments

In order to understand the obtained results and to rule out any artifacts from temperature dependent and time dependent measurements we have done some control experiment. The results for these control experiments will further give insight into the presented conclusions.

a. Aging of Lead Acetate

Figure 6.11 shows aging of aqueous lead acetate with different time interval. Spectrum has taken by dissolving lead acetate in water with water as reference. Peak feature at 5.9 eV degrades in intensity with time which is just opposite to behavior for uncapped PbS QDs. It shows the feature observed in aging of uncapped PbS QDs (6.9a) is not coming from presence of unused lead acetate in the final product of PbS QDs.

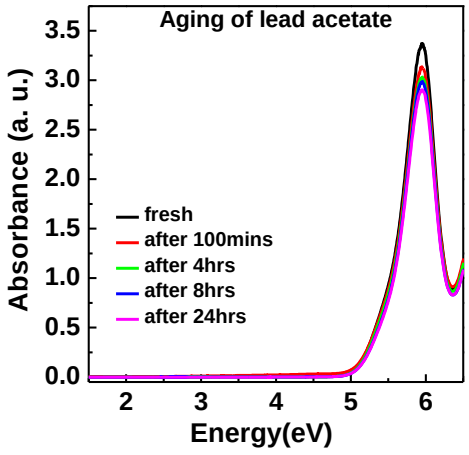

Figure 6.11. Aging of lead acetate at different time interval.

b. Lead Acetate Absorption Spectra at Different Temperature

Figure 6.12 shows effect of temperature on absorption spectra of aqueous lead acetate solution. Spectra are taken by dissolving lead acetate in water with water as reference. With increasing temperature absorption peak at 5.9 eV fades out and peak at 5.4 eV start appearing, but lowering temperature back to 20 °C shows peak at 5.9 eV with no signature at 5.4 eV. This behavior is similar to the uncapped PbS QDs. Similar spectral behavior and temperature dependence (with figure 6.9b) just indicates that the molecular orbitals of E_3 band structure may be generically related with atomic orbitals of lead in lead compounds. However, we will clearly demonstrate in the next section that the E_3 resonance (Fig 6.2 and 6.4) is not coming from the leftover Lead Acetate precursors. Moreover, we will also show in the next section that our washing and purification sequence remove all such leftover reagents.

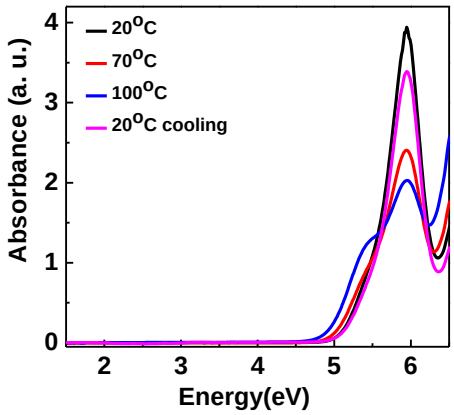

Figure 6.12. Absorption spectra for lead acetate at different temperature.

IV) Control experiments to Rule out Presence of Artifacts and Unused Chemicals or Ligands in the Optical Measurements of E_3 Transition.

a. Water Absorption Spectrum

Figure 6.13 shows absorption Spectra of DI water with DI water as reference. No trace of PbS like E_3 peak found around 5.9 eV.This also indicates that reported E_3 transition of PbS are

not due to any instrumental artifact or defects in cuvette or from water itself. So it indicates that reported E_3 transition of PbS are not due to any instrumental artifact or defects in cuvette.

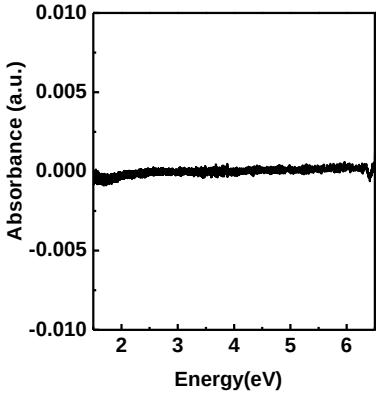

Figure 6.13. Absorption spectra for water with water as reference.

b. Absorption Spectra of Thioglycerol Capping Agent

Figure 6.14 shows absorption spectra of Thio-glycerol solution in de-ionized water with deionized water as reference. It shows no resonance transition around 5.9 eV. Also the absorption spectra for 24 nm uncapped QDs presented in the paper (Figure 6.2, 6.7a and 6.9a) have no thioglycerol in it. Therefore, the E_3 transition for PbS QDs (reported in manuscript) cannot be from any unused Thio-glycerol (i.e. ligand) present in solution.

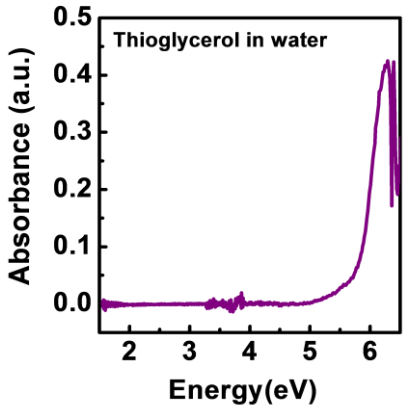

Figure 6.14. Absorption spectra for Thioglycerol with water as reference.

c. Absorption Spectra of Sodium Sulfide

Figure 6.15 shows absorbance of aqueous Sodium sulfide with deionized water as reference. It shows absorption at 5.37 eV, indicating that E_3 resonant absorbance of PbS QDs (> 5.9 eV) is not due to presence of unused sodium sulfide in the aqueous dispersion of PbS nanoparticle used in optical absorption experiments.

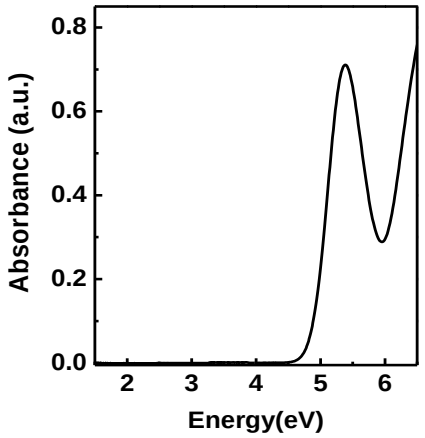

Figure 6.15. Absorption spectra for Sodium Sulfide with water as reference.

d. E_3 Resonance is Not Coming From Unused or Left Over Lead Acetate

Figure 6.16 shows absorbance spectra for mercapto-succinic acid capped CdTe QDs and CdTe + additional Lead acetate solution, washed for 5 times. Here we have done the same experiment with CdTe QDs which has no E_3 like resonant peak to beginning with. We added aqueous lead acetate solution (20 micro-liter of 0.02 M lead acetate in 3 ml of CdTe solution, this is the full amount we add during the chemical synthesis in aqueous dispersion of CdTe and then we washed it 5 time using centrifuge to prove that unused lead acetate won't persist the washing + purification sequence. Moreover, in case of PbS QDs, >99% of this 20 micro-liter of lead acetate is expected to be used up in making PbS and only a very small fraction will be left after the reaction with equal concentration of Na_2S. So the E_3 resonance peak is definitely not coming from unused Lead Acetate either. It evidence that E_3 excitonic resonance is not coming from any leftover chemical reagents as our washing and purification sequence removes it from the final aqueous dispersion of PbS QDs used in optical absorption experiments.

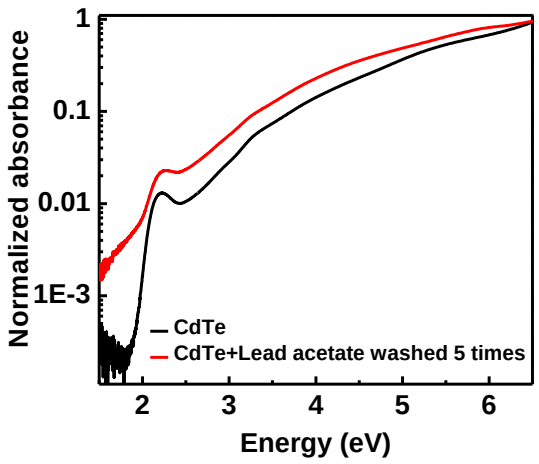

Figure 6.16. Absorption spectra for CdTe QDs and for CdTe QDs + lead acetate solution with water as reference.

V. Conclusions

In summary, dynamical Coulomb screening and the residual effect of extended band structure of PbS were sought to explain the dependence of E_3 excitonic resonance with aging and temperature over a wide range nanoparticle sizes from weakly confined quasi bulk to strongly confined very small QDs. We argue that Bohr radius of hot exciton is not material specific but photo-excitation specific[54]. This empirical notion of effective excitonic Bohr radius is a direct consequence of the dynamical screening of coulomb interactions at high photon energies which may eventually lead to better conceptual understanding of condensed matter physics of 'hot' excitons. Although it is not immediately clear whether one can use such a straight forward extension of hydrogenic atom model to understand the formation of excitons at such high enough energies. However, it is understandable that significant reduction of carrier multiplication in the ballistic limit could have influenced all past studies focused only on strongly confined quantum dots. As per our calculation in case of ε =17, the mean free path for exciton-exciton scattering event is >30 nm. In that case, any significant impact ionization is not possible in any of the PbS QDs under our investigation due their relative small sizes < 24 nm. However, if we use $|\varepsilon(\omega)|$ = 7.2, then possibility of collisional broadening of E_3 exciton within a reasonable *'size window'* of operation is restored inside weak-to-intermediate confinement regimes. Therefore, we predict an

intermediate *'size window'*, where impact ionization can dominate over other kinds of exciton relaxation pathways. Although, this current 6 eV excitonic resonance has no relevance for photovoltaics, but one can surely extend these analyses of hot exciton physics and even suggest size optimization of semiconductor QDs for better exploitation of carrier multiplications to improve the power conversion efficiency of nano-photovoltaics inside the solar spectrum. Recently, it has been brought to our notice that enhancement of internal quantum efficiency of PbSe quantum dots with increasing size is verified[55] in experiments. While determining the hydrodynamic sizes of the QDs using Dynamic Light Scattering we came across interesting results here we could find out the exact result for the observed smaller hydrodynamic size compare to the crystallite size. In the next ***Chpater 7,*** we have discussed these results in more detail using Fluorescence Correlation Spectroscopy.

VI. References

[1] A. J. Nozik, Multiple exciton generation in semiconductor quantum dots, Chem. Phys. Lett. 457, 3-11, 2008.

[2] W. Schockley and H. J. Queisser, Detailed Balance Limit of Efficiency of p-n Junction Solar Cells, J. Appl. Phys. 32 (3), 510, 1961.

[3] S. Kolodinski and J. Werner, Solar Energy. Mat. And Solar cells 33, 3, 275, 1994.

[4] A. J. Nozik, Quantum dot solar cell, Physica E 14, 115, 2002.

[5] G. N. Lazaro, A. Padilha, L. Levina, V. Sukhovatkin, S. Webster, L. Brzozowski, E. H. Sargent, D. J. Hagan and Eric W. Van Stryland, Size dependence of carrier dynamics and carrier multiplication in PbS quantum dots, Phys. Rev. B, 83, 155302, 2011.

[6] R. D. Schaller and V. I. Klimov Phys. Rev. Lett. 92, 186601, 2004 ; R. D. Schaller, M. Sykora, J. M. Pietryga and V. I. Klimov, Nano Lett. 6, 424, 2006.

[7] R. J. Ellingson, M.C. Beard, J. C., Johnson, P. Yu, O. I. Micic, A. J. Nozik, A. Shabaev and A. L. Efros, Highly Efficient Multiple Exciton Generation in Colloidal PbSe, Nano Lett. 5, 865, 2005.

[8] J. J. H. Pijpers, R. Ulbricht, K. J. Tielrooij, A. Osherov, Y. Golan, C. Deleure, G. Alla and, M. Bonn, Assessment of carrier-multiplication efficiency in bulk PbSe and PbS, Nature Phys. 5, 811, 2009.

[9] C. Deleure, G. Allan, J. J. H. Pijpers and M. Bonn, Carrier multiplication in bulk and nanocrystalline semiconductors: Mechanism, efficiency, and interest for solar cells Phys. Rev. B 81, 125306, 2010.

[10] G. Nair, S. M. Geyer, L.-Y. Chang and M. G. Bawendi, Carrier multiplication yields in PbS and PbSe nanocrystals measured by transient photoluminescence, Phys. Rev. B 78, 125325, 2008.

[11] G. Nair and M. G. Bawendi, Carrier multiplication yields of CdSe and CdTe nanocrystals by transient photoluminescence spectroscopy, Phys. Rev. B 76, 081304R, 2007.

[12] T. D. Krauss and F. W. Wise, Raman-scattering study of exciton-phonon coupling in PbS nanocrystals, Phys. Rev. B 55, 9860, 1997.

[13] A. Olkhovets, R. C. Hsu, A. Lipovskii, and F. W. Wise, Size-Dependent Temperature Variation of the Energy Gap in Lead-Salt Quantum Dots, Phys. Rev. Lett. 81, 3539, 1998.

[14] F. W. Wise, Lead Salt Quantum Dots: the Limit of Strong Quantum Confinement, Acc. Chem. Res. 33, 773, 2000.

[15] B. R. Hyun et al. Role of solvent dielectric properties on charge transfer from PbS nanocrystals to molecules. Nano Lett. 10, 318, 2010.

[16] Yu P and Cardona M Fundamentals of Semiconductors (Springer-Verlag, Berlin Heidelberg 1999), 2nd edition, Chapter 6.

[17] A. I. Ekimov et al. Absorption and intensity-dependent photoluminescence measurements on CdSe quantum dots: assignment of the first electronic transitions, J. Opt. Soc. Am. B 10, 100, 1993.

[18] S. E. Kohn, P. Y. Yu, Y. Petroff, Y. R. Shen, Y. Tsang and M. L. Cohen M L, Electronic Band Structure and Optical Properties of PbTe, PbSe, and PbS, Phys. Rev. B 8, 1477, 1973. See figure 12 and subsequent discussions as well as to a list of such higher energy excitonic transitions in lead salts mentioned in Table 1.

[19] J. W. Luo, A. Franceschetti and A. Zunger, Carrier multiplication in semiconductor nanocrystals: theoretical screening of candidate materials based on band-structure effects, Nano lett. 8, 3174, 2008.

[20] A. Nozik, Quantum dot solar cell, Physica E 14, 115, 2002.

[21] M. S. Hybertsen, Absorption and emission of light in nanoscale silicon structures, Phys. Rev. Lett. 72, 1514, 1994.; C. Delerue, G. Allan and M. Lannoo, Theoretical aspect of luminescence of porous Si, Phys. Rev. B 48, 11024, 1993.

[22] S. Datta and K. L. Narasimhan, Model for physical absorption in porous Si, Phys. Rev. B 60, 8246, 1999.

[23] Y. Wang, A. Suna, W. Mahler and R. Kasowski, PbS in polymers from molecules to solids. J. Chem. Phys. 87, 7315, 1987.

[24] S. Schmitt-Rink, D. A. B. Miller and D. S. Chemla,Theory of the linear and nonlinear optical properties of semiconductor microcrystallites, Phys Rev. B 35, 8113, 1987. Refer to equation 19.

[25] H. Kanazawa and S. Adachi, Spectroellipsometry and electroreflectance of PbS, J. Appl. Phys. 83, 5997, 1988.

[26] A. Franceschetti, Structural and electronic properties of PbSe nanocrystals from first principles, Phys. Rev. B 78, 075418, 2008.

[27] V. I. Klimov, Optical Nonlinearities and Ultrafast Carrier Dynamics in Semiconductor Nanocrystals, J. Phys. Chem. B 104, 6112, 2000.

[28] M. Stobbe, R. Redmer and W. Schattke, Impact ionization rate in GaAs, Phys. Rev. B 49, 4494, 1994.

[29] L. Tirino, M. Weber, K. F. Brennan, E. Bellotti and M. Goano M, Temperature dependence of the impact ionization coefficients in GaAs, cubic SiC, and zinc-blende GaN, J. Appl. Phys. 94, 423, 2003.

[30] J. Y. Tang and K. Hess, J. Appl. Phys. 54, 5139, 1983.

[31] V. I. Klimov, A. A. Mikhailovsky, D. W. McBranch, C. A. Leatherdale and M. G. Bawendi, Quantisation of multiple auger states in semiconductor nanoparticles. Science 287, 1011, 2000.

[32] V. I. Klimov, A. A. Mikhailovsky, S. Xu, A. Malko, J. A. Hollingsworth, C. A. Leatherdale, H. J. Eisler and M. G. Bawendi, Optical gain and stimulated emission in nanocrystals quantum sots, Science 290, 314, 2000.

[33] A. Piryatinski and K. A. Velizhanin, An exciton scattering model for carrier multiplication in nanocrystals: Theory, J. Chem. Phys. 133, 084508, 2010.

[34] A. Franceschetti, J. M. An and J. Zunger J, Impact ionization can explain carrier multiplication in PbSe quantum dots, Nano Lett. 6, 2191, 2006.

[35] G. Nootz, L. A. Padilha, L. Levina, V. Sukhovatkin, S. Webster, L. Brzozowski, E. H.Sargent, D. J. Hagan and E. W. VanStryland, Size dependence of carrier dynamics and carrier multiplication in PbS quantum dots, Phy. Rev. B 83, 155302, 2011.

[36] N. Sano and M. Tomizawa and A. Yoshii, IEEE Transaction on electron devices 42, 2211, 1995.

[37] G. A. Thomas, A. Frova, J. C. Hensel, R. E. Miler and P. A. Lee, Collision broadening in the exciton gas outside the electron-hole droplets in Ge, Phys. Rev. B 13, 1692, 1976.

[38] S. DasSarma and D. W. Wang, Many-Body Renormalization of Semiconductor Quantum Wire Excitons: Absorption, Gain, Binding, and Unbinding, Phys. Rev. Lett. 84, 2010, 2000; Wang D W, and DasSarma S, Phys. Rev B. 64, 195313, 2001.

[39] Meyer J R and Bartoli F J Dynamic dielectric response to electron-hole and electron-electron interactions, Phys. Rev B 28, 915, 1983.

[40] A. L. Rogach, Covalent bound CdTe nanocrystals, Mat. Sci. and Eng B 69-70, 435, 2000.

[41] M. G. Lisachenko, E. A. Konstantinova, P. K. Kashkarov and V. Timoshenko Yu, Dielectric effect in Si quantum wires, Phys. Stat. Sol. (a) 182, 297, 2000.

[42] S. W. Buckner, R. L. Konold and P. A. Jelliss, Luminescence quenching in PbS nanoparticles, Chem. Phys. Lett. 394, 400, 2004.

[43] M. Califano M, J. Phys. Chem. C 112, 8570, 2008.

[44] E. Hendry, M. Koeberg, F. Wang, H. Zhang, C. De M. Donega, D. Vanmaekelbergh and M. Bonn, Direct observation of electro to hole energy transfer in CdSe quantum dots. Phys. Rev. Lett. 96, 057408, 2006.

[45] M. Califano, Giant suppression of auger electron cooling in charged nanocrystals, Appl. Phys. Lett. 91, 172114, 2007.

[46] N. S. Waldron, A. J. Pitera, M. L. Lee, E. A. Fitzgerald and J. A. Alamo, Positive temperature coefficient of impact ionization in strained Si, IEEE Transactions on Electron Devices 52, 1627, 2005.

[47] L. Turyanska et. al.Tailoring physical properties of PbS quantum dots by thermal annealing, Nanotechnology 20, 315604, 2009.

[48] J. A. McGuire, M. Sykora, I. Robel, L. A. Padilha, J. Joo, J. M. Pietryga and V. I. Klimov, Spectroscopic signature of photocharging due to hot-carrier transfer in solution of semiconductor nanocrystals under low-intensity ultra-violet excitation. ACS Nano, 4, 6087, 2010.

[49] A.V.R. Murthy, Padmashri Patil, Shouvik Datta, Shivprasad Patil, Photoinduced dark fraction due to blinking and photodarkening probability in aqueous CdTe quantum dots. J. Phys. Chem. C. 117, 13268-75, 2013.

[50] M. Califano, Photoinduced Surface Trapping and the Observed Carrier Multiplication Yields in Static CdSe Nanocrystal Samples, ACS Nano, 5, 3614, 2011.

[51] P. Tyagi and P. Kambhampati, False multiple exciton recombination and multiple exciton generation signals in semiconductor quantum dots arise from surface charge trapping, J. Chem. Phys. 134, 094706, 2011.

[52] B. Cho, W. K. Peters, R. J. Hill, T. L. Courtney and D. M. Jonas, Bulk like hot carrier dynamics in PbS quantum dots, Nano Lett. 10, 2498, 2010.

[53] C. F. Klingshirn C F Semiconductor Optics, (Springer, Berlin, 1997) Chapter 10.

[54] Z. Lin, A. Franceschetti and M. T. Lusk, Size dependent multiple exciton generation rate in CdSe quantum dots. ACS Nano, 5, 2503, 2011.

[55] O. E. Semonin, J. M. Luthe, S. Choi, H-Y. Chen, J. Gao, A. J. Nozik and M. C. Beard, Peak exciton quantum efficiency exceeding 100% via MEG in quantum dot solar cell. Science 334, 1530, 2011.

Chapter 7

Effect of Blinking on Hydrodynamic Size Measurement

I. Introduction

As we have seen before in the introduction chapter, the usefulness of semiconductor QDs for variety of device applications made this area attractive for research. Different useful properties of these QDs are the key to the success of various leading innovations in biomedical[1,2,3,4,5,6] research, electronics[7] and opto-electronics[8] industry. However, physical properties of the nanoparticles (NPs) are primarily dependent on the amount of spatial confinement of charge carriers i.e. size of NPs. This characteristic size is measured by few different approaches depending on the interest, like hydrodynamic size and crystallite size. Crystallite sizes are usually measured by X-ray diffraction and transmission electron microscopy. The crystallite size measures physical size of NP which consist mainly the part with crystallite planes and includes constituents of the NP only. Whereas, the hydrodynamic size also measures the small additional layer of capping ligands and the effective overall size due to interaction of NPs with surrounding solvent in addition to the solid core crystallite. The two approaches of measurements are qualitatively described in figure 7.1.

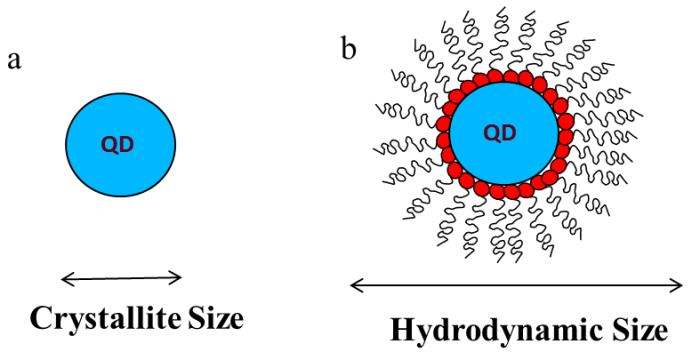

Figure 7.1. A schematic diagram showing a) crystallite size and b) hydrodynamic size of NPs.

Here we have used X-ray diffractometer as a tool to measure crystallite size of NPs whereas Dynamic Light Scatterer (DLS) and Fluorescence Correlation Spectroscopy (FCS) is used as a tool to measure hydrodynamic size of NPs. While studying the aging behavior of lead sulfide (PbS) Quantum Dots (QDs) (***Chapter 6***, section III f) we came across some anomalous results; the measured hydrodynamic size was found to be smaller compared to the calculated average crystallite size as shown in figure 7.2. As the hydrodynamic size consist additional contribution from ligand molecules as well as interaction with solvent it is in general greater than that of crystallite size. However, figure 7.2 shows an opposite behavior for QDs of smaller sizes.

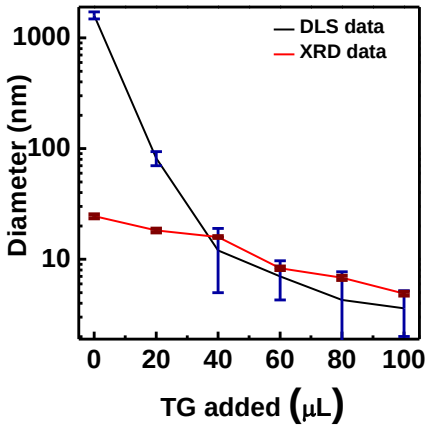

Figure 7.2. Average crystallite and hydrodynamic size of PbS QDs measured using XRD and DLS respectively.

Initially we thought that the smaller sized QDs are undergoing photo induced fragmentation while it is being excited by laser. However, such kind of fragmentation of NPs into smaller NPs happens only at or > 90 mW intensity[9,10] whereas in DLS the intensity of laser used for excitation is hardly 3- 4 mW. So to find out the reason behind this ambiguity we decided to do more experiments using FCS in collaboration with Dr. Shivprasad Patil's research group in IISER Pune. However, we could not use PbS QDs in these FCS measurements as the FCS only works with measurement of fluorescence fluctuation and fluorescence intensity from PbS QDs was considerably smaller than CdTe QDs. Therefore, in order to do this experiment we used fluorescent CdTe QDs, these QDs are synthesized as explained in ***Chapter 3***. Out of the various available sizes, we have used only four differently sized CdTe QDs for our study using FCS[11].

II. Materials and Methods

II. a. Fluorescence Correlation Spectroscopy (FCS)

FCS can be used to measure average number of luminescent particles in its detection volume[12,13,14,15]. We have used a home-built FCS setup available with Dr. Shivprasad Patil's group for all the measurements mentioned here. A diode laser of 532 nm, TEM00 mode (Dream lasers, China) was used as a photo excitation source. Excitation intensity is varied using a combination of neutral density filters from 3.3 kW/cm^2 to 145 kW/cm^2. FCS setup was calibrated by a standard fluorescent dye Rhodamine 6G (RH6G).

II. b. CdTe Quantum Dots

We have used four differently sized CdTe QDs in these measurements. The QDs are characterized using UV-VIS absorption and Photoluminescence spectroscopy and corresponding spectra is given in the figure 7.3. We have recorded a series of absorption spectra at various dilutions. A molar extinction coefficient of 5.6×10^4 mol^{-1}cm^{-1} is measured from the concentration versus peak absorbance data. The average diameters of these CdTe QDs are 3.4 nm, 4.1 nm, 4.2 nm and 4.5 nm respectively. The size of QDs noted here is calculated by applying effective mass approximation (EMA) formula[16,17,18] to its excitonic peak position in the

optical absorbance spectra. The absorption cross section is determined following ref[19]. The absorption cross section of QD with size 4.2nm is 2×10^{-16} cm^2. After complete characterization, QD samples are further diluted for FCS study.

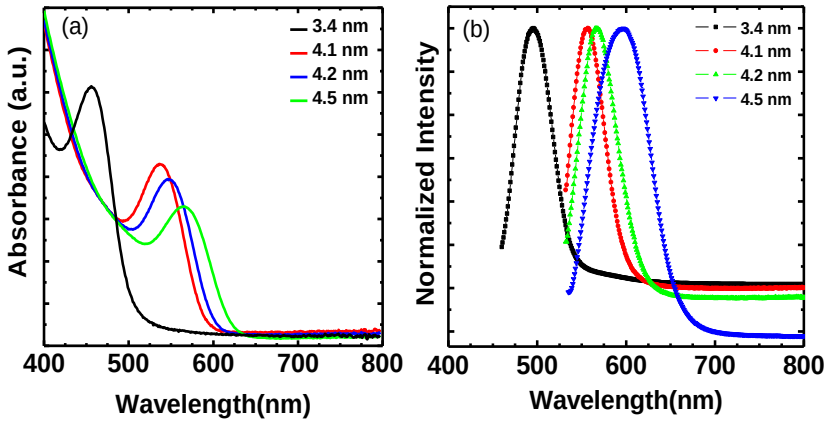

Figure 7.3. a) Absorbance spectra and b) photoluminescence spectra for the as prepared CdTe QDs.

III. Results and Discussions

a. FCS Study of QDs with Different Excitation Intensity

We have studied autocorrelation curves for 4.2 nm QDs at different excitation intensities starting from lowest available intensity ~3.3 kW/cm^2 to highest intensity ~145 kW/cm^2. For this study we have used extremely dilute aqueous solution of QDs. An analytical expression (7.1) describing nanoparticles diffusion is fitted for the autocorrelation data obtained from different excitation intensities[20,21,22,23].

$$G(\tau) = \frac{1}{N\left(1+\frac{\tau}{\tau_D}\right)\left(1+\left(r/1\right)^2\frac{\tau}{\tau_D}\right)^{1/2}} \qquad (7.1)$$

Here, the τ_D is the diffusion time or average residence time spent by luminescent QDs in the detection volume. This is the only characteristic time one get using this equation. Parameters r

and l are radial and axial dimensions of the detection volume respectively. The average number of fluorescent particles in the detection volume can be calculated by taking inverse of autocorrelation at zero time lag. The measured autocorrelations and fits to 3 D diffusion equation at different excitation intensities for 4.2 nm CdTe QDs is shown in the upper part of figure 7.4. The plot at the bottom is a representative fit at 145 kW/cm^2 showing the quality of the fit.

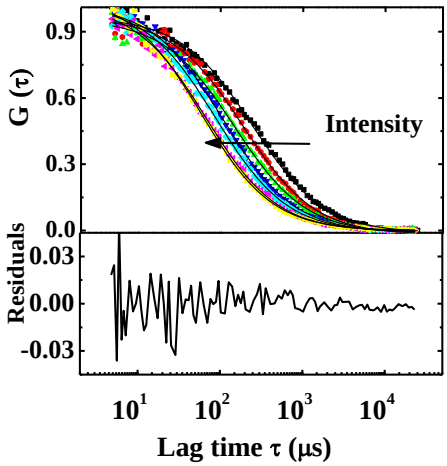

Figure 7.4. Autocorrelation curves obtained for 4.2nm QD excited at different intensities. The plot at the bottom shows residual after fitting the data equation 7.1. The dots represent obtained data and continuous black lines are the fits to the dots.

After fitting individual curves of figure 7.4 and using fit parameters, we have calculated values of τ_D and N i.e. diffusion time and average number of QDs in the detection volume respectively. The values of τ_D decreases with increase in photo-excitation intensity on other hand τ_D values for standard dye rhodamine (Rh6G) remains constant as shown in figure 7.5a. The direct indication of this result is that the size of the particles is decreasing as the excitation intensity increases i.e. particles are undergoing fragmentation. This cannot be true as the value for number of particles in the detection volume decreases as shown in figure 7.5b. Further observations are based on the estimated values of N for different excitation intensity as shown in figure 7.5b. These values of N initially decreases with intensity and after a while remain constant with increasing excitation intensity. At this we came across the phenomenon of 'blinking'[24,25,26]. in QDs and realized that this luminescence intermittency or 'blinking' events may explain the obtained results. Many researchers have tried to model blinking using Monte Carlo simulations,

stretched exponents and multiple exponents[27]. Though the exact reason for intermittency is not known[24,28,29,30,31], experiments revealed that the random "on" and "off" states in luminescence blinking occurs at all-time scale[24,25,26]. It is important to understand the photo-physics of luminescence blinking from single QD in aqueous solution as the "off" state affects ensemble quantum yield[32] and restricts advances in QD technology where a single QD is used[33]. It is also known that the blinking can be suppressed by the addition of thiols to a colloidal solution of QDs[34].

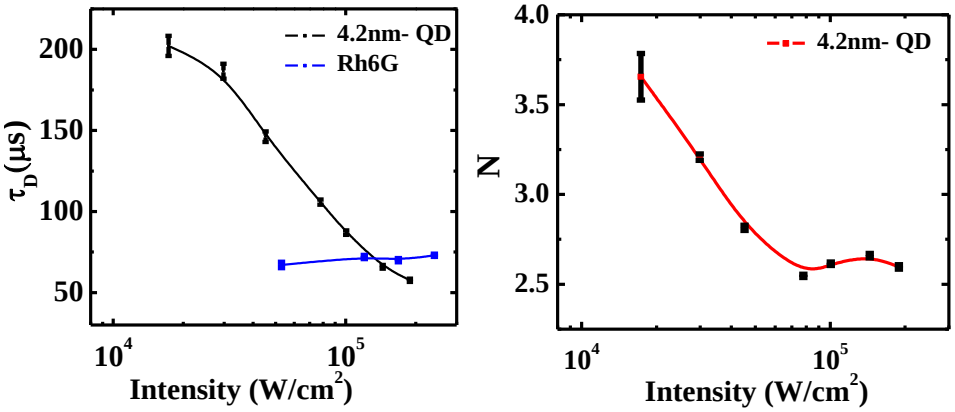

Figure 7.5. a) Dependence of diffusion time on the excitation intensity. b) Dependence of average number of QDs on intensity.

So we argue that blinking is the main reason for observing decrease in diffusion time and average number of QDs in detection volume as shown in schematic diagram 7.6a. As the QDs undergoes 'off' state while diffusing through the detection volume, the calculated number of QDs for particular intensity (figure 7.5b) is not the actual number of QDs present in detection volume. So we refer to this number as the apparent average number of QDs i.e. N_{app}. The actual number of QDs, both in dark and luminescent states which is higher than this, and we refer to it as N_{actual}. The measurements in figure 7.5b provide us an estimate of N_{app}. Further we attribute the reduction in τ_D to an apparently reduced detection volume due to a blinking QD. The cartoon in Figure 7.6b describes this concept. When a QD enters into the detection volume it starts to blink. While calculating autocorrelation a QD becoming dark is not different from a QD leaving the detection volume. Similarly, a QD becoming luminescent again is identical to a QD entering the detection volume. Therefore, the **effective detection volume** seen by a blinking QD is less

than the actual detection volume. This actual detection volume is usually measured using a standard fluorophore (Rh6G) with a known diffusion coefficient in a given medium. Due to the apparently reduced detection volume, the measured average residence time of blinking QD is less than its actual value. A close inspection of figure 7.5a reveals that at low excitation intensity, the τ_D does not change much with intensity and remains constant around 200 μs. From this value of τ_D and using the Stokes−Einstein relationship, we determined the hydrodynamic radius to be 3 nm. This matches well with the estimated radius of these QDs (2.2 nm) using the effective mass approximation to its excitonic absorption spectrum. The above result suggests that blinking does not affect measurement of the hydrodynamic radius of these CdTe QDs using FCS at lower intensities.

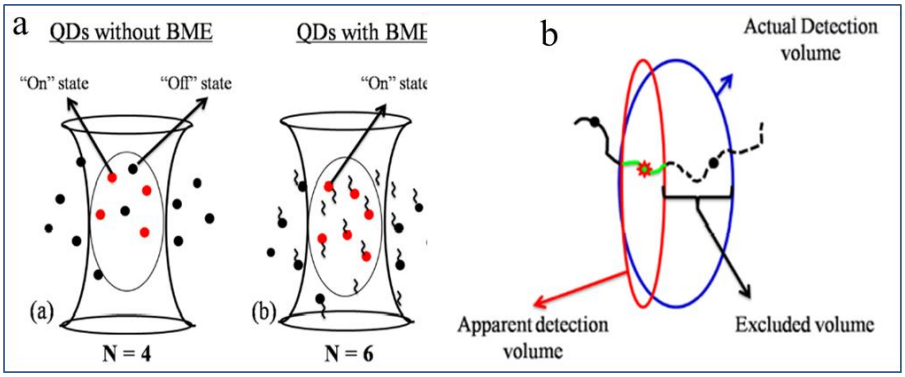

Figure 7.6. a) Schematic showing detection volume and effect of addition of BME on "ON" state of QDs b) Schematic describing 'apparently reduced detection volume' for blinking QDs.

b. Suppression of Blinking by Addition of BME

In this section we will prove the concept of apparent reduced detection volume and the apparent average number of QDs. We have performed same experiments after addition of BME to an aqueous solution of QDs, which make these QDs non-blinking. If the QDs are non-blinking then the "excluded volume" should not appear in the experiments and we should get back actual detection volume. Moreover, here the diffusion time τ_D should provide the correct hydrodynamic radius. Since thiol addition is known to suppress blinking[32,34,35] we have added 1mL of 100μM BME to an aqueous solution of QDs. As blinking affects ensemble quantum yield of a

nanoparticle, the per particle brightness (PPB) should increase after addition of BME. We have observed that the count rate as well as PPB increased from 19×10^3 s^{-1} to 36×10^4 s^{-1} and from 6×10^3 s^{-1} to 18×10^3 s^{-1}, respectively. Figure 7.7 shows autocorrelation curves before and after addition of BME at 145 kW/cm^2.

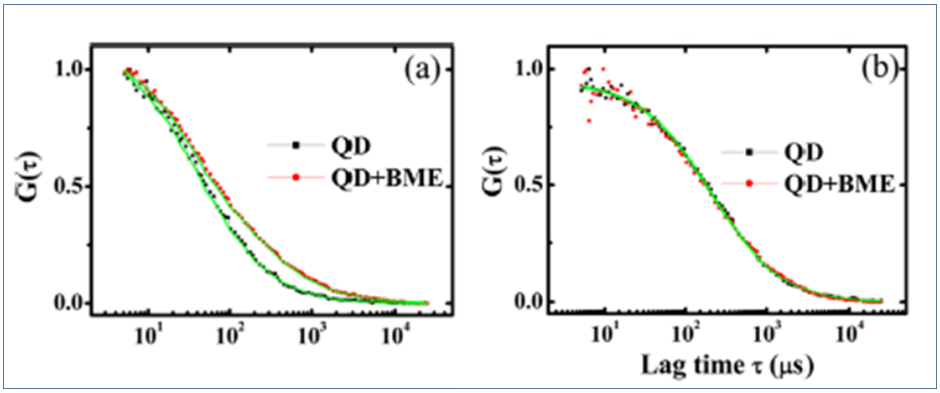

Figure 7.7. Autocorrelation curves for 4.2 nm QD before and after addition of BME a) excited at 145 kW/cm^2 intensity b) excited at 3.3 kW/cm^2 intensity.

We observed that after BME addition simple 3D diffusion fit equation (equation 7.1) does not fit to the autocorrelation instead, an analytical expression of equation 7.2 describing a diffusion kinetics plus single "on−off" rate fits to autocorrelation data. Equation 7.2is typically used in FCS analysis where a chemical reaction involving the luminescence "on−off" state along with diffusion contributes to the equilibrium intensity fluctuations[20,21,22,23].

$$G(\tau)=\left(1+\frac{F}{1-F}e^{-\tau/\tau_r}\right)\times\frac{1}{N\left(1+\frac{\tau}{\tau_D}\right)\left(1+(r/1)^2\frac{\tau}{\tau_D}\right)^{1/2}} \qquad (7.2)$$

Note that in this equation there are two characteristic time scale; one is τ_D which explains the diffusion time or average resident time spent by fluorescent molecule in detection volume. The second one is τ_r, which is a characteristic time needed to reach an equilibrium number of dark and bright populations and so the rate is reaction rate $k_r = 1/\tau_r$. The k_r is the sum of forward and backward rates in reaction causing luminescence[22]. F is the equilibrium dark fraction in dark−bright conversion[22]. After BME addition the luminescence fluctuations are caused due to

(a) fluorophores moving in and out of the detection volume because of diffusion, and (b) switching between "on" and "off" luminescence states of fluorophores with a single rate to attain equilibrium. Table 7.1 shows various parameters obtained by fitting 3D diffusion equations 7.1 and equation7.2 to measured autocorrelations in Figure 7.7a. As mentioned above, 3 D diffusion equation fits to autocorrelations without BME addition, whereas equation 7.2 fits to autocorrelations with BME addition. Both of these measurements are performed at 145 kW/cm^2 excitation intensity.

TABLE 7.1: Fit parameters are described before and after BME addition to QDs solution. (a) Average number of particles (N) (b) Diffusion time (τ_D) (c) Electron exchange rate (k_r) (d) Equilibrium dark fraction (F)

Sample	**Fit parameters at 145 kW/cm^2**			
	N [(a)]	**τ_D (µs) [(b)]**	**k_r (µs) [(c)]**	**F [(d)]**
QDs without BME	2.96 ± 0.01	40.96 ± 0.67	-	-
QDs with BME above 70 µM	4.74 ± 0.02	160.96 ± 11	28.3 ± 1.67	0.426 ± 0.01

From fit parameters, it is clear that the diffusion time after the addition of BME is recovered and now determines the hydrodynamic radius reasonably well. This supports the concept of "apparently reduced detection volume" presented in the previous section IIIa. Additionally, the fitting of equation 7.2 means that luminescence after the addition of BME fluctuates with a single rate $k_r = 1/\tau_r$[2222]. τ_r = 28.3 ± 1.67 µs in the present experiment. The fit value of 0.426 ± 0.01 for F also suggests that nearly 40% of the QDs are dark in equilibrium dark−bright conversion, yet all of them contribute to N[20,21,22]. A nonzero value for τ_r indicates that the addition of BME does not suppress luminescence fluctuations at all-time scales. This does not contradict the previous evidence of blinking suppression using BME since those measurements employ millisecond binning times[34]. After BME addition the average number of QDs in the detection volume increases from 2.96 ± 0.01 to 4.74 ± 0.02 (Table 7.1). The effect of BME addition on average number of QDs in the detection volume is shown in figure 7.8b.

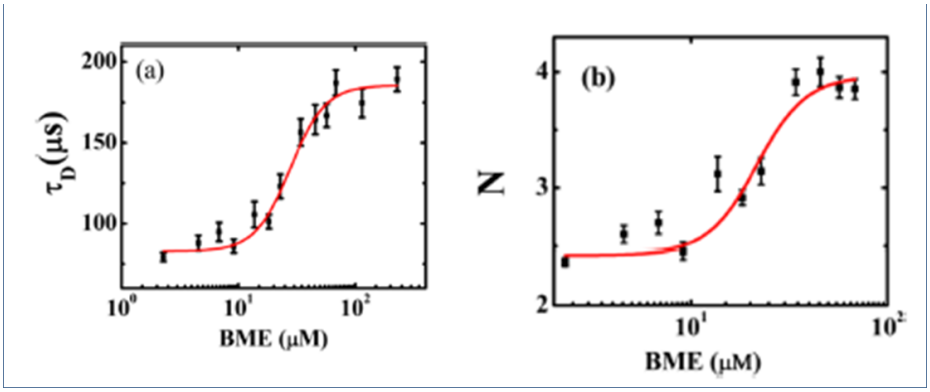

Figure 7.8. Effect of gradual addition of BME on a) diffusion time and b) average number of QDs in the detection volume.

In a collection of QDs there are blinking, non-blinking and non-radiant QDs[36]. As name suggests the non-radiant QDs remain dark at all times so in our measurement we are concerned only with blinking and non-blinking QDs. If we assume that addition of BME recovers all blinking QDs from their dark state then the actual number of QDs in the detection volume is $N_{actual} = 4.74 \pm 0.02$. As there is no evidence that long lived non-radiant QDs fully recover due to addition of BME, so the N_{actual} does not include them. Now the difference $\Delta N = N_{actual} - N_{app} = 4.74 - 2.96 = 1.78$ and the dark fraction due to blinking is $f = \Delta N/N_{actual} = 0.37$. It should be noted here that, the equilibrium dark fraction F, and the equilibrium dark fraction f due to blinking are not same. At very low intensity ~3.3 kW/cm^2, the addition of BME does not have any effect on FCS measurements. Figure 7.7 b shows autocorrelations for both before and after addition of BME at 3.3 kW/cm^2, importantly 3D diffusion equation 7.1 fits to both the autocorrelation curves before and after BME addition. Note that we are measuring τ_D and N by fitting the equations to data starting from 10 μs. This range is typically avoided in FCS measurements owing to photo-bleaching in the case of fluorophores[22] and rotational dynamics in the case of nanostructures[37]. We monitor fluorescence intensity trace at the time of experiment and the laser intensity used in our experiments is in the range of a few microwatts to a maximum of 500 μW only. So, if the QDs are suffering from photo-bleaching, average fluorescence intensity and per particle brightness should decrease within the autocorrelation record time (100 s). We did not observe these effects related to photo-bleaching. Secondly if the QDs are undergoing photo-bleaching then the equation describing only diffusion does not fit

autocorrelation properly. However, it fits very well in our experiments. We could not capture polarization of emission light which excludes effects of rotational dynamics on autocorrelation curves.

c. Required Number of BME Molecules per QD to Suppress Blinking

In this section we discuss how many number of BME molecules are needed per QD to suppress blinking? In order to do this measurement we have added controlled amount of BME to the 1ml of diluted QDs dispersion solution. The excitation intensity is kept constant 145 kW/cm^2 and autocorrelations are measured after each addition of BME. The data is plotted in figure 7.8 shows average number of QDs (N) versus BME addition. Initially the number of QDs is increases slowly, then changes rapidly and finally saturates. This growth is modeled with a sigmoid growth given by Hill equation, $\theta = \theta_{max}[x_n/(k_n + x_n)]$[38]. Here, θ is number of QDs recovered from photo-darkened state by BME addition and x is the concentration of BME molecules needed to recover half of the QDs from photo-darkened state. Calculations show that ~70 μM BME is required, i.e. 104 BME molecules are required to recover QDs from photo-darkened state by using value of detection volume 0.95 fL.

d. Dark Fraction (f) and photo-darkening Probability (P)

The Dark fraction (f) in dark-bright conversion is measured using FCS at different excitation intensity and is given as $f = \Delta N/N_{actual}$. The measured dark fraction (f) due to blinking at different excitation intensity is as shown in figure 7.9. A straight line fits to the data and yields slope 1.2×10^{-6} cm^2/W. The dependence of dark fraction on excitation intensity suggests that dark state in blinking is photo-induced and the linear dependence on intensity suggests that it is a one-photon process.

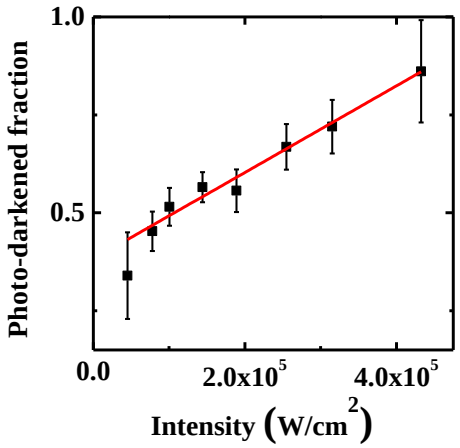

Figure 7.9. Photo-darkened fraction verses excitation intensity.

From figure 7.9 we can compute the probability of a QD becoming dark after absorption of a photon i.e. photo-darkening probability. Now the photo-induced dark fraction in our experiment must be equal to the product of photo-darkening probability P and number of photons absorbed n (i.e. f = P × n). Here, the number of photons absorbed 'n' can be computed if we know the absorption cross-section ρ, the excitation intensity I in kW/cm^2, the frequency of excitation υ and the illumination time t, then the n = Iρt/hυ[29].

$$\text{Therefore, } f = P \times I\rho t / h\nu$$

Now, theoretically the slope of the straight line (figure 7.9) is Pρt/hυ which is 1.2 × 10^{-6} cm^2/W. We have further computed value of P = 9 × 10^{-6}. For this calculations we have used hυ= photon energy for 532 nm wavelength of laser and ρ= 2×10^{-16} cm^2 (i.e. measured absorption cross-section). The illumination time t = 210 μs is considered as average diffusion time measured at intensity 3.3 kW/cm^2. The photo-darkening probability implies that typically a QD needs to absorb ~10^5 to 10^6 photos before it enters into a photo-darkened 'off' state. This result will now clarify why we could not see effect of BME addition on autocorrelation and why equation 1 fit to both the autocorrelations in figure 7.7b. For this particular event the excitation intensity was 3.3kW/cm^2, which corresponds to ~1 × 10^3 number of photons a QD can absorb while transiting through detection volume. The photo-darkened probability is 9 × 10^{-6}. It is very unlikely for a QD to enter into 'off' state so there is no apparently reduced detection volume effect. Whereas, for 145 kW/cm^2 intensity a 4.2 nm QD can absorb 1.6 × 10^5 average number of photons while its

transit inside the detection volume and hence there is more probability that QDs can enter into photo-induced dark state. This clearly explains that lower intensities do not affect FCS measurements but at higher photo excitation intensities above a certain threshold, nanoparticles may suffer from 'blinking'. Moreover, as we have discussed earlier, photo-darkening is typically a one photon process. The measurement of photoionization rate using electrostatic force microscopy also suggests photo-ionization is one photon process. The results for ionization probability measured using EFM[5] also matches with photo-darkening probability measured by us. Therefore, we suggest that in this case the photo-darkening is caused by photo-ionization.

e. Physical Meaning of the Rate (k_r)

An important parameter obtained after fitting autocorrelations to the equation 7.2 is k_r i.e. $k_r = 1/\tau_r$. In this section we will try to find out the physical meaning of this rate. Preliminary observations tempted us to label this rate as association-dissociation of BME molecules with QDs. If it is so then k_r should depend on the concentration of BME as well as the on the temperature. We found that once the BME concentration is reached to a point which is sufficient to recover all photo-darkened QDs then k_r does not depend on the further addition of BME. Further results also showed that the k_r does not depend on the temperature (inset of figure 7.10a). We measured k_r in the temperature range 25-65 ˚C. In this experiment temperature range is somewhat limited as we were using aqueous medium with water immersion objectives.

The second possibility for the interpretation is ionization-neutralization rate. As the charged QD losses its luminescence and recovers after neutralization, the addition of BME might be neutralizing the charged QDs by electron-donating ability. It is well known that the BME addition prevents long-lived charged state and enhances neutralization rates. If the k_r is ionization-neutralization rate then it should be depend on the QD core diameter (7.10a) and on the excitation rate (7.10b) i.e. the number of photons absorbed per second. We measured autocorrelation for four different sized QDs and calculated k_r values are plotted in figure 7.9b. It shows that the k_r is dependent on the size of QD and decreases as size of QD increases i.e. well width is affecting the attempt frequency (this is further explained in section f). Here, the QD with size 3.4 nm has peak absorbance wavelength 456nm so it is excited with a blue laser of 446 nm wavelength we have used standard coumarin dye for this calibration. With all these information,

FCS measurements support the charging model of luminescence blinking proposed by Nirmal et.al. and other scientists[24,25,26].

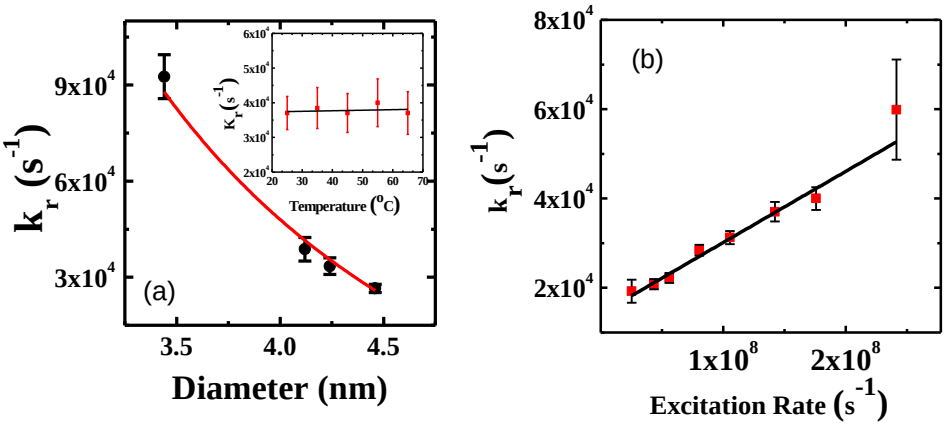

Figure 7.10. Dependence of k_r on a) temperature, b) size of QD and c) on excitation rate.

f. Mechanism of Photoionization

Many mechanism have been proposed to explain complex process of electron transfer from QD core[24,25,26,31]. Among all these proposed mechanisms, electron tunneling is thought be dominant process of ionization[24,25,26]. If it is so, then well width of the QD should affect attempt frequency. We assume that in case of QDs, the effective well width for electrons is the QD diameter itself i.e. core of QD. As shown in figure 7.9 the linear dependence of k_r on excitation intensity, inverse dependence on QD core diameter and its insensitivity towards temperature suggest that tunneling is the likely mechanism for electron exchange between core and surface trap state. Based on the obtained results we represented the photoionization process by a schematic as shown in figure 7.11.

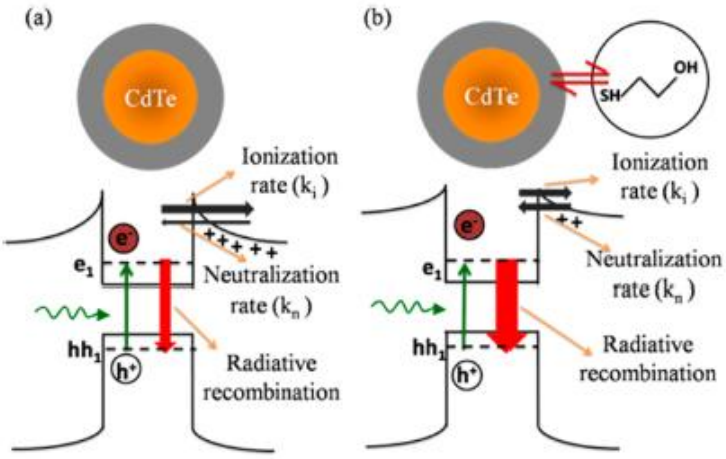

Figure 7.11. A schematic describing electron transfer process in photo-excited QD in aqueous solution. Radiative recombination rate is represented by a thick reed arrow. Occasionally an electron is transferred to the surface trap i.e. ionization rate and neutralization of the vacancy is shown by neutralization rate they are represented by black arrows. After addition of BME neutralization rate increases and the situation is shown in b.

Here, in the absence of BME, the photo-ionization rate is more compared to the neutralization rate and so the luminescence is weak (represented by downward red arrow). After addition of BME the electron transfer probability (the slope of fig 7.10b) is ~10^{-4} which is 10 times more than the photo-darkening probability (i.e. ~10^{-5}). So the addition of BME enhances the neutralization rate (shown by red arrow), and this in turn increases ionization rate as well. So the k_r is addition of ionization and neutralization rate ($k_r = k_i + k_n$)[22]. However fraction of QDs remaining dark at any given time is still around 40% even after BME addition. This indicates continues luminescence after BME addition on millisecond time-scale is not continues on microsecond time scale.

IV. Conclusions

In short, in this chapter we have seen that the intensity of photo-excitation does play a role in hydrodynamic size determination. Moreover the effect is not that crucial for below threshold intensities. So, one should not believe data of hydrodynamic size measurements before calculating the characteristic 'threshold intensity' for the particular QDs. We have understood that the blinking i.e. fluorescence intermittency affects the FCS measurements and this further

affect its use in different applications. We have used the FCS as a tool to measure the photo-induced dark fraction of QDs by recovering their luminescence with BME addition. The linear dependence of this fraction on intensity of band-edge photo-excitation suggests a one-photon photo-darkening process. This fraction is also used to calculate the probability of photo-darkening. The chemical kinetics rate in the reaction-diffusion model used in conventional FCS analysis is interpreted as the electron exchange rate that causes the "on−off" states of luminescence. The insensitivity of this rate toward temperature and its strong dependence on QD size supports the tunneling theory of electron exchange between core and surface trap states.

V. References

[1] A. Anas, H. Akita, H. Harashima, T. Itoh, M. Ishikawa, V. Biju, Photosensitized breakage and damage of dna by CdSe-ZnS quantum dots. J. Phys. Chem. B, 112, 10005−10011, 2008.

[2] I. L. Medintz, H. T. Uyeda, E. R. Goldman, H. Mattoussi, Quantum dot bioconjugates for imaging, labelling and sensing. Nat. Mater., 4, 435−446, 2005.

[3] M. Bruchez, Jr. M. Moronne, P. Gin, S. Weiss, A. P. Alivisatos, Semiconductor nanocrystals as fluorescent biological labels. Science, 281, 2013−2015, 1998.

[4] D. R. Larson, W. R. Zipfel, R. M. Williams, S. W. Clark, M. P. Bruchez, F. W. Wise, W. W. Webb, Water-soluble quantum dots for multiphoton fluorescence imaging in vivo. Science, 300, 1434− 1436, 2003.

[5] M. Michalet, F. F. Pinaud, L. A. Bentolila, J. M. Tsay, S. Doose, J. J. Li, G. Sundaresan, A. M. Wu, S. S. Gambhir, S. Weiss, Quantum dots for live cells, in vivo imaging, and diagnostics, Science, 307, 538−544, 2005.

[6] X. Y. Wu, H. J. Liu, J. Q. Liu, K. N. Haley, J. A. Treadway, J. P. Larson, N. F. Ge, F.Peale, M. P. Bruchez, Immuno fluorescent labeling of cancer marker and other cellular targets with semiconductor quantum dots. Nat. Biotechnol, 21, 41−46, 2003.

[7] V. I. Klimov, A. A. Mikhaelovsky, S. Xu, A. Mlko, J. A. Hollingsworth, Optical gain and stimulated emission in nanocrystal quantum dots. Science, 290, 314−317, 2000.

[8] V. L. Colvin, M. C. Schlamp, A. P. Alivisatos, Light-emitting diodes made from cadmium selenide nanocrystals and a semiconducting polymer. Nature, 370, 354−357, 1994.

[9] M. Fumitaka, K. Jun-ya, T. Yoshihiro and K. Tamotsu, Formation of gold nanoparticles by laser ablation in aqueous solution of surfactant, J. Phys. Chem. B, 105, 5114-5120, 2001.

[10] M. Fumitaka, K. Jun-ya, T. Yoshihiro and K. Tamotsu, Formation and size control of silver nanoparticles by laser ablation in aqueous solution, J. Phys. Chem. B, 104, 9111-9117, 2001.

[11] A.V.R. Murthy, Padmashri Patil, Shouvik Datta, Shivprasad Patil, Photoinduced dark fraction due to blinking and photo-darkening probability in aqueous CdTe quantum dots. J. Phys. Chem. C. 117, 13268-75, 2013.

[12] P. Zhang, L. Liang, C. Dong, H. Qian and J. Ren, Sizes of water-soluble luminescent quantum dots measured by fluorescence correlation spectroscopy, Analytica Chimica Acta, 546, 46-51, 2005.

[13] J. A. Rochira, M. V. Gudhti, T. J. Gould, R. R. Laughlin, J. L. Nadeu, S. T. Hess, Fluorescence intermittency limits brightness in CdSe/ZnS nanoparticles quantified by fluorescence correlation spectroscopy. J. Phys. Chem. C, 111, 1695-1708, 2007.

[14] D. Magde, E. Elson, W. W. Webb, Thermodynamic fluctuations in a reacting system-measurement by fluorescence correlation spectroscopy, Phys. Rev. Lett., 29, 705-708, 1972.

[15] D. Magde, E. Elson, W. W. Webb, fluorescence correlation spectroscopy. I. conceptual basis and theory, biopolymers, 13, 1-27, 1974.

[16] L. Brus, Electronic wave functions in semiconductor clusters: experiment and theory, J. Phys. Chem. 90, 2555–2560, 1986.

[17] Al. L. Efros and M. Rosen, The electronic structure of semiconductor nanocrystals, Annu. Rev. Mater. Sci., 30, 475–521, 2000.

[18] Y. William, Q. Lianhua, G. Wenzhuo, and P. Xiaogang, Experimental determination of the extinction coefficient of CdTe, CdSe, and CdS nanocrystals, Chem. Mater., 15, 2854-2860, 2003.

[19] C. A. Leatherdale, W. –K. Woo, F. V. Mikulec, M. G. Bawendi, On the absorption cross-section of CdSe nanocrystal quantum dots. J. Phys. Chem. B, 106, 7619−7622, 2002.

[20] D. Magde, E. Elson, W. W. Webb, Thermodynamic fluctuations in a reacting system-measurement by fluorescence correlation spectroscopy, Phys. Rev. Lett., 29, 705−708, 1972.

[21] D. Magde, E. Elson, W. W. Webb, Fluorescence correlation spectroscopy. I. conceptual basis and theory. biopolymers, 13, 1−27, 1974.

[22] O. Krichevsky, G. Bonnet, fluorescence correlation spectroscopy: the technique and its applications, Rep. Prog. Phys. 65, 251−297, 2002.

[23] Sengupta, P.; Balaji, J.; Maiti, S. Measuring Diffusion in Cell Membranes by Fluorescence Correlation Spectroscopy. Methods, 27, 374−387, 2002.

[24] M. Nirmal, B. O. Dabbousi, M. G. Bawendi, J. J. Macklin, J. K. Trautman, T. D. Harris, L. E. Brus, Fluorescence intermittency in single cadmium selenide nano crystals. Nature, 383, 802−804, 1996.

[25] M. Kuno, D. P. Fromm, H. F. Hamann, A. Gallagher, D. J. Nesbitt, "On"/"Off" fluorescence intermittency of single semiconductor quantum dots, J. Chem. Phys., 115, 1028−1040, 2001.

[26] K. T. Shimizu, R. G. Neuhauser, C. A. Leatherdale, S. A. Empedocles, W. K. Woo, M. G. Bawendi, Blinking statistics in single semiconductor nanocrystal quantum dots, Phys. Rev. B, 63 (205316), 1-5, 2001.

[27] S. Ito, N. Toitani, L. Pan, N. Tamai, and H. Miyasaka, Fluorescence correlation spectroscopic study on water-soluble cadmium telluride nanocrystals: fast blinking dynamics in the μs-ms region J. Phys. Condens. Matter., 19, 486208 10, 2007.

[28] D. E. Gomez, M. Califano, P. Mulvaney, Optical properties of single semiconductor nanocrystals. Phys. Chem. Chem. Phys., 8, 4989−5011, 2006.

[29] T. D. Krauss, S. O'Brien, L. E. Brus, Charge and photoionization properties of single semiconductor nanocrystals, J. Phys. Chem. B., 105, 1725−1733, 2001.

[30] S. Li, M. Steigerwald, L. E. Brus, Surface states in the photoionization of high-quality CdSe core/shell nanocrystals, ACS Nano, 3, 1267−1273, 2009.

[31] J. Zhao, G. Nair, B. R. Fisher, M. G. Bawendi, Challenge to the charging model of semiconductor-nanocrystal fluorescence intermittency from off-state quantum yields and multiexciton blinking. Phys. Rev. Lett., 104 (157403), 1−4, 2010.

[32] S. Jeong, M Achermann, J. Nanda, S. Ivanov, V. I. Klimov, J. A. Hollingsworth, Effect of the thiol-thiolate equilibrium on the photophysical properties of aqueous cdse/zns nanocrystal quantum dots, J. Am. Chem. Soc., 127, 10126−10127, 2005.

[33] M. Dahan, S. Lévi, C. Luccardini, P. Rostaing, B. Riveau, A. Triller, Diffusion dynamics of glycine receptors revealed by single−quantum dot tracking, Science, 302, 442−445, 2003.

[34] S. Hohang, T. Ha, T. Near-complete suppression of quantum dot blinking in ambient condition, J. Am. Chem. Soc., 126, 1324− 1325, 2004.

[35] L. N. Jay, L. Carlini, D. Suffern, O. Ivanova, S. E. Bradforth, Effects of β-Mercaptoethanol on quantum dot emission evaluated from photoluminescence Decays. J. Phys. Chem. C, 116 (4), 2728−2739, 2012.

[36] J. Yao, D. R. Larson, H. D. Vishwasrao, W. R. Zipfel, W. W. Webb, W. W. Blinking and nonradiant dark fraction of water-soluble quantum dots in aqueous solution, Proc. Natl. Acad. Sci. U.S.A., 102, 14284−14289, 2005.

[37] C. Dong, H. Qian, N. Fang, J. Ren, Study of fluorescence quenching and dialysis process of cdte quantum dots, using ensemble techniques and fluorescence correlation spectroscopy. J. Phys. Chem. B, 110, 11069−11075, 2006.

[38] A. V. Hills, The possible effects of the aggregation of the molecules of hemoglobin on its dissociation curves, J. Physiol., 40, iv−vii, 1910.

Chapter 8

Conclusions and Future Outlook

Synthesis of good quality nano-material is important for making efficient next generation solar cells. In order to fulfill the huge energy demand we need to come up with novel wet chemical synthesis techniques and efficient device structure. Keeping track of the economic viability and environmental concerns, we primarily have tried to do the synthesis in aqueous medium and at low temperature and further used these solution processed semiconductor quantum dots to make solar cells. Here in this thesis work, we have studied various synthesis routes to make good quality luminescent CdTe, CdTe/CdSe, PbS dots and also investigated their physical properties to optimize the solar cell performance. Introductory details of Semiconductor QDs and their relevance to energy problem are described in ***Chapter 1*** and required various characterizations techniques are introduced in ***Chapter 2***. Structural and optical properties of solution processed CdTe QDs are presented in ***Chapter 3***. The measured photoluminescence quantum yield for these CdTe QDs is ~85%, which is high compared to the other reported aqueous based synthesized CdTe QDs. Further we have also used these as active photo-absorber in Quantum Dot Sensitized Solar Cells (QDSSC). The measured efficiency was significantly affected by the destructive reaction between the QDs and the polysulfide electrolyte. However, we could find out the way to avoid such reactions by using type- II heterostructure i.e. core/shell QDs[1,2].

In ***Chapter 4,*** we have described the single step synthesis procedure for type-II heterostructure with CdTe as a core and CdSe as a shell material[1]. Cost is one of the most important primary concerns of Solar Cell fabrication. Therefore, any research in solar energy materials is important if it provides a better and economic way of making good quality materials for solar cells having reasonable efficiency. In ***Chapter 4***, we have reported a novel synthesis step which can reduce the overall time and cost of material synthesis as well as solar cell fabrication. The simple and low temperature (~80 ˚C) aqueous synthesis technique presented here provides a straightforward and procedurally economic, wet chemical synthesis route to make equally good core/shell CdTe/CdSe quantum dots without the complex purification steps and high temperature processing. The reported synthesis procedure is easy, quick and economic compared to the usual two step synthesis procedure. The similarities between the optical and structural properties of the synthesized QDs using these two different synthesis procedures prove the importance of such quick synthesis procedure with reduced processing steps. Thickness of CdSe shell layer was varied and the calculated efficiency for QDSSCs using thickest shell sample was ~2%. We have also observed that the efficiency is a function of shell thickness for core/shell QDs. The capping layer which is used to protect QDs from agglomeration and oxidation is insulating in nature and blocks carrier transport and further affects efficiency of cells. Sintering of photo-anode is also found to be important step in order to improve efficiency of these QDSSCs[2]. The above mentioned sintering process actually helps in easy charge transport by removing electronically insulating capping layer from QDs while maintaining the quantum confinement of charge carrier by some extent.

To avoid adverse effect from sintering we have used uncapped QDs as photo-absorber in QDSSCs[3]. ***Chapter 5*** presents solar cells results from such ligand free $AgInS_2$ QDs. The QDs used here were supplied by Dr. Angshuman Nag's group, IISER Pune. As the $AgInS_2$ is prone to have more defects, measured efficiency of our cells also compliments respective spectroscopy studies[3]. The highest efficiency using QDs with fewer defects is ~0.8% which is higher compared to any previously reported efficiency using this material.

In quantum confined structures, the carrier multiplication or multiple exciton generation (CM/MEG) by photons having much larger energy than the lowest energy gap is considered as one of the promising effect in order to achieve high efficiency solar cells at lower cost. In connection with this in ***Chapter 6,*** we report collisional broadening of high energy E_3 excitonic

resonance in lead sulfide (PbS) QDs at room temperature optical absorption spectra at excitation energies (≥ 5.9 eV) much higher than its bulk band gap (~0.4 eV)[4]. We have investigated absorption spectra of the PbS QDs over a wide range sizes, the energy broadening and their corresponding blue shift of excitonic resonance and its overall aging and temperature variation to support our arguments. In connection with the observed E_3 excitonic resonance in PbS, we explore how any empirical re-definition of the Bohr exciton radius may affect the mean free path of exciton-exciton collision and the basic understanding of MEG/CM. As the MEG/CM is a direct consequences of hot-exciton physics therefore, our results on the effects of excitonic collisions on absorbance spectra of PbS QDs, although observed at energies much above the visible range of solar spectrum, may help in understanding the physics of MEG/CM for photovoltaic applications.

In addition to this we have also studied the dependence of hydrodynamic size of QDs on the excitation intensity[5] using Fluorescence Correlation Spectroscopy (FCS) in collaboration with Dr. Shivprasad Patil, IISER Pune. Further study helps us to know more about the blinking in nanoparticles. Blinking is 'fluorescence intermittency'. Though the exact reason for the blinking is not yet know, we have calculated the photo-induced darkened fraction due to blinking. We have also observed that the blinking happens only above threshold excitation intensity and below which one can correctly use the FCS to determine size of QDs. We have added controlled amount of thiols to the aqueous solution of QDs which is known to suppress the blinking. We have calculated probability of QD entering into dark state upon photon absorption is ~10^{-6} which matches very well with similar estimates found using different techniques.

Future outlook:

Research is a never ending process, though we have done a lot of work and tried to find out the solutions for the few problems which we faced during the search, there is still some work which I will love to do in continuation (or one can do in continuation).

1. The huge need of affordable energy sources motivated us to do research in this area. Though we have done systematic study and tried to get best results out of the available infrastructure it is still possible to achieve higher efficiency using the same QDs. Further discoveries of efficient charge-transferring electrolyte, better pathways for electron transport, methods to fully cover

TiO_2 with optimum amount of nanoparticles, perfect non-reacting cathode may help in increasing the efficiency in future.

2. While studying the absorption spectra for core/shell QDs we observed that,

a) The absorption related to the CdTe QDs is also red shifting with core/shell growth as shown in figure 8.1. If one expects the growth of shell layer then this type of controversial red shift in core structure should not observed.

b) After prolonged growth of these core/shell structures this particular red shift diminishes in intensity and further vanishes as shown in inset of the figure 8.1 and inset of this figure 8.1. Further study is required understand this spectral variation.

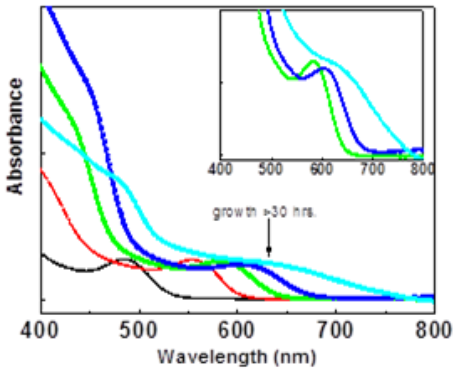

Figure 8.1. UV-visible absorption spectra for CdTe/CdSe core/shell QDs. Inset shows after prolonged growth of QDs the absorption peaks related to the CdTe diminishes.

c) The photoluminescence study of these core/shell structures shows very interesting behavior. The usual observation is as the shell thickness increases the PL intensity decreases (figure 4.11 of ***Chapter 4***) [1] but for very smaller shell growth the PL intensity increases and it is more compare to the seed QDs as shown in figure 8.2.

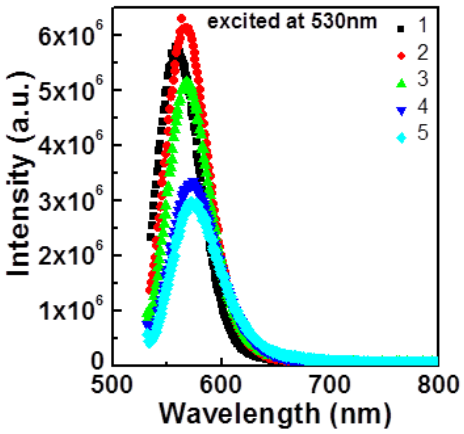

Figure 8.2. PL spectra for core/shell QDs. Here sample #1 is seed i.e. CdTe and all other samples are after subsequent growth of shell on it. All samples are excited at 530 nm.

Such kind of behavior opens up questions regarding the charge transport process happens in the type-II structure. Is the recombination of charge carriers happens after charge transfer (as shown in figure 8.3a)? Alternatively, is it due to strain induced changes or due to both such mechanisms (as shown in figure 8.3b)?. There is some ongoing experimental and theoretical studies in collaboration with Dr. Prasenjit Ghosh, IISER Pune.

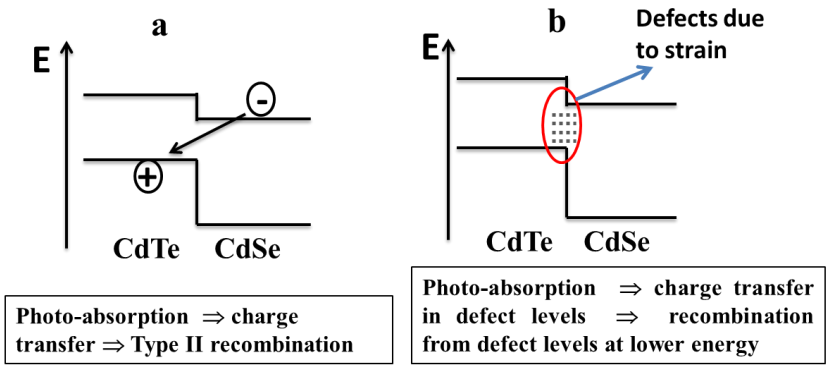

Figure 8.3. Energy level diagram for core/shell QDs showing a) usual type-II process b) charge transfer process via defect levels.

3. Detailed optical and electronic study of transient photo current etc may throw more light on possible ways to use CM/MEG to enhance the efficiency of nano-photovoltaic cells. This may also be useful to understand the excitonic physics of hot carriers.

4. Systematic FCS study with varying shell thickness can reveal further information on blinking in core/shell quantum dots. As explained in the ***Chapter 7***, the blinking affects diffusion and so the hydrodynamic size of QDs[5]. However, in case of core/shell QDs the energy level alignment is such that blinking may not be possible or can be reduced with increasing shell thickness. One can use FCS to quantify blinking in such core/shell structure.

References

[1] Padmashri Patil*, Clan Laltanzuala, Shouvik Datta, Sensitized solar cell from type-ii cdte/cdse core/shell nanocrystals synthesized without seed purification at low temperature, J. Alloys and Compound, 607, 230-237, 2014. (* corresponding author)

[2] Padmashri Patil, Thermal sintering improves the short circuit current of solar cells sensitized with CdTe/CdSe core/shell nanocrystals, Environmental Science and Engineering, pp 343-346, 2014.

[3] Kiran P. Kadlag, Padmashri Patil, M. J. Rao, Shouvik Datta and Angshuman Nag, Luminescence and solar cell from ligand-free colloidal $agins_2$ nanocrystals, Cryst. Eng. Comm, 16, 3605-3612, 2014.

[4] Padmashri Patil and Shouvik Datta, do we need to revisit the bohr exciton radius of hot excitons? arXiv: 1105.2205

[5] A.V.R. Murthy, Padmashri Patil, Shouvik Datta, Shivprasad Patil, Photoinduced dark fraction due to blinking and photodarkening probability in aqueous CdTe quantum dots. J. Phys. Chem. C. 117, 13268-75, 2013.